Part V

Annexes

A List of all results

A.1 Articles in journals with IF

F. Abdolahpur Monikh, L. Chupani, K. Smerkova, T. Bosker, P. Cizar, V. Krzyzanek, L. Richtera, R. Franek, E. Zuskova, **R. Skoupy**, G. K. Darbha, M. Vijver, E. Valsami-Jones, and W. Peijnenburg. Engineered nanoselenium supplemented fish diet: toxicity comparison with ionic selenium and stability against particle dissolution, aggregation and release. *Environmental Science: Nano*, 2020. doi:10.1039/D0EN00240B

R. Skoupy, T. Fort, and V. Krzyzanek. Nanoscale Estimation of Coating Thickness on Substrates via Standard less BSE Detector Calibration. *Nanomaterials*, 10(2):332, 2 2020. doi:10.3390 /nano10020332

R. Skoupy, J. Nebesarova, M. Slouf, and V. Krzyzanek. Quantitative STEM imaging of electron beam induced mass loss of epoxy resin sections. *Ultramicroscopy*, 202:44–50, 2019. doi:10.1016/j.ultramic.2019.03.018

V. Holan, E. Javorkova, K. Vrbova, Z. Vecera, P. Mikuska, P. Coufalik, P. Kulich, **R. Skoupy**, M. Machala, A. Zajicova, and P. Rossner. A murine model of the effects of inhaled CuO nanoparticles on cells of innate and adaptive immunity - a kinetic study of a continuous three-month exposure. *Nanotoxicology*, pages 1–12, 4 2019. doi:10.1080/17435390.2019.1602679

P. T. Knotigova, J. Masek, F. Hubatka, J. Kotoucek, P. Kulich, P. Simeckova, E. Bartheldyova, M. Machala, T. Svadlakova, J. Krejsek, N. Vaskovicova, **R. Skoupy**, V. Krzyzanek, S. Macaulay, M. Katzuba, L. Fekete, P. Ashcheulov, M. Raska, I. Kratochvilova, and J. Turanek. Application of Advanced Microscopic Methods to Study the Interaction of Carboxylated Fluorescent Nanodiamonds with Membrane Structures in THP-1 Cells: Activation of Inflammasome NLRP3 as the Result of Lysosome Destabilization. *Molecular Pharmaceutics*, 16(8):3441–3451, 8 2019. doi:10.1021/acs.molpharmaceut.9b00225

E. Drazanova, L. Kratka, N. Vaskovicova, **R. Skoupy**, K. Horska, Z. Babinska, H. Kotolova, L. Vrlikova, M. Buchtova, Z. Starcuk, and J. Ruda-Kucerova. Olanzapine exposure diminishes perfusion and decreases volume of sensorimotor cortex in rats. *Pharmacological Reports*, 71(5):839–847, 10 2019. doi:10.1016/j.pharep.2019.04.020

S. Marvanova, P. Kulich, **R. Skoupy**, F. Hubatka, M. Ciganek, J. Bendl, J. Hovorka, and M. Machala. Size-segregated urban aerosol characterization by electron microscopy and dynamic light scattering and influence of sample preparation. *Atmospheric Environment*, 178:181–190, 2018. doi:10.1016/j.atmosenv.2018.02.004

D. Fialova, **R. Skoupy**, E. Drozdova, A. Patak, J. Pinos, L. Sín, R. Benus, and B. Klima. The Application of Scanning Electron Microscopy with Energy-Dispersive X-Ray Spectroscopy (SEM-EDX) in Ancient Dental Calculus for the Reconstruction of Human Habits. *Microscopy and Microanalysis*, 23(6):1207–1213, 2017. doi:10.1017/s143192761701266198

A.2 Articles in journals without IF

J. Hrabina, M. Jelinek, **R. Skoupy**, M. Hola, B. Mikel, O. Cip, and J. Lazar. Reference optickýchkmitočtů na bázi mikrostrukturních fotonických vláken a jejich využití ve frekvenčně stabilizovaných laserových systémech. *Jemná mechanika a optika*, 6:161–163, 2020

E. Chocholova, D. Fialova, **R. Skoupy**, E. Drozdova, and L. Sin. Detection of surface contamination in ancient dental calculus by scanning electron microscopy. *Česká antropologie*, 68(1-2):12–17, 2018

N. Vaskovicova, **R. Skoupy**, and V. Krzyzanek. Aplikace nízkých teplot pro zvýšení katodoluminiscenčního signálu v rastrovacím elektronovém mikroskopu. *Jemná mechanika a optika*, 10:260–263, 2017

D. Fialova, E. Drozdova, **R. Skoupy**, P. Mikulik, and B. Klima. Scanning electron microscopy of dental calculus from the great moravian necropolis Znojmo-Hradiště. *Anthropologie (CzechRepublic)*, 55(3), 2017

A.3 Book section

D. Fialova, R. Benus, **R. Skoupy**, and E. Drozdova. Mikroskopická analýza zubního kamene z velkomoravského pohřebiště Devín – Za kostolom. In *Katarína Harmadyová. Devín Veroniky Plachej Zborník k životnému jubileu PhDr. V. Plachej*, pages 143–151. Múzeum mesta Bratislavy, Bratislava, 2017

A.4 Conference abstracts

R. Skoupy, V. Krzyzanek, L. Kocova, and J. Nebesarova. Electron beam induced mass loss dependence on aging of Epon resin sections. In A. Kittel and B. Pecz, editors, *12th Multinational Congress on Microscopy: Proceedings*, pages 112–113. Akademiai Kiado, Budapest, 2015

R. Skoupy, J. Nebesarova, and V. Krzyzanek. Electron Beam Induced Mass Loss Dependence on Stained Thin Epon Resin Sections. *Microscopy and Microanalysis*, 22(S3):926–927, 7 2016. doi:10.1017/S143192761600547X

D. Fialova, **R. Skoupy**, E. Drozdova, V. Krzyzanek, L. Sin, R. Benus, and B. Klima. The Application of Scanning Electron Microscopy with Energy Dispersive X-ray Spectroscopy (SEM-EDX) in Ancient Dental Calculus for the Reconstruction of Human Habits. *Microscopy and Microanalysis*, 22(S3):2056–2057, 7 2016. doi:10.1017/S1431927616011119

R. Skoupy, V. Krzyzanek, and J. Nebesarova. Plasma cleaning effect on the stability of the Epon resin sections. In *European Microscopy Congress 2016: Proceedings*, pages 597–598, Weinheim, Germany, 12 2016. Wiley-VCH Verlag GmbH & Co. KGaA. doi:10.1002/9783527808465.EMC2016.5995

M. Machala, P. Kulich, O. Serý, S. Marvanová, **R. Skoupy**, A. Rusnák, P. Mikuska, and Z. Vecera. The deposition of inhaled titanium nanoparticles in mice organs. In *Toxicology Letters:*

Abstracts of the 52nd Congress of the European Societies of Toxicology (EUROTOX) Fibes Congress Center Seville, volume 258, page S277, 2016. doi:10.1016/j.toxlet.2016.06.1969

R. Skoupy, J. Nebesarova, and V. Krzyzanek. Temperature dependent mass loss of Epon resin sections. In *Mikroskopie 2016: Proceedings*, page 56. Czechoslovak microscopy society, Praha, 2016

R. Skoupy, N. Vaskovicova, K. Hrubanova, P. Kulich, J. Turanek, and V. Krzyzanek. Cathodoluminescence imaging and mapping of biological samples in cryo-SEM. In *The 51st Annual Meeting of the Israel Society for Microscopy: Proceedings*, Rehovot, 2017.
URL:http://www.ismicroscopy.org.il/ism2017/files/2017/05/Poster-13.pdf

R. Skoupy, D. Fialova, M. Dornhoferova, V. Krzyzanek, and E. Drozdova. Soil contamination of human dental calculus determined by Energy-dispersive X-ray spectroscopy. In *13th Multinational Congress on Microscopy BOOK OF ABSTRACTS*, 2017

K. Hrubanova, V. Krzyzanek, O. Samek, **R. Skoupy**, M. Siler, J. Jezek, S. Obruca, and P. Zemanek. Morphological and Production Changes in Planktonic and Biofilm Cells Monitored Using SEM and Raman Spectroscopy. *Microscopy and Microanalysis*, 23(S1):1158–1159, 7 2017. doi:10.1017/S1431927617006456

N. Vaskovicova, **R. Skoupy**, A. Patak, K. Hrubanova, and V. Krzyzanek. Cathodoluminescence Study of Microdiamonds and Improvements of Signal Detection by Lowering Temperature of the Sample. *Microscopy and Microanalysis*, 23(S1):2284–2285, 7 2017. doi:10.1017/S1431927617012089

T. Stark, E. Drazanova, N. Vaskovicova, V. Pekarik, J. Ruda-Kucerova, **R. Skoupy**, P. Kulich, M. Buchtova, Z. Starcuk, F. Drago, A. Sulcova, and V. Micale. Sex differences in a neurodevelopmental animal model of schizophrenia: focus on white matter structures and myelin. *European Neuropsychopharmacology*, 27:S890–S891, 10 2017. doi:10.1016/S0924-977X(17)31590-0

S. Marvanova, P. Kulich, **R. Skoupy**, F. Hubatka, M. Ciganek, J. Bendl, J. Hovorka, and M. Machala. Size-segregated urban particulate matter characterization by electron microscopy and dynamic light scattering during the sample preparation. *Toxicology Letters*, 280(December2017):S180, 10 2017. doi:10.1016/j.toxlet.2017.07.506

R. Skoupy and V. Krzyzanek. Correlative imaging using CL and STEM detector in a SEM. In *Mikroskopie 2018: Proceedings*, Czechoslovak microscopy society, Praha, 2018

R. Skoupy and V. Krzyzanek. Thickness determination of a cathodolumenescence active nanoparticles by means of quantitative STEM imaging. In *Proceedings of the 16th International Seminar: Recent Trends in Charged Particle Optics and Surface Physics Instrumentation*, pages 74–76. Institute of Scientific Instruments The Czech Academy of Sciences, 2018

R. Skoupy and V. Krzyzanek. Correlative cryo-qSTEM-CL imaging in a SEM. In *International Microscopy Congress: Proceedings*, Sydney, 2018

R. Skoupy and V. Krzyzanek. Determination of thickness refinement using STEM detector segments. In *NANOCON 2018 - Conference Proceedings, 10th Anniversary International Conference on Nanomaterials - Research and Application*, Ostrava, 2019

R. Skoupy and V. Krzyzanek. Determining the accuracy of qSTEM for use in electron beam induced mass loss studies. In *Mikroskopie 2019: Proceedings*, pages 105–106. Czechoslovak microscopy society, Praha, 2019

R. Skoupy and V. Krzyzanek. Assessing the thickness error rate of quantitative STEM measurements. In *Proceedings from the 14th multinational congress on microscopy*, page 498, Belgrade, 2019

B Referred full texts

B.1 Quantitative STEM imaging of electron beam induced mass loss of epoxy resin sections

R. Skoupy, J. Nebesarova, M. Slouf, and V. Krzyzanek. Quantitative STEM imaging of electron beam induced mass loss of epoxy resin sections. *Ultramicroscopy*, 202:44–50, 2019. doi:10.1016/j.ultramic.2019.03.018

Ultramicroscopy 202 (2019) 44–50

Contents lists available at ScienceDirect

Ultramicroscopy

journal homepage: www.elsevier.com/locate/ultramic

Quantitative STEM imaging of electron beam induced mass loss of epoxy resin sections

Radim Skoupy[a], Jana Nebesarova[b,c], Miroslav Slouf[d], Vladislav Krzyzanek[a,*]

[a] Institute of Scientific Instruments of the Czech Academy of Sciences, Kralovopolska 147, 612 64 Brno, Czech Republic
[b] Institute of Parasitology, Biology Centre of the Czech Academy of Sciences, Branisovska 31, 370 05 Ceske Budejovice, Czech Republic
[c] Faculty of Science, Charles University in Prague, Vinicna 7, 128 44 Prague 2, Czech Republic
[d] Institute of Macromolecular Chemistry of the Czech Academy of Sciences, Heyrovsky Sq. 2, 162 06 Prague 6, Czech Republic

ARTICLE INFO

Keywords:
Scanning electron microscopy
Scanning transmission electron microscopy
Mass loss
Epoxy resin
EMbed 812 resin
Epon resin

ABSTRACT

In sample preparation of biological samples for electron microscopy, many types of embedding media are widely used. Unfortunately, none of them is perfectly resistant to beam induced damage. The article is focused on mass loss measuring of pure epoxy resin EMbed 812 that replaced Epon – the most widely used embedding resin for biological electron microscopy, in a form of ultrathin sections with thicknesses ranging from 30 to 100 nm. The STEM imaging was performed in a quantitative way which allowed us to estimate the mass loss directly up to the total dose of 3000 e^{-}/nm^{2}. For data acquisition we used SEM equipped with a commercial STEM detector working at a relatively low acceleration voltage of 30 kV. In this study we estimated the influence of various factors which can affect the endurance of the epoxy resin EMbed 812 ultrathin sections under an electron beam, such as the sample aging, differences between storing the samples in forms of ultrathin sections and whole blocks, ultrathin sections thicknesses, temperature of the sample, probe current, and one or two-sided carbon coating of ultrathin sections. The aim of this work is to investigate beam induced mass loss at electron energies of SEM and find out how to reduce the mass loss.

1. Introduction

Low voltage transmission electron microscope (TEM) and scanning transmission electron microscope (STEM) can be regarded as a method of choice for many structural studies of very thin biological samples, ultrathin sections, viruses etc. [1–3]. The main advantages of these techniques are that they allow images of low contrast samples being taken. Usually, in a conventional TEM (acceleration voltage typically 60–300 kV) the image contrast is enhanced by staining, using salts of heavy metals (e.g. uranyl acetate, lead citrate [4]). Staining procedures can be omitted in the case of using modern detectors (e.g. CMOS with direct electron detection [5,6]), which offer imaging with a reduced electron dose and improved detection efficiency, making them suitable for quantitative measuring. This is not necessary in low voltage STEM, where the image contrast even of light elements is significantly higher. This is caused by increasing the electron scattering at lower acceleration voltage [7,8].

Omitting the staining procedures allows imaging of the investigated structures closer to the native state. During the most frequent preparation workflow used for a biological sample at room temperature, a small piece of biological material is fixed, dehydrated and embedded in an appropriate material for thin sectioning, such as a suitable resin [9]. After polymerization, the ultrathin sections are cut and examined in a microscope. There is a wide spectrum of resins, such as epoxy, methacrylate, melamine etc., commercially available, designated for various purposes. The epoxy resin EMbed 812 is considered to be the best embedding medium for ultrastructural studies, suitable for a range of hardnesses from soft tissues to bones; it replaced the most widely used embedding resin for biological electron microscopy, “Epon 812” [9,10]. The production of original Epon (Shell) stopped in 1984 [11]. There are commercially available alternatives based on 1,2,3-propanetriol glycidyl ether having slightly different properties: Poly/Bed 812 (Polysciences), LX-112 (Ladd Research Industries), Eponate 12 (Ted Pella), SPI Pon 812 (SPI supplies), Agar 100 (Agar Scientific) and EMbed 812 (Electron Microscopy Sciences - EMS). The wide range of resins has specific parameters such as penetrability into specimens and various hardness and mechanical stability after polymerization [12]. An important parameter for imaging is sensitivity to degradation by electron beam. There have not been many studies describing the resin sections mass loss quantitatively; the most comprehensive work was performed

* Corresponding author.
E-mail address: krzyzanek@isibrno.cz (V. Krzyzanek).

https://doi.org/10.1016/j.ultramic.2019.03.018
Received 12 December 2018; Received in revised form 26 March 2019; Accepted 29 March 2019
Available online 30 March 2019
0304-3991/

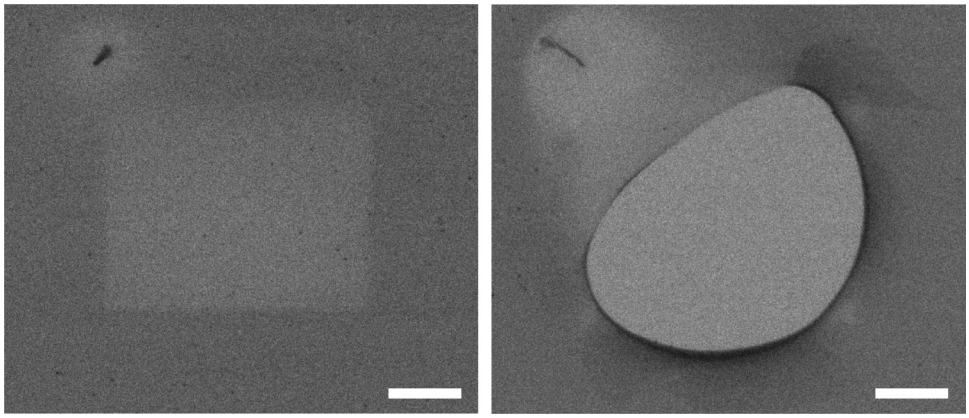

Fig. 1. Bright-field STEM images of multiple scanned area at half magnification (100,000 → 50,000 ×) of pure EMbed 812 epoxy resin ultrathin sections: brighter rectangle showing clearly the loss of material (left), and a hole burned in the section by electron beam (right). Bar 300 nm.

on a dedicated STEM for molecular mass measurements [13], done at voltages of 80 and 100 keV, or even at higher electron energies done by EFTEM [14]. However, there is a lack of such measurements at the energies applied in SEM.

Most researchers consider STEM to be a significant source of radiation damage and contamination of the irradiated area (investigated in [15]) on the ultrathin section surface during its examination. Strategies of damage control for TEM are described in [16], however, most of them are useful for STEM as well.

The mass loss indicates a degree of the radiation damage, therefore, we investigated the mass loss of embedding medium in specific conditions – divided into two general groups: parameters of the microscope (probe current) and properties of the sample (composition and thickness of ultrathin sections, surface modification of the sections by evaporated thin carbon layer, temperature of the sections). We had observed various types of sample reactions – different types of deformations, size increase/decrease; in the worst case the sample can be totally destroyed by electron beam (Fig. 1).

2. Material and methods

In this study, we focus on epoxy resin EMbed 812 of medium hardness that is considered to be the most stable resin used for embedding in electron microscopy. The resin EMbed 812 (EMS) was prepared precisely according to the instructions in the datasheet for making medium hard blocks (Table 1) [17]. The resin mixture was placed in flat embedding moulds and polymerized at 60 °C for 48 h. Ultrathin sections 30, 60 and 100 nm thick were cut with a UCT ultramicrotome (Leica microsystems) using a diamond knife (Diatome). The 30 nm sections were cut using the oscillating diamond knife (Diatome) according to the procedure described in [18]. Sections were floated on the water surface and picked up on 300 Mesh grids (EMS) without any supporting film (Table. 1).

The main technique used for mass loss quantitative measurement is based on the mass measurements by dedicated STEM [19–21], using SEM equipped with a commercial solid-state STEM detector [22–26].

2.1. Used equipment

The imaging was performed with SEM Magellan 400 L (FEI) at the acceleration voltage of 30 kV and the three lowest possible nominal probe currents: 1.6 pA, 6.3 pA and 13 pA. Images were captured in a field free mode (without magnetic field on the sample) by the bright-field (BF) segment with detection angle of 33.7 mrad of the commercial STEM3 detector (FEI). Electron dose for each scan corresponded to about 60 e^-/nm^2. Dark field (DF) segments of the used STEM detector were not applied because the signal in individual DF segments was too low for accurate measurement (based on the result of Monte Carlo simulations for given angular geometries of the DF segments). The SEM is equipped with a cryo-stage for the BALZERS/Leica microsystems cryo-holders and enables to cool the sample down to approximately −150 °C.

Table 1
Composition of the EMbed 812 epoxy resin.

EMbed812	DDSA	NMA	DMP30
20 mL	16 mL	8 mL	0.77 mL

2.2. Examined thin sections

Thickness of the used resin sections was ranging from 30 to 100 nm (the thickness was estimated during the sections being cut with the ultramicrotome by setting the thickness, and roughly confirmed by the colour of the slices). Thicker sections are not applicable for the used acceleration voltage (those were investigated in [27]). Resin slices were examined over the period of 6 weeks since the moment of cutting (Leica Ultracut UCT). During this time they were stored in an exicator filled with ROTH Silica Gel 1–3 mm at room temperature. Each grid was in the vacuum inside the microscope chamber only once (each measurement was performed using a new sample) so that the changes caused by repeated exposure to vacuum could be limited.

A thin layer of carbon for a stabilization study (as recommended in [28]) was prepared in the sputter coater ACE 600 (Leica microsystems) by carbon thread evaporation. Thickness measurement was done with an oscillating crystal that is a part of ACE 600.

2.3. Preparation of STEM beam damages

The resin slices mass loss measurement was accomplished by imaging the same area at magnification of 100,000 × (field of view 1.024 × 0.884 μm) in series of many consecutively scanned images (usually the first 50 images were captured). For each experiment, three different areas on each sample were imaged to reduce space dependency of the measurement.

2.4. Quantification of the radiation-induced 'bleaching'

The dose D applied on the sample was calculated by the following equation:

$$D_x = \frac{X \cdot t_p \cdot I_p}{a^2 \cdot e},$$

where X is the sequence number of the image in acquisition series, t_p is the dwell time, I_p is the probe current, a is the pixel size of the recorded image and e is the elementary charge of an electron.

For quantitative measurement it is necessary to calibrate data before processing them. We used two images captured during each imaging session, one of them for no electrons impacting on the STEM detector which is shaded by a grid holder (signal in the image is given by brightness settings) and the other for all emitted electrons impacting on the STEM detector (which has to be under saturation level). All measured images of real samples are somewhere between those extreme values. Using this calibration and normalization of all data to the real probe current in each imaging session eliminated the influence of fluctuations in measurement conditions among individual measurements. The correction of the probe current to the nominal value was measured for each session using the picoammeter KEITHLEY 6485 (Tektronix) connected to the Faraday cup mounted on the sample holder stage of the SEM. Actual values of the probe current were in the range from 84 to 87% of the nominal values. The mass loss was obtained from the normalized BF signals using the Monte Carlo simulation of electron scattering in soft materials MONCA [29], analogically to mass measurements by STEM [30]. In a nutshell, the method compares the captured electron intensity normalized between 0 (mean pixel value of the "dark" image) and 1 (mean pixel value of the "bright" image) with a simulated intensity calculated from the number of electrons captured by the detector at a known detection angle and the total number of simulated electrons. All processing was programmed in MATLAB (Mathworks).

3. Results

We observed irradiation consequences during the imaging by electron beam right at the beginning of image acquisition, typical examples of images of a multiple scanned area are shown in Fig. 1. A regular mass loss usually occurs in the full scanned frame (Fig. 1, left) where the irradiated area is clearly visible as the brighter rectangular part; the spot situated in upper left corner is caused by electron beam blanking in the time between capturing individual images. If the radiation dose is too high, there is a hole formed in the epoxy resin (Fig. 1, right). In general, we can split the observed phenomena into five subgroups: sample thickness effects, sample aging effects, sample temperature effects, probe current effects, and total radiation dose effects. All these effects are discussed separately in the following subsections.

3.1. Sample thickness dependencies

Individual epoxy resin sections cut by ultramicrotome at the same adjustments have various thicknesses which is evident in BF signal changes in the range of several hundredths in normalized units (the thickness variations are in the nm-range). A similar variability is observed even in the case of more measurements of one section. The results were shifted to the value calculated as the mean value of 10 measurements: 0.76 for 30 nm thickness, 0.63 for 60 nm and 0.45 for 100 nm section (all in normalized units of BF signal, see Section 2.4.). The comparison of different thickness dependencies on irradiated dose is in graphs Fig. 2a,b. The BF signals for all three thickness values have similar shapes with nearly linear parts (Fig. 2a). Relative mass-thickness (Fig. 2b), calculated from the normalized BF signals, clearly shows that the mass loss has exponential decrease and is much higher for 30 nm thin sections than for 60 and 100 nm thick ones. Our tentative explanation consists in that the conductivity of the sample is inversely proportional to its thickness. Therefore, the thinnest sample (here: 30 nm section) with the lowest conductivity does not eliminate surface charge so efficiently, which results in higher sample surface damage and higher mass loss, as discussed below in Section 4. The thicker samples (here: 60 and 100 nm sections) seem to be beyond the threshold where the thickness-related conductivity is sufficient to eliminate most of the surface charging.

3.2. Sample aging dependencies

The main aim of this study was to estimate the influence of aging (of the cut samples – sections) on sensitivity in relation to the irradiated dose. Over the period of 6 weeks we made a series of measurements to examine this influence that had been noticed earlier [31]. Fig. 2c shows how the beam damage of 30 nm thin slices cut from freshly prepared block of resin is changing in the course of this time. The measurement of the slices that were just cut (0 days old) is denoted "Day 0". We can see a decrease in sensitivity in first two weeks with maximum between day 8 and 15. After this time, sensitivity is increasing until the last measurement on the 41st day. After comparing the results at the same dose, visible aging consequences can be observed. In the case of imaging in the most stable time period, the BF signal is 0.82 after irradiated dose of 3000 e^-/nm^2, but on day 41 the thin section is burnt at a dose of 2880 e^-/nm^2. The corresponding mass loss is shown in Fig. 2d, where 68% of initial mass remains in the most stable age of the section.

Similar dependence is visible at the 60 nm section, too, though in a smaller scale (Fig. 2e) and with variability from 84% of the remaining mass in stable "window" to 43% on the last day measurement. There are changes visible on the 100 nm slice, with the highest stability on day 8. The variability of the relative mass is ranging from 75% (on day 8) to 65% (on day 29).

The results above were measured on ultrathin sections which were cut with ultramicrotome immediately after the polymerization of new resin EMbed 812 block was finished. The mass-loss measurement of 30 nm sections from an old block (prepared 6 months before the cutting) is shown on Fig. 2f. Results in the whole examined 27 days period are without any visible dependencies – all measured curves form a narrow band in the whole dose range. In comparison with equally thick sections prepared from the new block, these are much more stable.

Covering 60 nm sections with very thin carbon layer was examined concerning the suppression of beam damage effects as well as aging of the sections. For that, a carbon layer 3 nm thin was evaporated on the girds containing the sections either on one side (upper side) or both sides. As shown in Fig. 2g, the carbon layers stabilize the sections. Even one-sided covering causes a decrease in sensitivity to nearly linear dependency with a low slope. Covering both sides stabilizes the section against the mass loss even more. In both cases the carbon evaporation was done on day 1 (on fresh sections) and imaged on day 29. Another section of the same age was covered with carbon layer on both sides immediately before the examination; the effect of mass loss was also suppressed.

3.3. Probe current dependencies

Another important point during the imaging is to know the sensitivity to the probe current and the consequent possibility to image the samples at higher currents. As can be seen in Fig. 2h, a change from 1.6 pA to 13 pA has an impact on sensitivity of samples 30 nm thin, where measured curves have different shape, however, no dependency is observed on two-sided carbon coated 60 nm thick slice.

3.4. Applied dose dependencies

Measurements performed using higher electron doses showed not only the mass loss, but also contamination by hydrocarbons due to the imperfect vacuum in the SEM specimen chamber and not perfectly clean surface of the investigated sections. From a certain dose, mass loss and contamination are balanced in the BF signal so that the resultant slope is zero. Experiments with 60 nm thick slices were performed at a dose up to nearly 12,000 e^-/nm^2. There is visible a constant stretch between a dose of 4000 and 10,000 e^-/nm^2 in Fig. 3, and after this predominant contamination caused the decreases of the BF signal.

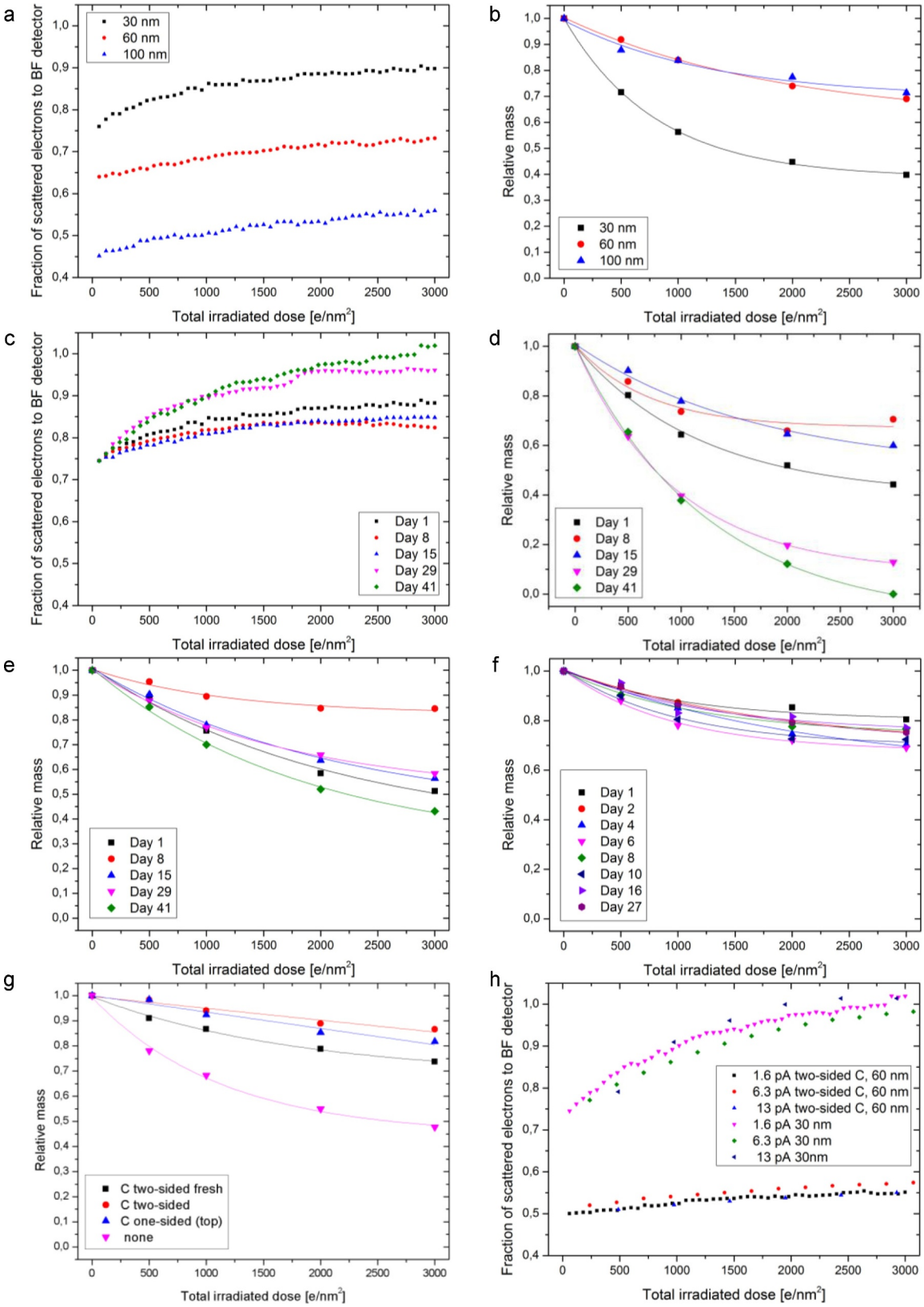

Fig. 2. Experimental measurements of the normalized bright-field signals and relative mass dependence on the total irradiation dose: (a,b) slices of various thickness recorded at "Day 1"; (c,d) aging of 30 nm thick slices; (e) aging of 60 nm thick slices; (f) aging of 30 nm thick slices cut from an old block;(g) covering of 60 nm thick slices at "Day 41" with thin carbon layer; and (h) used different probe currents for 30 and 60 nm thick sections.

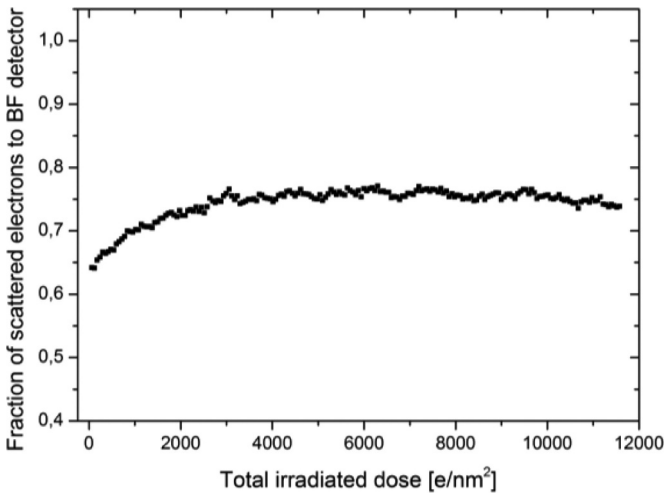

Fig. 3. Dependence of BF signal on the total dose of electrons, 60 nm resin slice, measured at high dose at day 6.

3.5. Temperature change dependencies

Our results show that the mass loss can be reduced by cooling the sample during the imaging in the SEM, however, the effect was significant only at relatively low doses as seen in Fig. 4. Note that mass loss at the dose of 3000 e^-/nm^2 is very similar for both temperatures (room temperature and −130 °C). We assume that this is due to the gradual heating of the sample placed on the grid and its poor thermal conductivity.

4. Discussion

We present quantitatively that properties of ultrathin sections are variable in time, and demonstrate it on pure epoxy resin EMbed 812 sections of medium hardness. It applies to all parameters, although some are more significant.

The thickness dependency estimation is demonstrated on 30 nm, 60 nm and 100 nm thick slices. The BF signals have very similar shapes if we manage to control the shift caused by different thicknesses. The 30 nm thin sections tend to burn the most, which is in agreement with our assumption that the conductivity of thin samples is not high enough to compensate for surface charging as discussed below. When relatively low acceleration voltage of 30 kV is used, more scattering occurs than in dedicated STEM [32], which causes damage at low dose.

In [19], results of mass loss examinations of pure EMbed 812 resin sections and *Escherichia coli* bacteria embedding are compared. It was found out that the pure plastic had the lowest beam sensitivity (a mass loss rate from a region with biological material on the same section is much higher), and the effect of section thickness is observed only at higher doses which corresponds to our results with all three measured thicknesses having similar shape (unlike us, Muller and Engel worked at a huge dose of 20,000 e^-/nm^2). It is difficult to compare the doses due to higher energy of electrons (acceleration voltage is 80 kV) and the resulting different cross section coefficient in this study. Another study [33] examined semi-thick EMbed 812 resin sections (300 nm) with the main conclusion that a shrinkage has exponential shape at low doses (for those under 10,000 e^-/nm^2) and nearly linear at higher doses.

The 30 nm thin slices which are about a month older already show burning through the section at relatively low doses of 3000 e^-/nm^2, unlike the newly prepared slices which are not perforated even at a higher dose. This is in contrast to 100 nm thick sections where no changes are visible (results in whole examinated period are invariable in time). For 60 nm thick sections the time dependencies are between these two cases. We recommend using slices about 10 days old, since these are the most stable. We assume that changes of features during the storage are connected with resin block maturation, because in the case of newly cut slices from an old block (stored 6 months before having been cut), considerably smaller changes are visible in the first 20 days. A decrease of stability can be observed for the first time around the 27th day. It shows that it is not the influence of surface changes, such as oxidation, but it could be in the volume of a thin section. Our result corresponds to the conclusions published in [34] according to which the influence of oxidation for EMbed 812 at room temperature is very low.

Mass loss seen during the sample examination can be reduced by covering the sections with a thin carbon layer which stabilizes epoxy slices excellently, even if the carbon layer is evaporated only to one side (top). It is not important in what phase a slice is covered by the carbon, whether immediately after having been cut or after some time before imaging.

The observed mass loss can occur due to both physical and chemical reasons. In this paragraph, we discuss the physical issues, while the next paragraph is focused on chemical issues connected with the electron beam induced polymer degradation. As described in [35], the used acceleration voltage is too high for the thermal effect (the effect

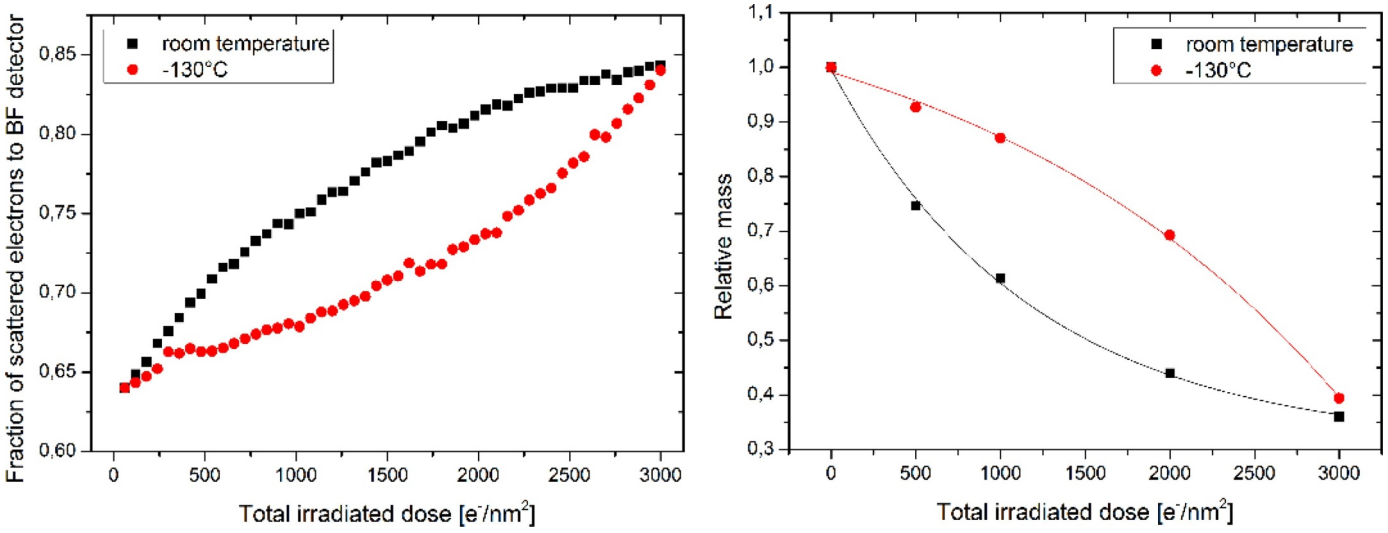

Fig. 4. Experimental measurements of the normalized bright-field signals (left) and relative mass (right) dependence on the total irradiation dose for the temperature of sample at room temperature and −130 °C.

becomes evident at acceleration voltage between 500 V and 2 kV, and the temperature rise in an organic specimen can reach several hundred degrees for non-scanning probe; the influence is reduced at video scanning rate – the temperature rise would always be less than 20 K [36]). On the other hand, for displacement damage and electron-beam sputtering, caused by high-angle elastic scattering, acceleration voltage used in our experiments is at lower limit. The mean displacement energy of carbon in molecular form is approximately 5 eV, and this amount of energy can be transferred in a head-on (180-degree angle) collision by incident electrons of energy of 30 keV or more [37]. Scattering cross sections appropriate to knock-on damage drop to zero between 20 and 100 keV for most organic compounds except the hydrogen, where a threshold energy is below 2 keV. Unfortunately the displacement cross sections for knock-on damage are a factor from 10^2 to 10^5 times lower than the damage cross sections for radiolysis [38], which we consider the main cause of the electron beam-induced damage. In conclusion, we can say that a simple reduction of the energy of primary electrons to eliminate the damage is not enough.

Radiolysis comes from inelastic scattering of incident electron beam and creation of secondary electrons (elastic scattering cross section for light elements decreases relative to the inelastic cross section so inelastic scattering dominates [39]). The damage should be proportional to the energy deposited per unit volume of the irradiated sample (average energy deposited per incident electron is given by the accelerating voltage, the sample thickness and the mean free path for inelastic scattering [38]). This brings higher radiolytic damage for low-energy electron beam because of higher ability of a sample to absorb the electrons. In the case of high-energy electron beam, most of the electrons go through a sample without absorption. General predictor for radiolysis is poor electrical conductivity with surface charging [32], which is inversely dependent on sample thickness [40].

In our measurements, this was proven as higher sensitivity of 30 nm thin sections in comparison with thicker ones. Our discovery is the possibility of using various probe currents. Even on non-covered slices the change of probe current has only a small impact (several hundredths in normalized signal, no trend during increasing the probe current is distinguishable). In the case of covered slices we did not observe any dependency. Efficiency of often used carbon layer covering may be in formation of a diffusion barrier reducing the escape rate for light gaseous elements, and removing charge from the specimen.

From the point of view of chemistry, the investigated resin (EMbed 812) can be classified as highly cross-linked thermosetting synthetic polymer. According to the information available from the manufacturer, the resin is a multi-component system, in which the main component (EMbed 812, commercial, exact composition unrevealed) contains epoxy groups, while the other important components are dicarboxylic acid anhydrides: DDSA (dodecenyl succinic anhydride) and NMA (methyl-5-norbornene-2,3-dicarboxylic anhydride); the remaining minor components of the mixture are amine accelerators (DBMA = N,N-Dimethylbenzylamine and DPM-30 = 2,4,6-Tris(dimethylaminomethyl)phenol). In general, the epoxy resins are prepared by curing, which consists in mixing the liquid epoxy precursors (here: EMbed 812) with suitable reactive agents such as polyamines, polythiols and anhydrides of polycarboxylic acids. In EMbed 812 the reactive curing agents are dicarboxylic acids (DDSA and NMA), which means they are bound to the EMbed 812 molecules with ester bonds [41]. On one hand, the ester-cross-linked epoxy resins have good mechanical performance and cuttability. On the other hand, the ester bonds may be susceptible to electron beam induced scissions [42]. At the beginning of curing process (open time step) the liquid precursor forms a gel (initial cure step), which gradually solidifies (final cure step). The cross-linking/curing rate increases with temperature and time, but even after rather long time the cured resin may contain both *gel* (cross-linked molecules, insoluble fraction) and *sol* (non-cross-linked, soluble fraction). Due to the random nature of the process, the shorter, low-molecular weight molecules with lower number of functional groups, have higher probability of remaining in the sol [43]. Consequently, the volatile molecules from the sol can be released from the resin upon irradiation with the electron beam; the effect is time-dependent (as shown in Section 3.2). The fact that the time dependence is non-linear and more pronounced in thinner sections (the strongest mass loss in 30 nm sections, weaker effect in 60 and 100 nm sections) suggests that also surface oxidative degradation might play an important role. It has been shown that the oxidative degradation is highly heterogeneous process, during which the deepest changes occur on the surface [44]. Last but not least, the electron beam irradiation causes chain scissions of the gel, which results in formation of another portion of volatile molecules escaping from the polymer and decreasing sample thickness. It is also worth noting that in a real, non-ideal network, not all molecules are bound on both ends; such molecules are easier to release due to electron beam induced chain scissions. The probability of chain scissions and, consequently, the overall sample degradation and mass-loss depend slightly on the probe current and significantly on the applied dose (as evidenced in Sections 3.3 and 3.4).

5. Conclusion

As presented in this paper, pure epoxy resin EMbed 812 sections have high variability in their features due to various factors. The main finding is the uneven sensitivity to electron beam in time after thin section preparation. We observed inclination of 30 nm thin sections to burning at relative low dose and specific age. Sections 60 and 100 nm thick are more stable but with significant mass loss. It follows from our measurements that samples embedded in resin EMbed812 are most stable for imaging around day 10, sliced with ultramicrotome from newly prepared block. Another way to lower the beam damage is to let the whole block mature and cut it after a selected time. We demonstrated the ability to stabilize the sample during irradiation, even with one sided carbon layer. In the case of two sided carbon covering the mass loss does not depend on the probe current used. Next topic for research arises from our examination - to determine the influence of carbon layer on the stabilized sample image quality, the impact of resin hardness on mass loss during its irradiation in the microscope (measurements were carried out only at medium hardness), and to compare different resins used for embedding biological samples (methacrylate, polyester, etc.).

Acknowledgments

The research was supported by Czech Science Foundation (project GA17-15451S). The research infrastructures were funded by Ministry of Education, Youth and Sports of the Czech Republic and European Commission (LM2015062), the Czech Academy of Sciences (project RVO:68081731) and the Technology Agency of the Czech Republic (project TN01000008). R.S. is grateful to a ThermoFisher/CSMS scholarship for support.

References

[1] H. Schatten, Scanning Electron Microscopy for the Life Sciences, Cambridge University Press, New York, 2013.
[2] A.E. Yakushevska, M.N. Lebbink, W.J.C. Geerts, L. Spek, E.G. van Donselaar, K.A. Jansen, B.M. Humbel, J.A. Post, A.J. Verkleij, A.J. Koster, STEM tomography in cell biology, J. Struct. Biol. 159 (2007) 381–391.
[3] H. Blank, R. Schneider, D. Gerthsen, H. Gehrke, K. Jarolim, D. Marko, Application of low-energy scanning transmission electron microscopy for the study of Pt-nanoparticle uptake in human colon carcinoma cells, Nanotoxicology 8 (2014) 433–446.
[4] D.G. Robinson, U. Ehlers, R. Herken, B. Herrmann, F. Mayer, F.W. Schürmann, Methods of Preparation for Electron Microscopy, Springer, Berlin Heidelberg, 1987.
[5] G. McMullan, A.R. Faruqi, D. Clare, R. Henderson, Comparison of optimal performance at 300 keV of three direct electron detectors for use in low dose electron microscopy, Ultramicroscopy 147 (2014) 156–163.
[6] M. Kuijper, G. van Hoften, B. Janssen, R. Geurink, S. De Carlo, M. Vos, G. van Duinen, B. van Haeringen, M. Storms, FEI's direct electron detector developments: embarking on a revolution in cryo-TEM, J. Struct. Biol. 192 (2015) 179–187.

[7] R.F. Egerton, Choice of operating voltage for a transmission electron microscope, Ultramicroscopy 145 (2014) 85–93.
[8] H. Drees, E. Muller, M. Dries, D. Gerthsen, Electron-beam broadening in amorphous carbon films in low-energy scanning transmission electron microscopy, Ultramicroscopy 185 (2018) 65–71.
[9] M.A. Hayat, Principles and Techniques of Electron microscopy: Biological Applications, 2d ed., University Park Press, Baltimore, 1981.
[10] J.H. Luft, Improvements in Epoxy Resin Embedding Methods, J Biophys Biochem Cy 9 (1961) 409–414.
[11] E.A. Ellis, No More Epon 812: this Product Does Not Exist Today, Microsc. Today 22 (2014) 50–53.
[12] A.M. Glauert, P.R. Lewis, Biological Specimen Preparation For Transmission Electron Microscopy, Princeton University Press, 2014.
[13] R. Reichelt, E. Carlemalm, W. Villiger, A. Engel, Concentration determination of embedded biological matter by scanning-transmission electron-microscopy, Ultramicroscopy 16 (1985) 69–80.
[14] M.A. Aronova, A.A. Sousa, G. Zhang, R.D. Leapman, Limitations of beam damage in electron spectroscopic tomography of embedded cells, J. Microsc.-Oxf. 239 (2010) 223–232.
[15] A.J.V. Griffiths, T. Walther, Quantification of carbon contamination under electron beam irradiation in a scanning transmission electron microscope and its suppression by plasma cleaning, J. Phys. 241 (2010) 012017.
[16] R.F. Egerton, Control of radiation damage in the TEM, Ultramicroscopy 127 (2013) 100–108.
[17] A.M. Glauert, Epoxy resins: an update on their selection and use, Microsc. Anal. 25 (1991) 15–20.
[18] J. Nebesarova, P. Hozak, L. Frank, P. Stepan, M. Vancova, The cutting of ultrathin sections with the thickness less than 20 nm from biological specimens embedded in resin blocks, Microsc. Res. Techniq 79 (2016) 512–517.
[19] S.A. Muller, A. Engel, Structure and mass analysis by scanning transmission electron microscopy, Micron 32 (2001) 21–31.
[20] A.A. Sousa, R.D. Leapman, Quantitative STEM mass measurement of biological macromolecules in a 300 kV TEM, J. Microsc.-Oxf. 228 (2007) 25–33.
[21] J.S. Wall, M.N. Simon, J.F. Hainfeld, History of the STEM at Brookhaven National Laboratory, Adv. Imaging Electron Phys. 159 (2009) 101–121.
[22] M. Pfaff, E. Muller, M.F.G. Klein, A. Colsmann, U. Lemmer, V. Krzyzanek, R. Reichelt, D. Gerthsen, Low-energy electron scattering in carbon-based materials analyzed by scanning transmission electron microscopy and its application to sample thickness determination, J. Microsc.-Oxf. 243 (2011) 31–39.
[23] T. Volkenandt, E. Muller, D. Gerthsen, Sample thickness determination by scanning transmission electron microscopy at low electron energies, Microsc. Microanal. 20 (2014) 111–123.
[24] T. Woehl, R. Keller, Dark-field image contrast in transmission scanning electron microscopy: effects of substrate thickness and detector collection angle, Ultramicroscopy 171 (2016) 166–176.
[25] T. Klein, E. Buhr, C.G. Frase, TSEM: a review of scanning electron microscopy in transmission mode and its applications, Adv. Imaging Electron Phys. 171 (2012) 297–356.
[26] V. Morandi, P.G. Merli, Contrast and resolution versus specimen thickness in low energy scanning transmission electron microscopy, J. Appl. Phys. 101 (2007) 114917114911-114918.
[27] C. Kizilyaprak, G. Longo, J. Daraspe, B.M. Humbel, Investigation of resins suitable for the preparation of biological sample for 3-D electron microscopy, J. Struct. Biol. 189 (2015) 135–146.
[28] V.E. Cosslett, Radiation-damage in high-resolution electron-microscopy of biological-materials - review, J. Microsc.-Oxf. 113 (1978) 113–129.
[29] V. Krzyzanek, R. Reichelt, MONCA: a new MATLAB package for Monte Carlo simulation of electron scattering in thin specimens in the energy range 10–200 keV, Microsc. Microanal. 9 (2003) 110–111.
[30] V. Krzyzanek, S.A. Muller, A. Engel, R. Reichelt, MASDET-A fast and user-friendly multiplatform software for mass determination by dark-field electron microscopy, J. Struct. Biol. 165 (2009) 78–87.
[31] V. Novotna, K. Hrubanova, J. Nebesarova, V. Krzyzanek, Investigation of electron beam induced mass loss of embedding media in the low voltage STEM, Microsc. Microanal. 20 (2014) 1270–1271.
[32] R.F. Egerton, A modest proposal for the propagation of information concerning radiation damage in the tem, and as fodder for pasturized professors, Microsc. Today 21 (2013) 70–72.
[33] M.B. Braunfeld, A.J. Koster, J.W. Sedat, D.A. Agard, Cryo automated electron tomography: towards high-resolution reconstructions of plastic-embedded structures, J. Microsc.-Oxf. 174 (1994) 75–84.
[34] M.C. Celina, A.R. Dayile, A. Quintana, A perspective on the inherent oxidation sensitivity of epoxy materials, Polymer 54 (2013) 3290–3296.
[35] R.F. Egerton, P. Li, M. Malac, Radiation damage in the TEM and SEM, Micron 35 (2004) 399–409.
[36] P. Li, R.F. Egerton, Radiation damage in coronene, rubrene and p-terphenyl, measured for incident electrons of kinetic energy between 100 and 200 keV, Ultramicroscopy 101 (2004) 161–172.
[37] M.R. Libera, R.F. Egerton, Advances in the transmission electron microscopy of polymers, Polym. Rev. 50 (2010) 321–339.
[38] R.F. Egerton, Mechanisms of radiation damage in beam-sensitive specimens, for TEM accelerating voltages between 10 and 300 kV, Microsc. Res. Techniq. 75 (2012) 1550–1556.
[39] P. Echlin, K. Zierold, Low-temperature biological microscopy and analysis, Springer, New York, 1992.
[40] G.B. Feng, M. Cao, L.P. Yan, H.B. Zhang, Combined effects of sample parameters on polymer charging due to electron irradiation: a contour simulation, Micron 52-53 (2013) 62–66.
[41] J.R. Young, P.A. Lovell, Network Polymers, Introduction to Polymer Physics, CRC Press, Boca Raton, 2011, p. 688.
[42] S. Kumar, W.W. Adams, Electron-beam damage in high-temperature polymers, Polymer 31 (1990) 15–19.
[43] J.R. Young, P.A. Lovell, Gelation Theory, Introduction to Polymer Physics, CRC Press, Boca Raton, 2011, p. 688.
[44] J. Pilar, D. Michalkova, M. Slouf, T. Vackova, Long-term accelerated weathering of HAS stabilized PE and PP plaques: compliance of ESRI, IR, and microhardness data characterizing heterogeneity of photooxidation, Polym. Degrad. Stabil. 120 (2015) 114–121.

B.2 4D-qSTEM-SRIP: calibration-less local thickness estimation of amorphous samples

R. Skoupy, M. Slouf and V. Krzyzanek. 4D-qSTEM-SRIP: calibration-less local thickness estimation of amorphous samples. (*submitted*)

Journal Name

ARTICLE TYPE

4D-qSTEM-SRIP: calibration-less local thickness estimation of amorphous samples

Radim Skoupy [a], Miroslav Slouf [b] and Vladislav Krzyzanek *[a]

The classical quantitative imaging in scanning transmission electron microscope (qSTEM) is a powerful method for estimation of local sample properties like thickness or mass distribution. It is based on calibration data characterising the detector response to impacting electrons, capturing of data and its comparison with theoretical electron scattering. We present calibration-less qSTEM imaging technique where images taken by pixelated STEM detector are used. The position of the most probable scattering angle instead of individual pixel intensity is used as a bridge between experiment and simulation. It reduces the necessary beam current stability to single pixel dwell time and causes redundancy of accurate detector calibration prior each imaging session. All requirements for 4D-qSTEM-SRIP method (Summarised Radial Intensity Profile) are 4D data from pixelated STEM detector, knowledge of in-chamber geometry, and sample composition. The new calibration-less method was applied on two samples. For model monodisperse latex microspheres, the accuracy of the thickness estimation was better than 5 %. For the ultrathin section of PS / PMMA polymer blend (where PS = polystyrene and PMMA = poly(methyl methacrylate), we were able not only to differentiate the two chemically similar polymers without staining, but also to determine different mass-loss of the two polymers due to interaction with electron beam.

1 Introduction

Quantitative scanning transmission electron microscopy (qSTEM) is a powerful method for local thickness determination or particle mass measurement in a wide range of thicknesses or masses [1–6]. The principle of the method is based on the comparison of captured images with simulated signals of a sample with known characteristics like thickness, density and composition. For precise comparison of those signal intensities, the classical qSTEM requires STEM detector calibration images used as limits which can be found in both captured and simulated data. Local properties of a sample are assigned by fitting the same signal intensity in simulated data. In this work, we demonstrate how the qSTEM method can be performed without detector calibration. Moreover, we show the first results obtained with our new, calibration-less qSTEM approach and discuss its advantages and disadvantages.

1.1 Detector calibration methods

There are two types of detector calibration techniques. The first one is normalisation of captured images using the signal of a material / thickness standard, like bulk Pd [7], Au [8], Si and Au [9], or detector response to blanked beam and crystalline Si [10] or thin films with defined thickness [11]. This type is often used for calibration of back-scattered electron (BSE) detectors because of the geometry of the detector inside vacuum chamber of SEM. The second one is direct irradiation of a detector by primary electron beam (an example for annular STEM detector is shown in Fig.1). This type is mainly used in case of STEM detector, where the calibration limits are no impacting electrons on the detector as a bottom limit (primary beam blanked / 0 electrons for simulation) and all impacting electrons as an upper limit (number of simulated electrons). This type of calibration is used in most of qSTEM studies [11–13] or it can be extended for BSE electrons by reflection of primary electrons on electron mirror [14]. Although this approach is used in some applications, it has several disadvantages:

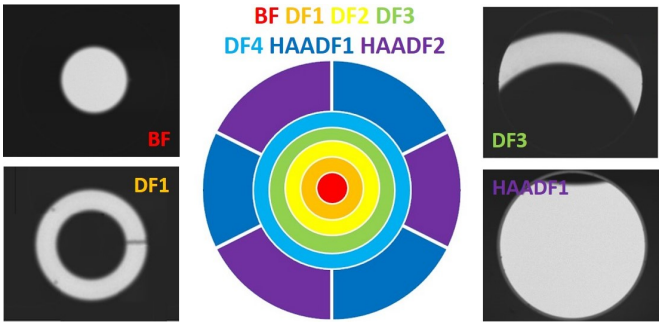

Fig. 1 Calibration images of full primary electron beam on different segments of annular STEM detector. The mean values of pixel intensity in individual bright areas are used as the upper calibration limits of each segment. Outer segments (DF3, HAADF) are unfortunately out of the field of view and moving the detector is necessary. The bottom calibration limit is obtained from images recorded at the same area and SEM condition when the beam is blanked.

- **Results change with time dependent beam current or detector contrast / brightness settings** – just a slight drift of a base signal line changes significantly the results because of its subtraction during the normalization of captured data accordingly to equation $I_{norm} = (I_{captured} - I_{base})/I_{range}$.

[a] The Czech Academy of Sciences, Institute of Scientific Instruments, Kralovopolska 147, Brno, Czech Republic.
[b] The Czech Academy of Sciences, Institute of Macromolecular Chemistry, Heyrovsky Sq. 2, Prague, Czech Republic.

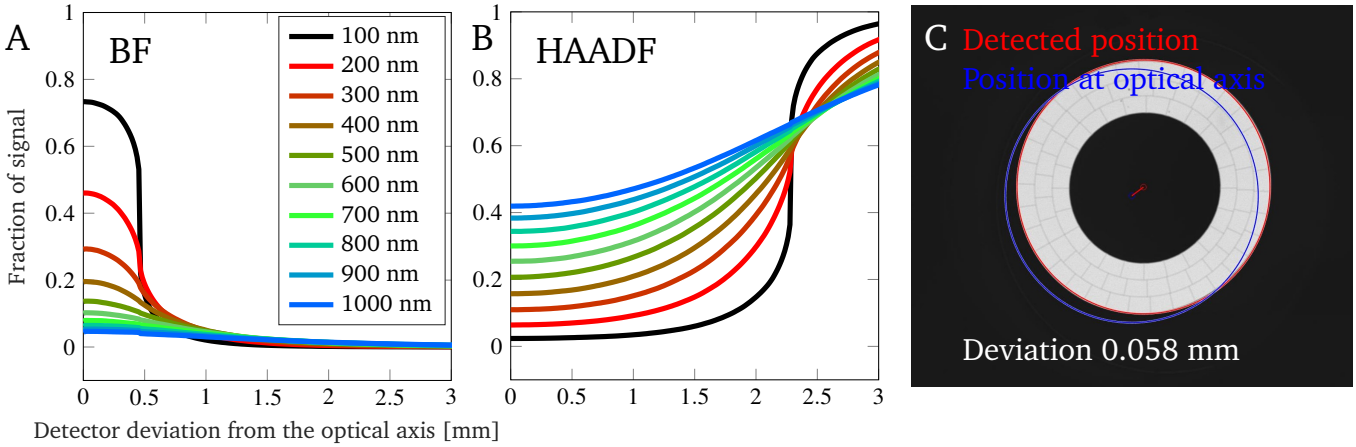

Fig. 2 Change of captured BF (A) and HAADF (B) signal accordingly to the detector deviation from the optical axis. (C) Analysis of real detector position – it is strongly dependent on its manual setting. Calculated for STEM III detector (Thermo Fisher Scientific), WD 4.5 mm, pole-piece – detector distance of 18 mm.

- **Partial segment calibration** – the calibration images give information about mean intensity in the image, unfortunately except the bright-field (BF) and inner dark-field (DF) segment, it is not possible to take an image of whole segment and only an image of part of segment is taken. The response of other parts of a segment can be different.

- **Coaxiality of detector and the optical axis** – detector deviation from the optical axis may induce systematic error because part of scattered electrons is captured by neighboring segment, which is not taken into account in simulation. The influence of this systematic error can be estimated from analysis of Monte Carlo (MC) simulation. We used simulation package MONCA (running under MATLAB) [15] because it has fully accessible partial results in form of MATLAB variable for following data processing. The results of simulation (settings: latex sample, density 1.05 g/cm^3, beam energy 30 keV, electron probe semiangle 0.76 mrad, electron probe diameter 1 nm, 200,000 electrons) is data structure with information about properties of each scattering event (position in x, y, z, scattering angle Θ and azimuth angle X, energy decay ΔE). For each simulated electron the distance from optical axis (in detector plane) was calculated and number of electrons captured by STEM detector segments of interest (BF and HAADF) was computed accordingly to the distance misalignment range from 0 to 3 mm (Fig. 2 A-B). The error caused by slight misalignment is negligible up to $\sim$0.2 mm. Higher detector deviation brings significant change in captured electron intensity. In our case we found the deviation of 0.058 mm (Fig. 2 C) which has no impact to the estimated thickness.

It would be advantageous to circumvent the need for such calibration or data normalisation and compare some different feature of sample signal than its size. The need for calibration can be elegantly circumvented by using a 2D STEM detector, where the position of the most probable scattering angle instead of individual pixel intensity can be used as a bridge between experiment and simulation.

1.2 Calibration-less approach

Classical detector calibration has to be done before each imaging session and so it brings up a disadvantage that imaging session has to be planed as "quantitative". It is not possible to take some images taken earlier and performe quantitative analysis based on those not calibrated images. We present a method for quantitative STEM imaging, where no detector calibration is required thanks to the use of pixelated STEM detector and quantitative analysis approach can by applied post-acquisition.

1.3 Application area of pixelated STEM detector

The pixelated STEM detectors (also called 2D STEM detectors) are widely used in material science for investigation of crystalline samples providing diffraction patterns in a wide variety of methods described in review [16]. Great amount of work done on different alloys, semiconductors [17], crystals [18], nanocrystals [19] or 2D materials [20] can be found .

In case of thin less ordered samples, the applications may be found as well: the size and distribution mapping of nanoscale crystalline regions in a polymer blend [21], characterization of the short- and medium-range order in aperiodically packed amorphous and partially crystalline organic molecules [22], strain mapping inside thin amorphous / partially crystalline samples [23,24] or *in-situ* measurements of interatomic nearest neighbor distances, average bond angles and coordination numbers in amorphous samples [25].

But there is no method for examination of thick amorphous samples, that are not creating ring-like features in their diffraction pattern. At those samples, the main advantage of 2D STEM detectors – capturing of full diffraction pattern, is seemingly redundant due to no direction preference of scattered electrons or absence of ring-like features. Diffraction / scattering patterns are in case of thick amorphous samples rationally symmetrical with the highest pixel value on optical axis, plus the change caused by

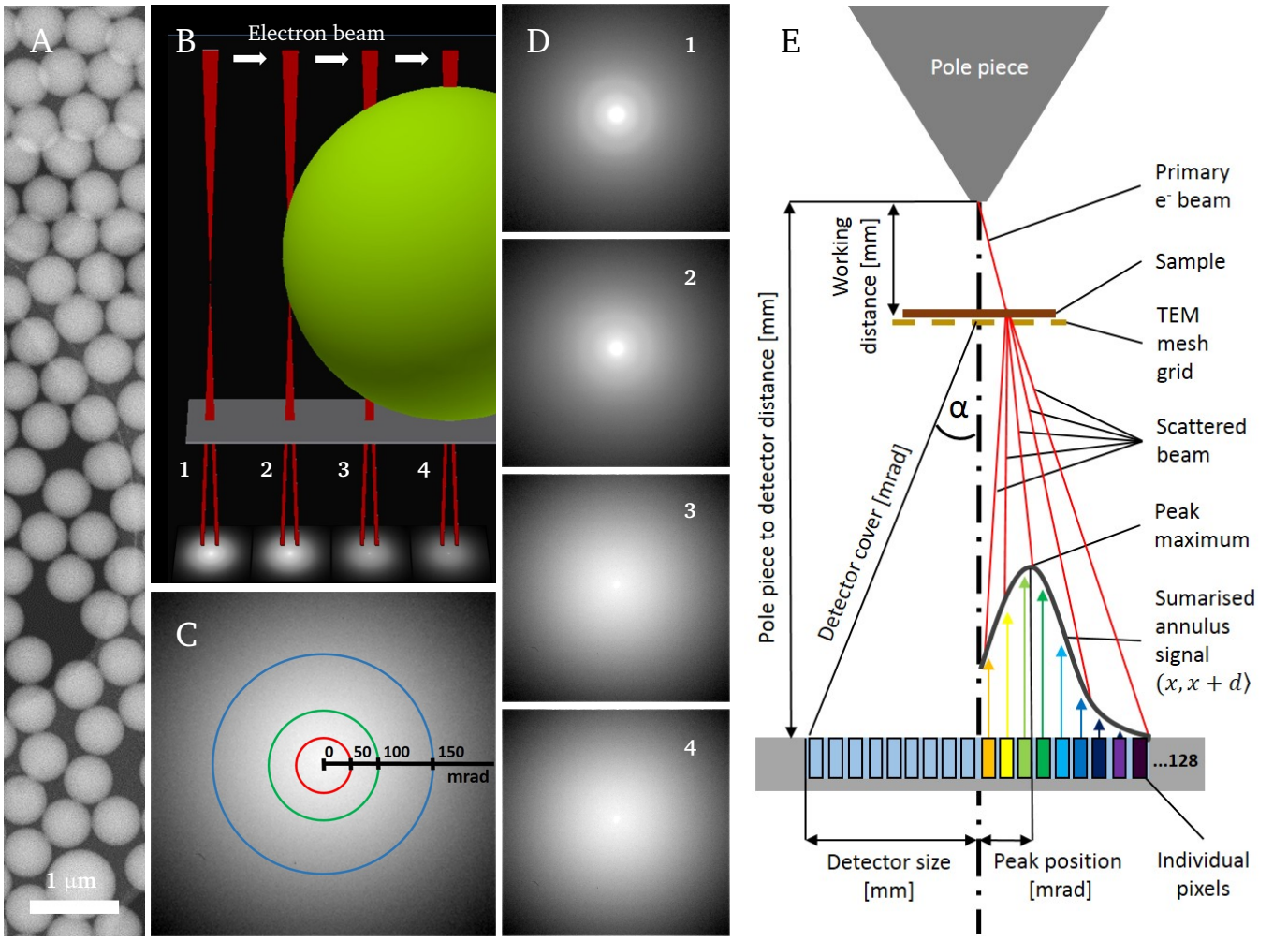

Fig. 3 (A) Latex nanospheres placed on thin-carbon / lacey carbon covered TEM grid. (B) Schematic drawing of 4D-qSTEM-SRIP method. Electron beam scans over a sample and scattering pattern is captured for each beam position. This approach creates 4D dataset which is further processed and the information about local thickness is extracted. (C) Highlighting of pixels with the same chosen scattering angles. (D) Scattering patterns of test sample in beam positions from 1 to 4. Spreading of electrons to higher scattering angles is obvious in shifting position. (E) Principe of calibration-less quantitative STEM measurement using pixelated STEM detector. Amount of electrons captured by individual pixels is summarised accordingly to its position on detector – angular deviation from optical axis with the vertex in the plane of the sample. Peak position of summarised annulus signal in mrad carries information about local thickness / density / composition.

beam scanning. However, it is still possible to obtain information about local thickness from such type of samples.

The use of 2D STEM detector for sample thickness estimation of $PbWO_4$ and $SrTiO_3$ crystals by PACBED (Position Averaged Convergent Beam Electron Diffraction Patterns) method[26] with achieved accuracy better than 10 % (the relation of captured and simulated patterns was done by visual comparison without automated procedure).

2 Materials and Methods

The main postulate of presented method is: the most probable scattering angle of electrons going through a sample is dependent on sample features like thickness, composition or density. The value of the most common scattering angle carries the information about those local properties and it shifts to higher values for thicker / denser samples. From the practical point of view, it is necessary to avoid the over-saturation of individual pixels which would alter the results.

As the primary electron beam is scanned over a sample (Fig. 3 A-B), individual scattering patterns are captured and stored for each beam position. Unfortunately the expected "donut" shape of scattering pattern is not visible (Fig. 3 C) because higher number of recorded electrons at higher scattering angles is distributed into more pixels (the factor of $2\pi r$). The captured images for each beam position (Fig. 3 D) are then analysed and pixel-to-centre distance is calculated. The next point is summarising the individual pixel values accordingly to their pixel-to-centre distance by

$$SRIP_x = \sum_{n=x}^{x+d} [I_n]$$

where x is the distance of pixel measured from the centre of

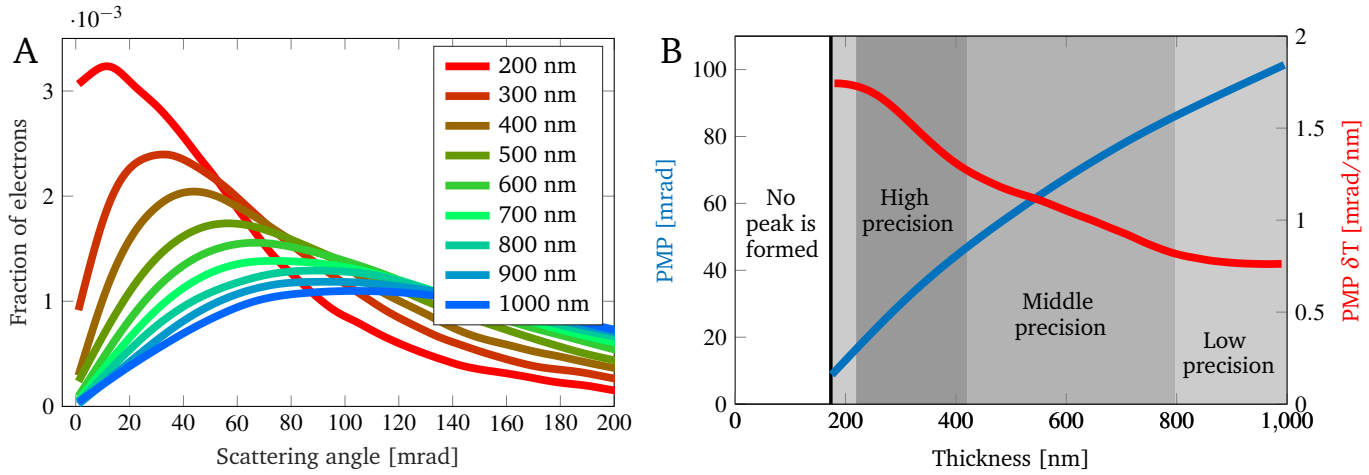

Fig. 4 Monte Carlo simulation results of latex (density of 1.05 g/cm^3, MONCA2). (A) High-angle-shift of the most common scattering angle accordingly to sample thickness. (B) Dependency of peak maximum position (PMP) on thickness (T).

the pattern in pixels, d is the summarising step (we used $d = 1$), I_n is the amount of captured electrons in pixels with distance of n. SRIP describes the dependency of captured amount of electrons on scattering angle, which is calculated from detector / sample geometry (schematically shown in Fig. 3 E). The computational inputs of the method are similar dependencies based on Monte Carlo simulation of electron scattering in a sample with known thickness, density and composition.

The key step in data processing is the detection of the most probable scattering angle in taken data. In this step, the data dimensionality is reduced from 2D matrix for each pixel to single value. This map of local characteristics is than compared with MC simulation of known samples. The value estimated by 4D-qSTEM-SRIP method is given by assignment of the simulated feature to the acquired data via same most probable scattering angle.

The use of pixelated detector brings one more advantage in the absence of detector calibration on the optical axis. When segmented STEM detector is deflected from the axis, the detection geometry does not match the MC simulation, which causes incorrect determination of the estimated resulting thickness. In case of 2D STEM detector the middle of diffraction pattern is detected at each image and detector displacement correction can be applied. The correction is in using this detected centre instead of geometrical middle of the detector for pixel to centre distance calculation used during SRIP creation.

2.1 Test samples

2.1.1 Experiment A

Latex nanospheres (density 1.05 g/cm^3, composition $[C_8H_8]_n$) of variety diameter (Fig. 3 A) were selected as a test sample for easy checking the accuracy of the 4D-qSTEM-SRIP based results. The local thickness of such type of sample is possible to compute from its geometry and the accuracy of the method can be determined. The nanospheres were mounted on home-made thin carbon ($\sim$3 nm thick) layer covered lacey carbon ($\sim$17 nm thick) supported copper TEM grid (mesh 300). For precise focusing and microscope setting the "islands" of gold are sputtered on the supporting carbon net ($\sim$1.5 nm thick layer). Both carbon and gold layers were prepared on freshly splitted mica sheet in sputter coater ACE 600 (Leica Microsystems, Vienna, Austria) and its thicknesses were estimated by oscillating crystal, mounted in its chamber.

2.1.2 Experiment B

The immiscible polymer blend PMMA/PS (polymethyl methacrylate/polystyrene in ratio 80/20; Fig. 6) was employed as a real-life sample, demonstrating a possible application area of the method. The blend consists of two amorphous polymers with similar chemical composition and density (PMMA: $[C_5O_2H_8]_n$ and ρ = 1.19 g/cm^3; and PS: $[C_8H_8]_n$ and ρ =1.05 g/cm^3). The ultrathin sections for qSTEM were prepared using an ultramicrotome (Ultracut EM UC7, Leica Microsystems, Austria). Nominal thickness of the samples (i.e. the thickness set during cutting) was 250 nm. The samples were cut at ambient temperature (ca 22°C).

2.2 Used microscope

The prepared test samples were imaged in the field free mode of a focused ion beam scanning electron microscope Helios G4 (Thermo Fisher Scientific, Waltham, USA) equipped with pixelated STEM detector T-pix (Thermo Fisher Scientific, Waltham, USA). The detector is composed of 256 × 256 pixels with pixel size of 55 μm. Total active area of detector has size 14 × 14 mm and it is mounted in detector-pole piece distance of 44 mm. In addition, it is equipped with an annular STEM III detector (Thermo Fisher Scientific, Waltham, USA). Images were captured with settings shown in Tab. 1 except common beam energy of 30 keV. The imaging was performed as individual point measurements using spot mode with discrete distances between individual beam positions. The beam shift was used for moving the beam across a sample.

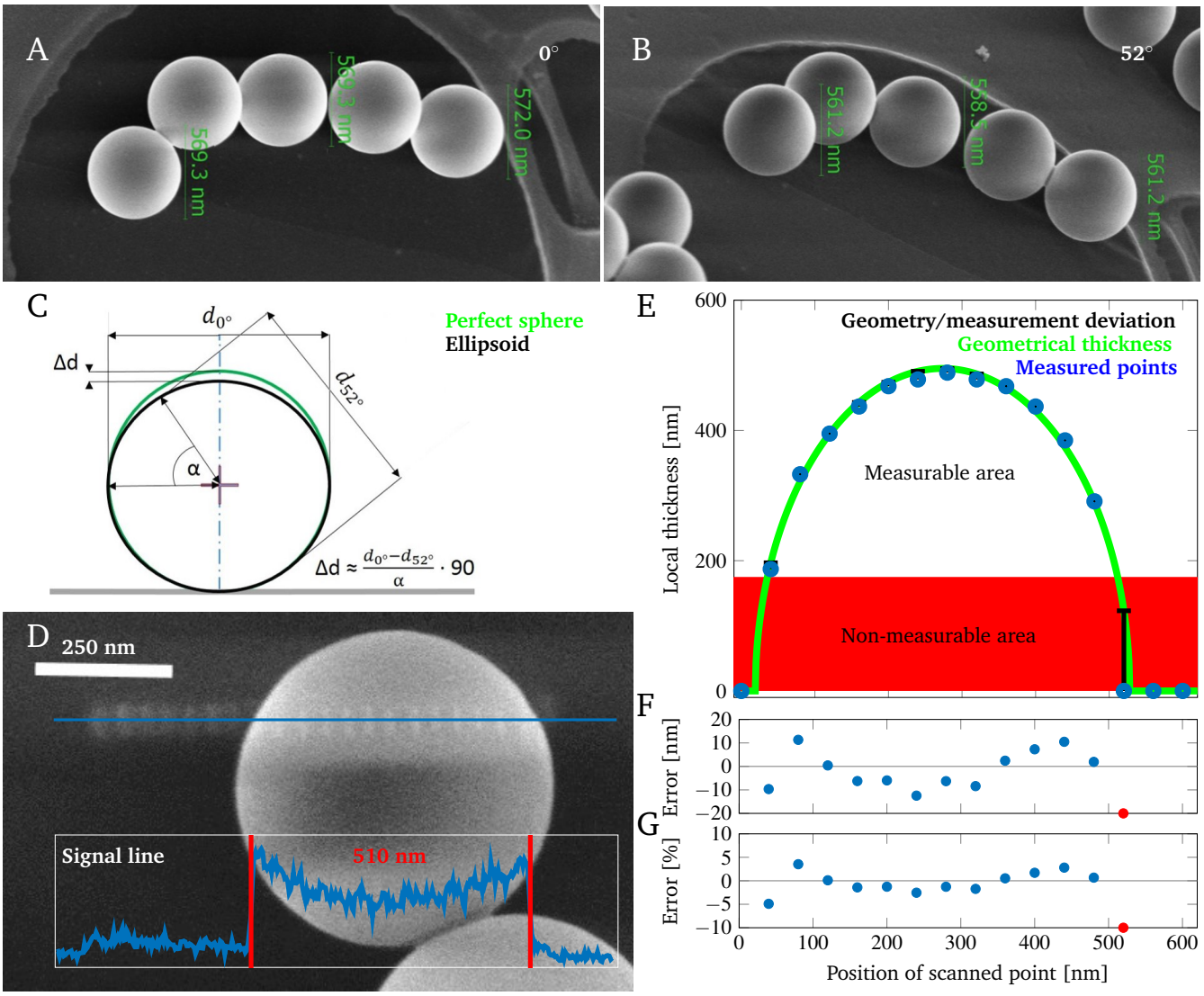

Fig. 5 Results of 4D-qSTEM-SRIP measurement. (A-B) The particles dimensions at tilting angle of 0° and 52°. (C) Geometry diagram of flattening calculation. The angle α between images is 52°. The nanosphere deformation is simplified as linear function of local geometrical thickness. (D) Measured nanosphere with visible beam scanning path caused by local damage of the sample. Diameter of the scanned section is estimated as ∼510 nm. (E) Comparison of geometry of a nanosphere with measurement. (F) Absolute thickness estimation error in nm. (G) Relative thickness estimation error in %.

Table 1 Data acquisition settings for individual experiments.

	Experiment A	Experiment B
Probe current [pA]	3.1	13
Working distance [mm]	5.3	2.9
Detector covering semiangle [mrad]	178.94	168.70
Imaging type	line scan	map
Step [nm]	40	150
Pixel time [s]	0.01	0.001
Frame integration	100	1

2.3 Monte Carlo simulation

Angle dependency of scattered electrons was simulated in Monte Carlo simulation software MONCA2* for wide range of thicknesses from 0 to 1000 nm. Selected scattering angle dependencies for thickness from 200 to 1000 nm are shown in Fig. 4 A. As visible at the graph, the position of the most probable angle shifts to higher scattering angle with increasing thickness of simulated sample. The dependency of the most common scattering angle on sample thickness is shown in Fig. 4 B. The graph is divided into several areas accordingly to the size of the change of peak maximum position (PMP) on thickness. Thicknesses under 170 nm are immeasurable by the proposed method because no

∗ MONCA2 is unpublished evolution of Monte Carlo simulation package MONCA[15] written in MATLAB (MathWorks, Natick, Massachusetts, USA).

peak is formed in captured scattering patterns - the dependency is in the form of pure decreasing function. Higher thicknesses in range from ∼200 to ∼400 nm offer high change of PMP per unit thickness and corresponding high precision of thickness estimation. This ratio is decreasing at higher thicknesses and the resolution of 4D-qSTEM-SRIP is decreasing with increasing thickness as shown in Fig. 4 B.

3 Results

3.1 Experiment A – the proof of functionality

We measured local sample thickness of our test sample to confirm the ability of calibration-less 4D-qSTEM-SRIP method as a tool for precise estimation of mass dependent characteristics of amorphous samples from its scattering patterns. Circularity control of nanospheres was achieved by imaging of those particles at two stage tilt angles (0° and 52°). The diameters of the nanospheres were measured and averaged in both projections. Example of such images is in Fig. 5 A-B. We found a slight deformation, where the nanospheres are flatter than expected. The found deviation is around 9 nm at the projection angle of 52° compared to no tilted sample. The change of nanospheres diameter was calculated accordingly to the scheme shown in Fig. 5 C as ∼ 2.9 %. This value is only approximation because we assume linear flattening in whole particle volume without any other distortions and imperfect localisation of measuring tool.

We performed line scan across individual nanoparticle (shown in Fig. 5 D) with scanning step of 40 nm for sample damage caused crosstalk, suppressing from neighboring points. Local diameter of measured circle cross-section through particle was estimated from line intensity profile and known pixel size of 2.7 nm as 510 nm.

The 4D-qSTEM-SRIP based thicknesses are compared with geometrical ones in Fig. 5 E including error Fig. 5 F-G. The plot show very good match at whole thickness range. The error is lower than 5 % in all cases which corresponds to error lower than 12 nm in absolute units. The red points in Fig. 5 F-G and long error bar in Fig. 5 E indicate the huge error of 132 nm but it can be easily explained because this value is lower than latex detection limit of 170 nm (explained in more detail in section 2.3).

3.2 Experiment B – thickness mapping

The 4D-qSTEM-SRIP method was used for the investigation of local thickness of PMMA / PS slice with nominal thickness of 250 nm. The brighter areas in Fig. 6 corresponds with PS fraction and the darker areas with PMMA (denser PMMA scatters more primary electrons to higher angles and its BF image is darker). The sample was mapped (Fig. 7 A) and the maximum peak position was calculated for each beam position. Resulting angle in mrad is shown in Fig. 7 B. As visible at this image the mean PMP of PS is higher than mean PMP of PMMA. We assume that it is caused by higher sensitivity of PMMA to the primary electron beam and corresponding mass-loss as investigated earlier on Epon resin sections[2] (local thickness of both fractions should be roughly the same). After taking into account MC simulation of PS and PMMA, two thickness maps are presented. As shown in Fig. 7 C the local thickness of PS areas is in range from 250 to 280 nm and thickness of PMMA (Fig. 7 D) in range from 190 to 240 nm. The mean thickness of PMMA fraction is lower (compared to nominal or PS) due to induced mass reduction during data acquisition. Interesting point is thickness inhomogeneity caused by the plastic deformations during cutting. The line at the bottom of the measured area is caused by an error in beam scanning / moving the microscope stage and corresponding shift of measuring spots.

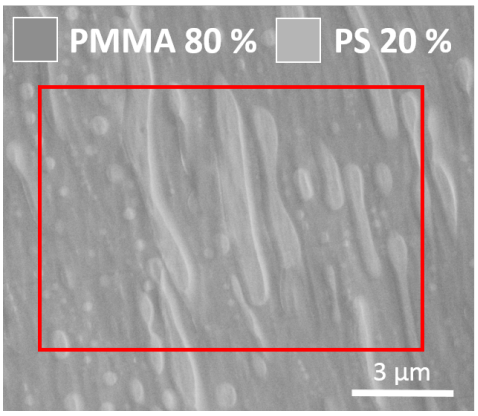

Fig. 6 Slice of PMMA / PS used as demonstration sample of possibilities of the 4D-qSTEM-SRIP method. The red rectangular shows the area of thickness mapping.

4 Discussion and Conclusions

We confirmed the usability of our method 4D-qSTEM-SRIP – calibration-less local thickness estimation of amorphous samples using pixelated STEM detector – for high magnification characterisation of samples and corresponding estimation of local properties like thickness, mass per area or mass per length. The achieved accuracy is better than 5 %, which we consider as a very good result for point based analysis. Refinement of the results can be achieved by averaging the results from areas of the same thicknesses. The higher error around middle of the particle could be caused by higher particle flattening than computed from tilted images, its deformation and degradation under impacting electrons or lower PMP modulation at those thicknesses.

The main advantages of the method are redundancy of intensity based detector calibration and straight forward results interpretation – we do not have problem with contrast interpretation for thick samples as in case of the use of annular STEM segments[27] or two resulting thicknesses for one measured signal intensity as described in[28]. On the other hand, an expensive detector with high homogeneity of individual pixel response is necessary and the method is limited in usable range of the thicknesses, which can be determined – it is given by creation of detectable peak at low scattering angles for low thicknesses instead of pure decreasing dependency. This range is dependent on the composition of a sample and its density – denser sample composed of elements with higher Z is measurable from lower thicknesses. All advantages and disadvantages are summarised below.

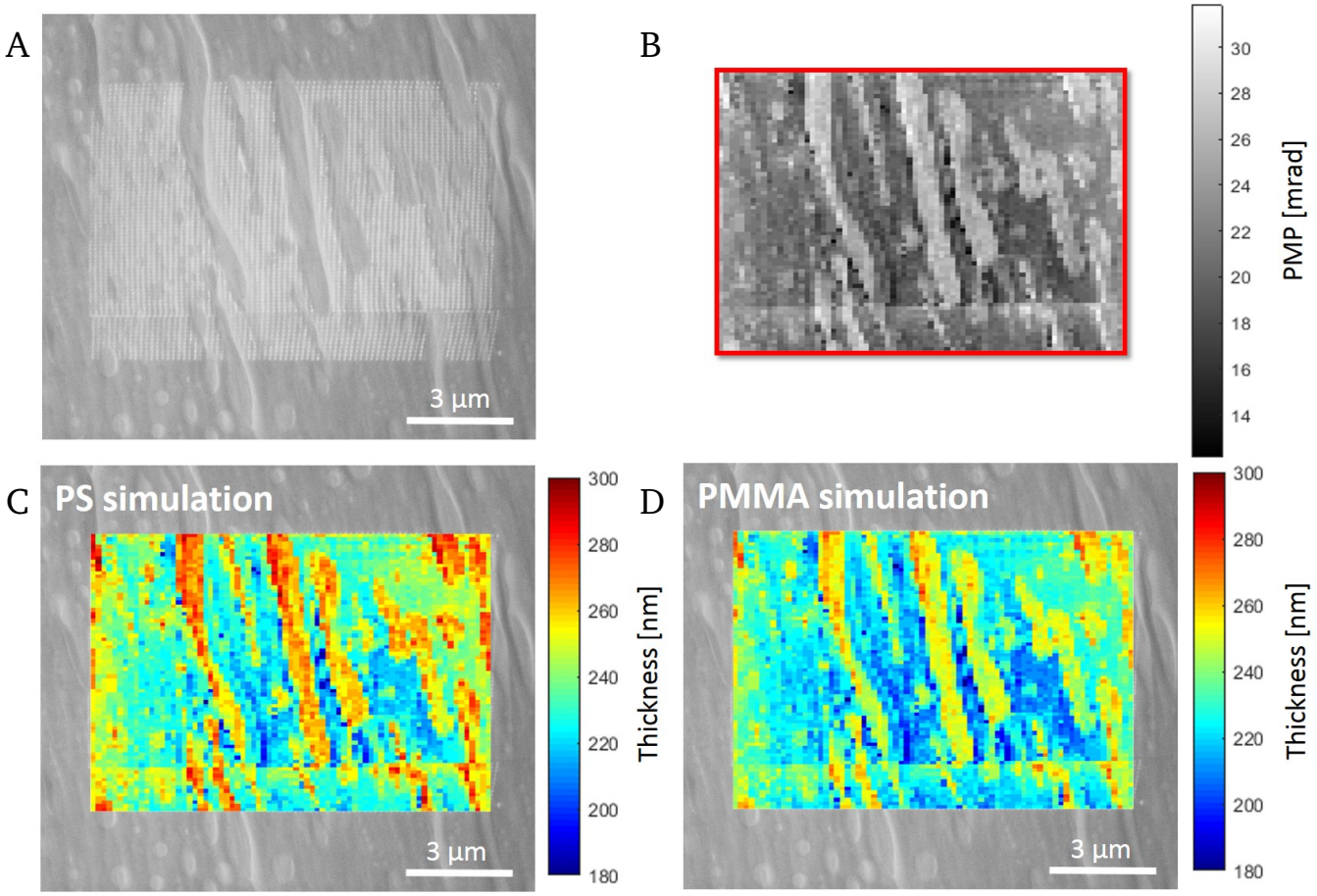

Fig. 7 Local thickness mapping of PMMA / PS mixture. (A) Test sample after irradiation by primary electron beam. Raster of scanned points is visible in areas of PMMA – there is a significant mass-loss compared to PS areas, where no bright points are visible. (B) Calculated position of peak maximum in mrad. (C) Local thickness based on Monte Carlo simulation of PS. (D) Local thickness based on Monte Carlo simulation of PMMA.

PROS
Independent on beam current change during an imaging session.
Independent on detector-optical axis coaxiality.
Does not require detector calibration.
Applicable post-acquisition.

CONS
Limited usable thickness range.
Sensitivity is dependent on measured thickness / sample.
Expensive pixelated STEM detector.
Longer pixel dwell time – slower scanning.

We assume that presented quantitative STEM imaging using pixelated detector will find its use and bring novel method for investigation of various amorphous samples.

Conflicts of interest

There are no conflicts to declare.

Acknowledgements

The research was supported by the Technology Agency of the Czech Republic (project TN01000008), the Ministry of Industry and Trade of the Czech Republic (project TRIO FV30271); the infrastructure by the Czech Academy of Sciences (project RVO:68081731). The authors thank Thermo Fisher Scientific Brno for providing the FIB-SEM Helios equipped with the T-pix detector (based on TimePix technology).

References

1 M. Müller, P. Veit, F. F. Krause, T. Schimpke, S. Metzner, F. Bertram, T. Mehrtens, K. Müller-Caspary, A. Avramescu, M. Strassburg, A. Rosenauer and J. Christen, *Nano Letters*, 2016, **16**, 5340–5346.

2 R. Skoupy, J. Nebesarova, M. Slouf and V. Krzyzanek, *Ultramicroscopy*, 2019, **202**, 44–50.

3 A. Sen, U. Baxa, M. N. Simon, J. S. Wall, R. Sabate, S. J. Saupe and A. C. Steven, *Journal of Biological Chemistry*, 2007, **282**, 5545–5550.

4 S. A. Müller and A. Engel, *Micron*, 2001, **32**, 21–31.

5 Z. Barkay, I. Rivkin and R. Margalit, *Micron*, 2009, **40**, 480–485.

6 E. Buhr, N. Senftleben, T. Klein, D. Bergmann, D. Gnieser, C. G. Frase and H. Bosse, *Measurement Science and Technology*, 2009, **20**, year.

7 M. Dapor, N. Bazzanella, L. Toniutti, A. Miotello and S. Gialanella, *Nuclear Instruments and Methods in Physics Research, Section B: Beam Interactions with Materials and Atoms*, 2011, **269**, 1672–1674.

8 M. Dapor, N. Bazzanella, L. Toniutti, A. Miotello, M. Crivellari and S. Gialanella, *Surface and Interface Analysis*, 2013, **45**, 677–681.

9 H. Kim, T. Negishi, M. Kudo, H. Takei and K. Yasuda, *Journal of Electron Microscopy*, 2010, **59**, 379–385.

10 A. Garitagoitia Cid, R. Rosenkranz, M. Löffler, A. Clausner, Y. Standke and E. Zschech, *Ultramicroscopy*, 2018, **195**, 47–52.

11 T. Volkenandt, E. Müller, D. Z. Hu, D. M. Schaadt and D. Gerthsen, *Microscopy and Microanalysis*, 2010, **16**, 604–613.

12 T. Volkenandt, E. Müller and D. Gerthsen, *Microscopy and Microanalysis*, 2014, **20**, 111–123.

13 M. Pfaff, E. Müller, M. F. G. Klein, A. Colsmann, U. Lemmer, V. Krzyzanek, R. Reichelt and D. Gerthsen, *Journal of Microscopy*, 2011, **243**, 31–39.

14 R. Skoupy, T. Fort and V. Krzyzanek, *Nanomaterials*, 2020, **10**, 332.

15 V. Krzyzanek and R. Reichelt, *Microscopy and Microanalysis*, 2003, **9**, 110–111.

16 C. Ophus, *Microscopy and Microanalysis*, 2019, **25**, 563–582.

17 S. Fang, Y. Wen, C. S. Allen, C. Ophus, G. G. D. Han, A. I. Kirkland, E. Kaxiras and J. H. Warner, *Nature Communications*, 2019, **10**, 1127.

18 P. Wang, F. Zhang, S. Gao, M. Zhang and A. I. Kirkland, *Scientific Reports*, 2017, **7**, 2857.

19 O. Panova, C. Ophus, C. J. Takacs, K. C. Bustillo, L. Balhorn, A. Salleo, N. Balsara and A. M. Minor, *Nature Materials*, 2019, **18**, 860–865.

20 B. W. Caplins, J. D. Holm and R. R. Keller, *Carbon*, 2019, **149**, 400–406.

21 O. Panova, X. C. Chen, K. C. Bustillo, C. Ophus, M. P. Bhatt, N. Balsara and A. M. Minor, *Micron*, 2016, **88**, 30–36.

22 X. Mu, A. Mazilkin, C. Sprau, A. Colsmann and C. Kübel, *Microscopy*, 2019, **68**, 301–309.

23 C. Ebner, R. Sarkar, J. Rajagopalan and C. Rentenberger, *Ultramicroscopy*, 2016, **165**, 51–58.

24 C. Gammer, C. Ophus, T. C. Pekin, J. Eckert and A. M. Minor, *Applied Physics Letters*, 2018, **112**, 171905.

25 D. R. Mitchell and T. C. Petersen, *Microscopy Research and Technique*, 2012, **75**, 153–163.

26 J. M. LeBeau, S. D. Findlay, L. J. Allen and S. Stemmer, *Ultramicroscopy*, 2010, **110**, 118–125.

27 J. Holm, B. Caplins and J. Killgore, *Ultramicroscopy*, 2020, **212**, 112972.

28 R. Skoupy and V. Krzyzanek, 10th Anniversary International Conference on Nanomaterials - Research & Application; NANOCON, 2018, pp. 677–681.

B.3 Nanoscale estimation of coating thickness on substrates via standard less BSE detector calibration

R. Skoupy, T. Fort, and V. Krzyzanek. Nanoscale estimation of coating thickness on substrates via standard less BSE detector calibration. *Nanomaterials*, 10(2):332, 2 2020. doi:10.3390/nano10020332

nanomaterials

MDPI

Article

Nanoscale Estimation of Coating Thickness on Substrates via Standardless BSE Detector Calibration

Radim Skoupy, Tomas Fort and Vladislav Krzyzanek *

Institute of Scientific Instruments of the Czech Academy of Sciences, Kralovopolska 147, CZ-61264 Brno, Czech Republic; radim.skoupy@isibrno.cz (R.S.); fortt@isibrno.cz (T.F.)

* Correspondence: krzyzanek@isibrno.cz

Received: 7 January 2020; Accepted: 12 February 2020; Published: 15 February 2020

Abstract: The thickness of electron transparent samples can be measured in an electron microscope using several imaging techniques like electron energy loss spectroscopy (EELS) or quantitative scanning transmission electron microscopy (STEM). We extrapolate this method for using a back-scattered electron (BSE) detector in the scanning electron microscope (SEM). This brings the opportunity to measure the thickness not just of the electron transparent samples on TEM mesh grids, but, in addition, also the thickness of thin films on substrates. Nevertheless, the geometry of the microscope and the BSE detector poses a problem with precise calibration of the detector. We present a simple method which can be used for such a type of detector calibration that allows absolute (standardless) measurement of thickness, together with a proof of the method on test samples.

Keywords: SEM; quantitative imaging; back-scattered electrons; standardless calibration; electron mirror; sample bias; Monte Carlo simulation; thin coating layers

1. Introduction

A scanning electron microscope (SEM) is a powerful method for examining many types of samples [1–4]. As the primary electron beam interacts with a sample, a wide spectrum of signals, carrying information about different physical properties of the sample, is generated [5]. The detection possibilities differ among individual types of SEMs, but secondary and back-scattered electron signals are the most common ones. We focus in detail on calibrated image acquisition of back-scattered electrons (BSE) using a retractable circular BSE detector (CBS), which compared to in-lens BSE detectors offers well-defined detection geometry without distortions caused by the optical system of the SEM column (in the field free mode of the final demagnifying lens).

BSE imaging (BSEi) is an often-used method for differentiation of elements with a different atomic mass in a sample thanks to its mass contrast [5]. The signal captured by the BSE detector is dependent on several factors such as elemental composition and its corresponding back-scattering coefficient, local thickness of individual layers or grains, local density, energy of the primary electron beam, collecting angle of the BSE detector and application of beam deceleration [6–8].

We have continued previous work where the back-scattering coefficient is estimated as a function of the over-layer thickness [9,10]. The authors there used Pd and Au layers on a Si substrate, the thicknesses of which were estimated using calibrated BSE imaging together with Monte Carlo simulation. Unlike the authors of that study, we focus on much smaller thicknesses (<25 nm). The BSE coefficient η is theoretically described for those thicknesses using an example of an Au layer on a C substrate and a C layer on an Au substrate in [11].

Calibration of the BSE detector response to the primary electron beam plays a crucial role for precise data acquisition and corresponding data processing where captured data are compared with simulated signal intensities. The limits or calibration points bring a connection between the experiment

and simulation and thus allow assigning the correct covering layer thickness to the corresponding BSE signal. Several approaches for calibration of the BSE signal have recently been published:

One tail relative calibration—upper limit [9] where the BSE images of thin Pd layers on a silicon wafer are normalized by the BSE signal of bulk Pd. The same detector settings for all samples were achieved by simultaneous imaging of all four samples (Pd bulk, Pd 10 nm, Pd 110 nm, and Pd 270 nm), and the BSE intensities are compared to each other. The same calibration was applied also in the case of measurement of Au layers on a Si substrate [10], where the upper limit is a measured BSE coefficient from bulk Au.

One tail relative calibration—bottom limit [12] is based on image background measurement in the vacuum part of a "sample". The upper limit is then floating just under the saturation limit of the detector. This detector calibration was applied for the determination of the In_xGa_{1-x}/GaAs ratio in the wedge-shape sample that was prepared by a gallium focused ion beam SEM (FIB-SEM). The density of a sample with changing composition was determined by linear interpolation of pure GaAs and InAs densities. The local thickness is calculated from the sample geometry of the wedge shape. Such measurements were analogically performed also for very thin samples using a scanning transmission electron microscopy (STEM) detector [13].

Two tail relative calibration [14], where the captured signal is normalized between two defined limiting values. Here, the BSE signal of the Si substrate is used as the lower limit and the signal of the Au substrate is used as the upper limit. Another combination of limits is the detector response to the blanked beam as the lower limit and the BSE signal of the crystalline Si sample as the upper limit [15].

Multi-point relative calibration [16] uses 26 mineral standards describing the correlation of the BSE signal on the changing atomic number Z in the range from 10.41 to 73.16. The atomic number Z of an unknown sample can be determined with maintaining the imaging conditions from the measured BSE signal—Z dependency.

All of the above-mentioned methods for calibration of the BSE detector are relative to chosen limits and therefore dependent on the calibration sample. The disadvantage is the possible variation of those limits with the use of different calibration standard qualities, cleanliness, and homogeneity.

The principle of quantitative BSE or STEM imaging is based on a comparison of captured and normalized image data with a theoretical model. Although a few empirical equations describing the BSE yield have been described [17], in practice, computer simulations usually based on the Monte Carlo methods are typically used which also include the SEM column and the BSE geometries. There are several types of software available where electron–matter interaction can be simulated. They differ in the incorporated physical models, the possibilities for sample definition, data exporting, or computed physical characteristics. The principle of quantitative STEM imaging is described in more detail in [18–20].

The maximum measurable layer thickness by qBSEi is given by the acceleration voltage and the corresponding penetrability into the sample [21]. Higher acceleration voltage brings a wider measurable range of thicknesses, but with lower modulation of the signal by unit thickness change. It follows that, for high-precision with thin layers, a lower acceleration voltage is preferred and, for a high measurable range of thicknesses, a higher beam energy should be used. An example of the penetrability of a 3 kV electron beam is shown in Figure 1A,B, where the beam partially goes through 6 nm of Mo but is fully absorbed in a layer of 25 nm.

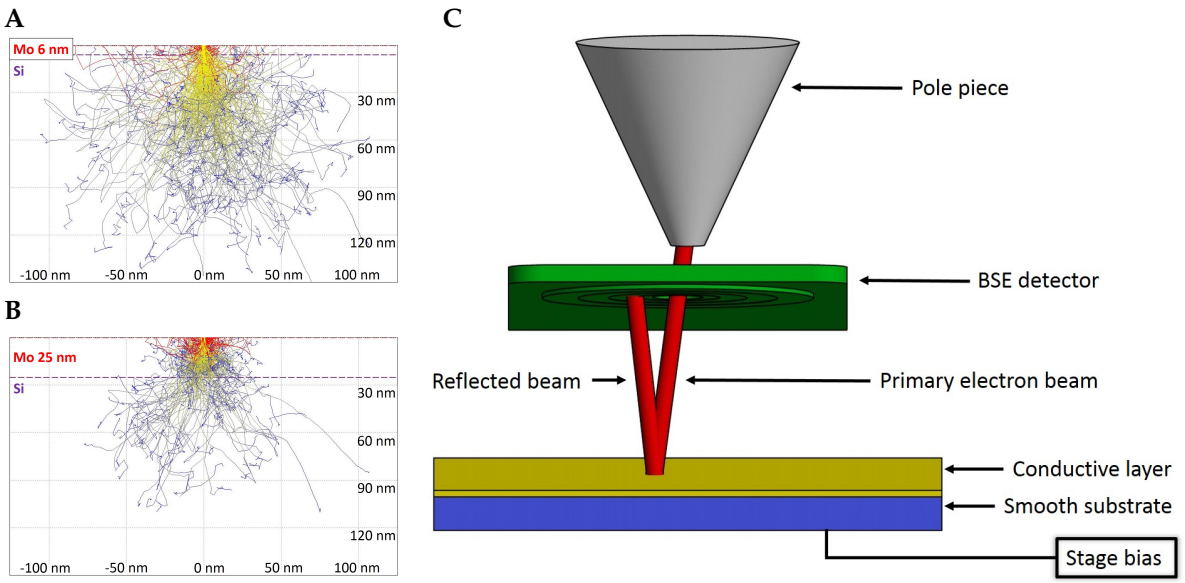

Figure 1. (**A**,**B**) trace of primary electrons hitting the sample, showing the principle of signal change accordingly to increasing coating layer thickness. The back-scattering coefficient is increasing with thickness of the coating layer (in the case that the covering layer has higher back-scatter electron (BSE) yield than the substrate). For example, in the case of a 6 nm thick layer of Mo on a Si substrate (**A**) most of the primary electrons penetrate the Mo layer and thanks to the lower BSE yield of Si the resulting BSE coefficient is lower than in the case of 25 nm Mo (**B**) where nearly all electrons are absorbed or back-scattered in the layer, simulated in CASINO version 2.51; (**C**) principle of the calibration of full beam on the BSE detector. Primary electron beam (red) is reflected on biased conducting surface (gold) created on smooth substrate (blue) back to the BSE detector (green).

2. Materials and Methods

2.1. Microscope Used

The test samples were imaged in the field free mode of a scanning electron microscope Magellan 400 L (FEI-Thermo Fisher Scientific, Waltham, MA, USA) equipped with a commercial four annular segment CBS detector (FEI). The imaging was performed with the following settings: the acceleration voltage of 3 kV, magnification in the range from 1000 to 500,000×, the probe current of 50 pA, resolution of 1024 × 884 pixels in each individual recorded image, the working distance of 4 mm, the distance from the pole-piece to the active detector plane of 1 mm, and the dwell time of 10 µs. All images were captured as 16 bit to keep high dynamics. Well-adjusted SEM including a centered BSE detector according to the optical axis is a prerequisite for quantitative measurements. For data collection, the innermost detector segment of the BSE detector (S1) was used because it is possible to take the calibration image of the whole segment under the same imaging conditions. The active area of the annular segment S1 is given by the diameter range from 0.75 to 1.25 mm that, for the above-mentioned settings, corresponds to the collection angles in the range of 124.4 to 205.4 mrad.

2.2. Absolute Detector Calibration

We present a two-tail absolute calibration method for a BSE detector that uses the detector response to no impacting electrons as a bottom limit and all primary electrons impacting the detector for the upper limit. Moreover, the method includes correlation of the captured BSE signal with the position and energy of the impacting electrons.

The background level of the BSE detector that is related to the brightness setting of the SEM is determined when no beam is hitting the sample, i.e., the lower calibration limit is calculated as the mean value of all pixel values in the recorded beam blanked image. It is necessary to avoid under-saturation. The acquired images are then normalized between those limiting values by the equation:

$$I_{norm} = \frac{I_{sample} - I_{blank}}{I_{full} - I_{blank}}$$

where I_{norm} is the normalized image intensity towards the actual beam current and detector contrast/brightness settings, I_{sample} is the original intensity, I_{blank} is the mean value in blanked image, and I_{full} is the signal intensity of full beam on the detector.

In the case of calibration of the BSE detector using the full beam, the geometry of the detector inside the microscope chamber does not allow for performing this directly as is typically used in qSTEM. The STEM detector is located under a sample and primary electrons may impact the STEM detector directly, in the case of the retractable BSE detector that is located immediately under the SEM column pole piece and therefore not in the field of view for the primary electrons. However, the solution could be to reverse the electron trajectories by applying appropriate negative stage bias to the sample and impact of the electrons on the BSE detector from its sensitive side as shown schematically in Figure 1C. For that purpose, a gold coated circular piece of glass with a diameter of 10 mm was prepared. Note that it is necessary to avoid over-saturation.

Unfortunately, in the case of the microscope used, the primary beam energy set by the user is the landing energy and so the SEM operating software raises the primary beam energy when negative stage bias is applied. In order to overcome this limitation, an external voltage source BERTAN 225 (Spellman, New York, NY, USA) connected directly to the sample stage was used.

For precise simulation of the captured signal, the detector response factor (DRF) for the electrons with different energies and positions of impact is introduced as follows. In order to estimate the DRF, a series of BSE detector images (Figure 2A) with a beam energy in the range from 500 to 3000 eV was captured. In the captured images of the BSE detector, the centers of the individual segments were detected and circular averages were performed (shown in Figure 2C). The results were used (after interpolating to non-measured energies) to determine the space and energy-dependent DRF for each individual simulated back-scattered electron. The actual beam current (Figure 2B) was measured by the Faraday cup mounted on the microscope stage using the picoammeter KEITHLEY 6485 (Keithley Instruments, Cleveland, OH, USA).

2.3. Test Samples

Three types of representative samples were used to show the proof of the described method. Very thin layers of chromium, molybdenum, and gold of known thickness were sputtered on a silicon wafer. The accurate thicknesses of the sputtered thin layers were estimated by the calibrated sputtering speed and the number of passes under the sputtering head. The sputtering speed was estimated from the thickness of the layer estimated by profilometry and the known number of passes. A cleaned silicon wafer with size of 10 × 10 mm was used as the substrate in all cases.

The chromium and molybdenum layers were prepared in an sputtering system B-301-308 (AURION, Seligenstadt, Germany) at a pressure of 9.9×10^{-5} Pa. The target was cleaned in an Ar athmosphere for 300 s by discharge. The high-frequency source power was 300 W. The flow of Ar was 20 sccm. The substrates were cleaned before covering by glow discharge with a power of 150 W for 120 s (rotation regime with speed 9 rpm, Ar pressure of 0.274 Pa).

In the case of molybdenum, the voltage on the magnetron was stabilized to −62 V. The pressure of the working gas in the chamber during sputtering was 0.162 Pa. The deposition was done in pulse regime ±45° and at a speed of 1.536 rpm. The thickness after 180 s sputtering was estimated by a profilometer Taylor–Hobson Talystep as 30 nm. For a layer thickness of 25 nm, the time was reduced to 150 s, for 20 nm to 120 s, for 15 nm to 90 s, for 8 nm to 48 s, for 3 nm to 18 s, and for 1 nm to 6 s.

In the case of chromium, the voltage on the magnetron was −52 V, and a chamber pressure of 0.160 Pa, a speed of 1.536 rpm, and a sputtering time of 400 s were used with a resulting layer thickness of 92 nm. The deposition time for the 25 nm layer was 108 s, for 20 nm 87 s, for 15 nm 65 s, for 8 nm 35 s, and for a 3 nm layer 13 s and 5 s for 1 nm.

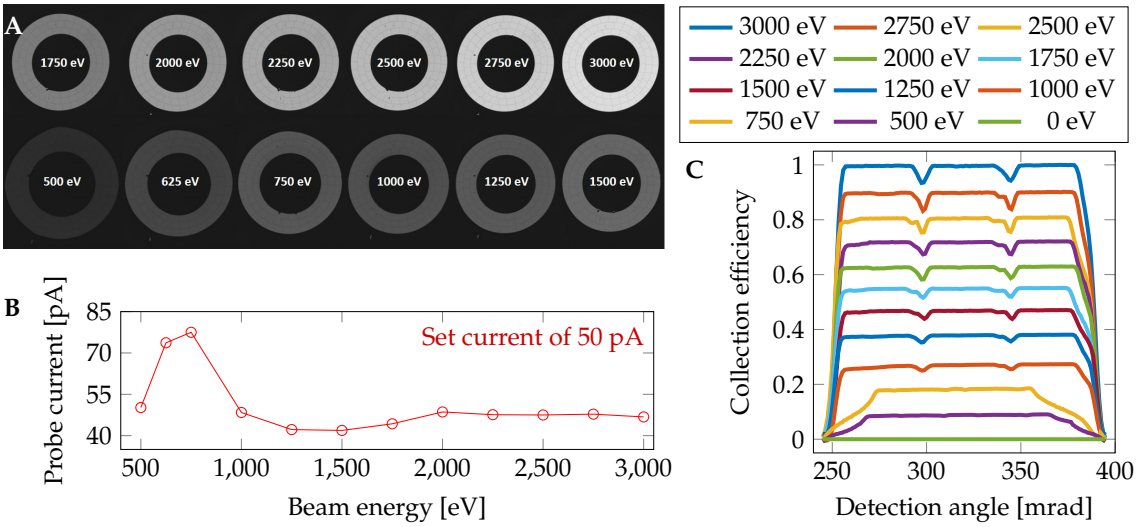

Figure 2. (**A**) set of BSE detector calibration images for the innermost segment at various electron energies of the primary beam. The change in diameter of the detector segment at individual electron energies is caused by image distortions during its reflection; (**B**) probe current measurements at used electron energies. Together with changing the electron beam energy, the probe current impacting the sample is changing and it is necessary to correct it; (**C**) calibration of the BSE detector according to primary beam energy and position of electron impact. Because of the rotational symmetry of the detector, only the back-scattering angle is considered. A working distance of 4 mm and a distance of the pole piece and the detector of 1 mm were used.

The gold layers were prepared at room temperature from the gold target of (99.9% purity) in an argon (99.999%) discharge in a commercially available Z 550 RF magnetron sputtering plant (Leybold Heraeus, Cologne, Germany). During the deposition, the power was held at 100 W and the pressure of argon was 0.150 Pa. The evacuation system consists of a rotary and turbomolecular pump, and limited pressure is 10^{-4} Pa. In such a way, a series of layers with thicknesses of 1.7, 3.4, 5.1, 6.7, 8.5, 11.9 and 13.4 nm were prepared.

2.4. Theoretic Description of the BSE Signal

The signal captured by the BSE detector is given by the back-scattering coefficient, angular distribution of BSEs, energy of individual BSEs, and local sensitivity of the BSE detector used (discussed in more detail in Section 2.2). In this part, we focus on the simulation of electron–matter interaction and the calculation of the amount of energy transferred to BSE detector from a sample with a known composition and detection geometry.

The Monte Carlo simulations, which describe well the electron scattering in a sample of matter, were done in the software CASINO version 3.3.0.4 [22] in an appropriate range of coating layer thicknesses from 0 to 28 nm (Cr and Mo) and from 0 to 16 nm for Au. Several physical models for total and partial cross sections such as Mott, Rutherford, and Reimer models were investigated, but, finally, the physical model Elsepa [23] was used in this work as it gives the most accurate results.

Each simulation was based on 300,000 impinging electrons in order to suppress statistical error. Simulated BSE coefficients accordingly to the coating thickness are shown in Figure 3C and the calculated captured energy fraction (CEF) in Figure 3D. The fraction of detected energy is estimated from information about energy and back-scattering angle (an example for 3 nm and 25 nm layers can be seen in Figure 3A,B) of each simulated electron as used in [24,25]. For data processing, the results of the MC simulation were analyzed in MATLAB (Mathworks).

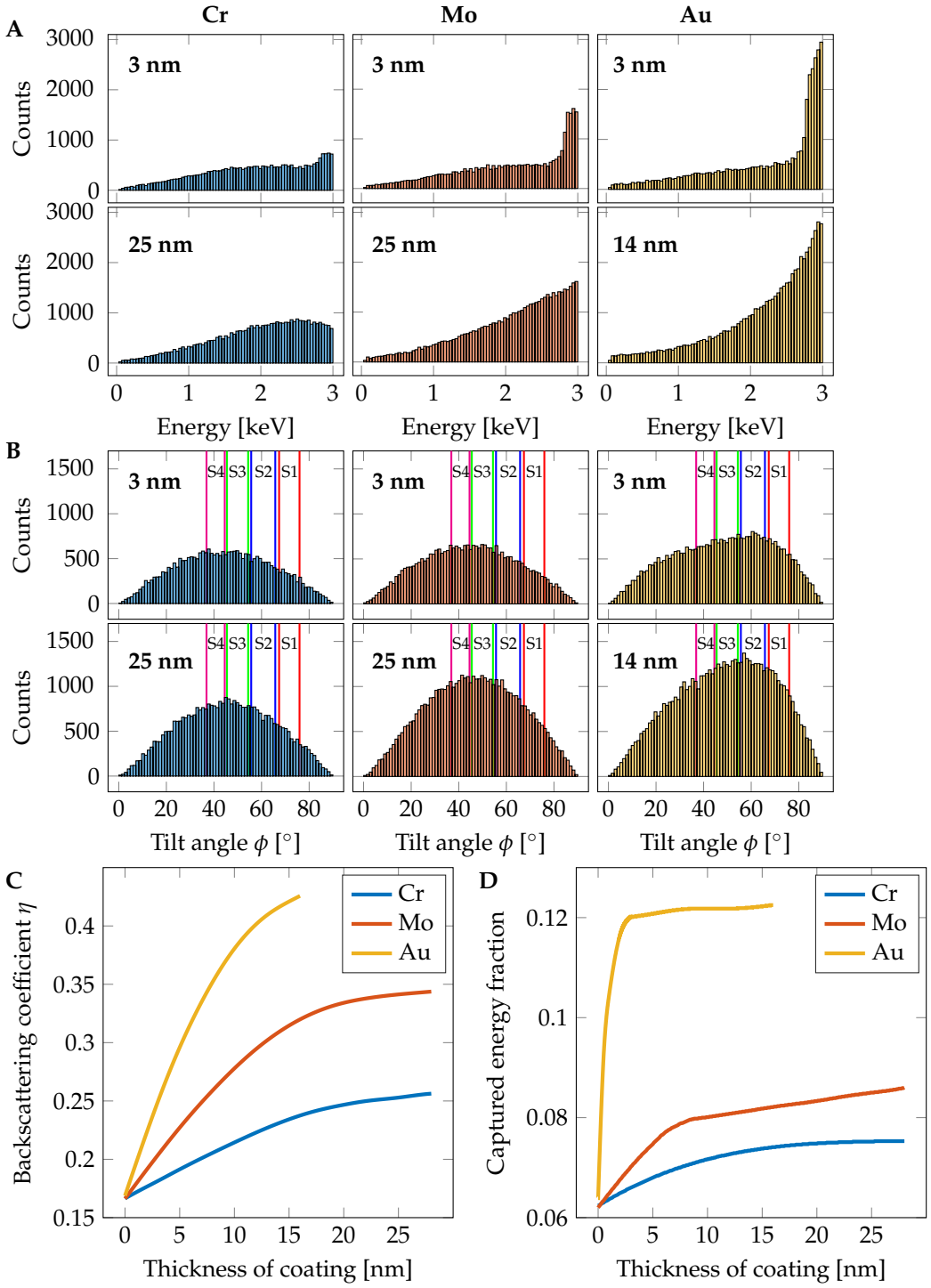

Figure 3. Monte Carlo simulation based inputs of the method. (**A**) With increasing coating thickness, the amount of middle energy BSE increases and enhances the total energy emitted from the sample. The peak just under the landing energy of 3 kV is caused by reflection in the coating layer. The rest of the energy spectrum is caused by the Si substrate. (**B**) The elements with higher atomic number reflect the impacted electrons closer to the optical axis ($\phi = 0$ is plain of a sample surface) and thus increase the signal captured by the BSE detector. Collecting angles of individual detector segments S1–S4 is highlighted; (**C**) dependency of back-scattering coefficient η on the thickness of Cr, Mo and Au coatings on a Si substrate; (**D**) captured energy fraction according to the chosen element and coating thickness. The fraction was calculated from the scattering angle and energy of each BSE.

The simulated BSE signal SBS_x generated by coating layer of element α with thickness x on the substrate β is calculated by the equation:

$$SBS_x = \eta_x \cdot CEF_x = \eta_x \cdot \frac{\sum_{i=1}^{c} E_i \cdot DRF_{E,\sigma}}{\sum_{i=1}^{t} E_i \cdot DRF_E},$$

where η_x is the BSE coefficient of a layer with thickness x, E_i is the energy of the electron i, c is the amount of the BSE captured by the detector, t is amount of all BSE and $DRF_{E,\sigma}$ is the detector response factor of an electron with energy E and position of impact given by the angle σ. The atomic number Z_α is higher than Z_β in the case of test samples.

3. Results

Thicknesses of coating layers on prepared samples with very good precision were measured using the herein-described new method. A higher error is visible in the case of a low-thickness region, where the simulation does not match experimental measurements very well. As visible in the graphs in Figure 4 and numerically in Table 1, the results for chromium are lower than expected in all examined cases. This could be caused by oxidation of those layers during the transfer of the sample from the sputter coater chamber to the SEM in air. An additional experiment had proven the oxidation of the chromium layers and consequently the change in estimated thickness (MC simulations are done for pure Cr). For suppression of such surface change caused by air exposure, a sample of chromium was prepared in the sputter coater ACE600 (Leica Microsystems, Vienna, Austria) and directly transferred into the SEM chamber via a vacuum transfer shuttle VCT100 (Leica Microsystems, Vienna, Austria) without leaving the high vacuum. The thickness of the layer was estimated as 11.14 nm in the case of no air exposure and 9.37 nm after 30 min in air. The results after one more hour in the air were the same as after half an hour. This shows fast oxidation of the pure chromium surface and creation of a Cr_xO_y layer.

Table 1. Results of qBSEi measurements.

	Nominal [nm]	qBSEi [nm]	Error [nm]	Error [%]
Au	1.7	0.50	−1.20	−70.8
	3.4	2.63	−0.77	−22.7
	5.1	4.42	−0.68	−13.3
	6.7	6.29	−0.41	−6.1
	8.5	8.08	−0.42	−4.9
	11.9	11.04	−0.86	−7.2
	13.4	13.52	0.12	0.9
Mo	1.0	1.23	0.23	23.1
	3.0	3.57	0.57	19.0
	8.0	9.13	1.13	14.1
	15.0	16.07	1.07	7.1
	20.0	19.99	−0.11	−0.1
	25.0	25.03	0.03	0.1
Cr	1.0	−1.39	−2.39	−239.4
	3.0	2.15	−0.89	−29.5
	8.0	7.18	−0.82	−10.3
	15.0	13.56	−1.44	−9.6
	20.0	16.09	−3.91	−19.5
	25.0	18.81	−6.19	−24.8

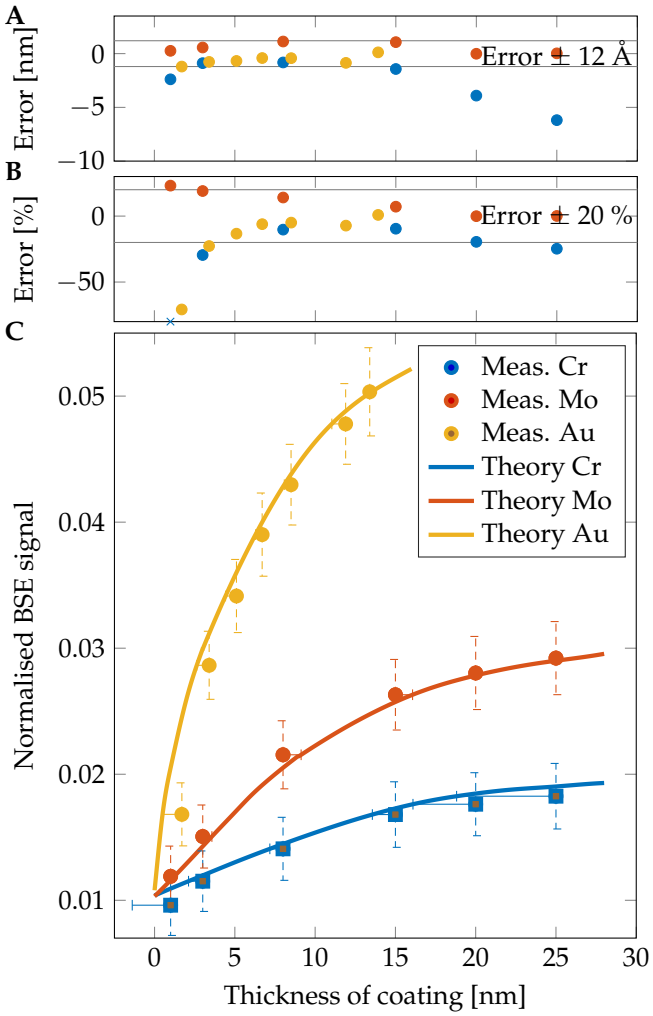

Figure 4. Results of qBSE imaging. (**A**) comparison of measured and nominal thicknesses. Most of the measurements show an error lower than 1.2 nm; (**B**) comparison of measured and nominal thicknesses. Most of the measurements show an error lower than 20%. The blue × mark shows a data point out of the used *y*-axis range; (**C**) theoretical BSE signal captured by an S1 segment in WD of 4 mm for Cr, Mo, and Au. The individual points show mean values of measured samples with its standard deviation and horizontal lines indicate the thickness assigned by qBSEi. The oxidized layer of Cr is highlighted by square marks.

In the case of Mo and Au layers, the estimation error is decreasing with the increasing thickness of the coating layer. In the case of Mo, the error is decreasing from 23% (1 nm) through 7% (15 nm) to 0.1% for a 25 nm thick layer. The Au gives a high error of 70% at 1.7 nm, but the error is rapidly decreasing up to an accuracy of 0.9% in the case of a 13.4 nm layer. All results are shown in Table 1.

An advantage of the presented method is a wide magnification range and the corresponding spatial resolution which can be achieved. In general, it is based only on maximum resolution of the SEM used and the rapidity by which a creation of hydrocarbon contamination layer is created which decreases the measured thickness. For estimation of the change of the estimated coating layer thickness, the molybdenum sample with a nominal thickness of 8 nm was used (the thickness estimated by qBSEi is around 9.3 nm). A comparison of measurements at a wide range of magnifications from 1000× up to 500,000× is shown in Figure 5. We found high accuracy across all the magnification range with a deviation around 0.1 nm. This brings an opportunity to measure the space dependency of coating thickness at all magnifications.

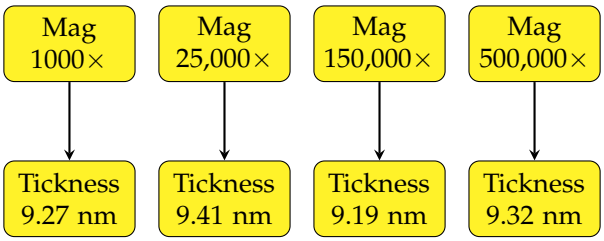

Figure 5. Change of estimated thickness of a molybdenum layer on a silicon wafer according to image magnification.

4. Discussion and Conclusions

We presented and proved a new calibration method for retractable BSE detectors mounted in the vacuum chamber of an SEM. Using the electron mirror BSE detector calibration, it is possible to measure the response of the detector to the primary beam, which is necessary for precise measurements and comparison of measured images. Using this approach, it is possible to measure the energy and spatial dependent response of the BSE detector which is usually unavailable without detector dismounting.

The measured thicknesses match the nominal ones very well (note that the nominal thicknesses are not entirely accurate and may slightly vary) because we achieved an accuracy of around several tenths of a nm in most cases. Thanks to the precise BSE detector calibration, we achieved better results with low-thickness films than is described in [9], where the thickness of a 10 nm Pd layer was immeasurable and, in the case of a 25 nm Au layer, an error of 20% was attained [10]. We achieved an error lower than 10% for an Au layer down to a thickness of 6.7 nm and, even in the case of a 5.1 nm Au layer, the error was only 13%. The high error at lower thicknesses (3.4 and 1.7 nm) is probably caused by low layer thickness homogeneity and creation of "metal islands" on the substrate during preparation of the layer as shown in [26]. Another source of inaccuracy is the sample being covered by a hydrocarbon contamination layer, which changes the BSE coefficient and the BSE energy distribution accordingly to its thickness and corresponding penetrability of the primary electron beam through the contamination layer [6,11,27,28].

For its accuracy, the method can be used as a non-destructive control of thin layer thickness during the preparation process in the semiconductor industry or manufacturing of thin coatings on optical elements.

Further improvement can be achieved by using all available BSE detector segments for image acquisition. This upgrade requires complex calibration of each individual segment and measuring its angle/space-dependent response factor. We would like to focus on this in a subsequent study. We suppose that a measurement accuracy around 0.5 nm is possible with enhanced detection angles, a higher number of simulated electrons, and precise positioning of the BSE detector in the SEM chamber.

Author Contributions: Conceptualization, R.S. and V.K.; methodology, R.S.; software, R.S.; validation, R.S. and V.K.; formal analysis, V.K.; investigation, R.S.; resources, V.K.; data curation, R.S.; writing—original draft preparation, R.S. and T.F.; writing—review and editing, V.K.; visualization, R.S.; supervision, V.K.; project administration, R.S. and V.K.; funding acquisition, V.K. All authors have read and agreed to the published version of the manuscript.

Funding: The research was supported by the Czech Science Foundation (project GA17-15451S) and the Ministry of Industry and Trade of the Czech Republic (project TRIO FV30271). R.S. thanks ThermoFisher Scientific/Czechoslovak microscopy society scholarship for support.

Acknowledgments: We would like to thank to our colleagues Jaroslav Sobota for preparation of test samples and Frantisek Hruby for his help with external voltage supply unit and its connection to the SEM.

Conflicts of Interest: The authors declare no conflict of interest. The funders had no role in the design of the study; in the collection, analyses, or interpretation of data; in the writing of the manuscript, or in the decision to publish the results.

Abbreviations

The following abbreviations are used in this manuscript:

BSE	Backscatter electron
BSEi	Backscatter electron imaging
CBS	Circular backscatter detector
CEF	Captured energy fraction
DRF	Detector response factor
EELS	Electron energy loss spectroscopy
MC	Monte Carlo
qBSEi	Quantitative backscatter electron imaging
qSTEM	Quantitative scanning transmission electron microscopy
SBS	Simulated backscattered electron signal
sccm	Standard cubic centimeters per minute
SEM	Scanning electron microscopy

References

1. Echlin, P. *Handbook of Sample Preparation for Scanning Electron Microscopy and X-ray Microanalysis*; Springer: Boston, MA, USA, 2009; p. 332. [CrossRef]
2. Schatten, H.; Walocha, J.; Litwin, J.; Miodoński, A.; Sepsenwol, S.; Naguro, T.; Nakane, H.; Inaga, S.; Walther, P.; Albrecht, R.; et al. *Scanning Electron Microscopy for the Life Sciences*; Cambridge University Press: Cambridge, UK, 2012; p. 261.
3. Fleck, R.A.; Humbel, B.M. *Biological Field Emission Scanning Electron Microscopy*, 1st ed.; Wiley: Hoboken, NJ, USA, 2018; p. 752.
4. Brodusch, N.; Demers, H.; Gauvin, R. *Field Emission Scanning Electron Microscopy*, 1st ed.; Springe Briefs in Applied Sciences and Technology; Springer: Singapore, 2018; p. 137. [CrossRef]
5. Goldstein, J.; Newbury, D.E.; Michael, J.R.; Ritchie, N.W.M.; Scott, J.H.J. *Scanning Electron Microscopy and X-ray Microanalysis*, 4th ed.; Springer: New York, NY, USA, 2018; p. 550.
6. Assa'd, A.M.D.; Gomati, M.M.E. Backscattering Coefficients for Low Energy Electrons. *Scan. Microsc.* **1998**, *12*, 185–192.
7. Lin, W.R.; Chuang, Y.J.; Lee, C.H.; Tseng, F.G.; Chen, F.R. Fabrication and characterization of a sensitivity multi-annular backscattered electron detector for desktop SEM. *Sensors* **2018**, *18*, 1–13. [CrossRef] [PubMed]
8. Krzyzanek, V.; Sporenberg, N.; Keller, U.; Guddorf, J.; Reichelt, R.; Schönhoff, M. Polyelectrolyte multilayer capsules: Nanostructure and visualisation of nanopores in the wall. *Soft Matter* **2011**, *7*, 7034–7041. [CrossRef]
9. Dapor, M.; Bazzanella, N.; Toniutti, L.; Miotello, A.; Gialanella, S. Backscattered electrons from surface films deposited on bulk targets: A comparison between computational and experimental results. *Nucl. Instrum. Methods Phys. Res. Sect. B Beam Interact. Mater. Atoms.* **2011**, *269*, 1672–1674. [CrossRef]
10. Dapor, M.; Bazzanella, N.; Toniutti, L.; Miotello, A.; Crivellari, M.; Gialanella, S. Backscattered electrons from gold surface films deposited on silicon substrates: A joint experimental and computational investigation to add new potentiality to electron microscopy. *Surf. Interface Anal.* **2013**, *45*, 677–681. [CrossRef]
11. Assa'd, A.M.D. Monte Carlo calculation of the backscattering coefficient of thin films of low on high atomic number materials and the reverse as a function of the incident electron energy and film thickness. *Appl. Phys. A* **2018**, *124*, 699. [CrossRef]
12. Müller, E.; Gerthsen, D. Composition quantification of electron-transparent samples by backscattered electron imaging in scanning electron microscopy. *Ultramicroscopy* **2017**, *173*, 71–75. [CrossRef]
13. Volkenandt, T.; Müller, E.; Hu, D.Z.; Schaadt, D.M.; Gerthsen, D. Quantification of sample thickness and in-concentration of InGaAs quantum wells by transmission measurements in a scanning electron microscope. *Microsc. Microanal.* **2010**, *16*, 604–613. [CrossRef]
14. Kim, H.; Negishi, T.; Kudo, M.; Takei, H.; Yasuda, K. Quantitative backscattered electron imaging of field emission scanning electron microscopy for discrimination of nano-scale elements with nm-order spatial resolution. *J. Electron. Microsc.* **2010**, *59*, 379–385. [CrossRef]

15. Garitagoitia Cid, A.; Rosenkranz, R.; Löffler, M.; Clausner, A.; Standke, Y.; Zschech, E. Quantitative analysis of backscattered electron (BSE) contrast using low voltage scanning electron microscopy (LVSEM) and its application to AlGaN/GaN layers. *Ultramicroscopy* **2018**, *195*, 47–52. [CrossRef]
16. Sánchez, E.; Torres Deluigi, M.; Castellano, G. Mean atomic number quantitative assessment in backscattered electron imaging. *Microsc. Microanal.* **2012**, *18*, 1355–1361. [CrossRef] [PubMed]
17. Reimer, L. *Scanning Electron Microscopy: Physics of Image Formation and Microanalysis*, 2nd ed.; Springer: Berlin/Heidelberg, Germany; New York, NY, USA, 1998; p. 538.
18. Volkenandt, T.; Müller, E.; Gerthsen, D. Sample thickness determination by scanning transmission electron microscopy at low electron energies. *Microsc. Microanal.* **2014**, *20*, 111–123. [CrossRef] [PubMed]
19. Skoupy, R.; Nebesarova, J.; Slouf, M.; Krzyzanek, V. Quantitative STEM imaging of electron beam induced mass loss of epoxy resin sections. *Ultramicroscopy* **2019**, *202*, 44–50. [CrossRef] [PubMed]
20. Pfaff, M.; Müller, E.; Klein, M.F.G.; Colsmann, A.; Lemmer, U.; Krzyzanek, V.; Reichelt, R.; Gerthsen, D. Low-energy electron scattering in carbon-based materials analyzed by scanning transmission electron microscopy and its application to sample thickness determination. *J. Microsc.* **2011**, *243*, 31–39. [CrossRef]
21. Seiter, J.; Müller, E.; Blank, H.; Gehrke, H.; Marko, D.; Gerthsen, D. Backscattered electron SEM imaging of cells and determination of the information depth. *J. Microsc.* **2014**, *254*, 75–83. [CrossRef]
22. Demers, H.; Poirier-Demers, N.; Couture, A.R.; Joly, D.; Guilmain, M.; de Jonge, N.; Drouin, D. Three-dimensional electron microscopy simulation with the CASINO Monte Carlo software. *Scanning* **2011**, *33*, 135–146. [CrossRef]
23. Salvat, F.; Jablonski, A.; Powell, C.J. Elsepa—Dirac partial-wave calculation of elastic scattering of electrons and positrons by atoms, positive ions and molecules. *Comput. Phys. Commun.* **2005**, *165*, 157–190. [CrossRef]
24. Merli, P.; Morandi, V.; Corticelli, F. Backscattered electron imaging and scanning transmission electron microscopy imaging of multi-layers. *Ultramicroscopy* **2003**, *94*, 89–98. [CrossRef]
25. Kowoll, T.; Müller, E.; Fritsch-Decker, S.; Hettler, S.; Störmer, H.; Weiss, C.; Gerthsen, D. Contrast of Backscattered Electron SEM Images of Nanoparticles on Substrates with Complex Structure. *Scanning* **2017**, *2017*, 1–12. [CrossRef]
26. Leosson, K.; Ingason, A.S.; Agnarsson, B.; Kossoy, A.; Olafsson, S.; Gather, M.C. Ultra-thin gold films on transparent polymers. *Nanophotonics* **2013**, *2*, 3–11. [CrossRef]
27. Dapor, M. Backscattering of low energy electrons from carbon films deposited on aluminum: A Monte Carlo simulation. *J. Appl. Phys.* **2004**, *95*, 718–721. [CrossRef]
28. Assa'd, A.M. Monte Carlo computation of the influence of carbon contamination layer on the energy distribution of backscattered electrons emerging from Al and Au. *Jordan J. Phys.* **2019**, *12*, 37–44.

B.4 The application of scanning electron microscopy with energy-dispersive X-Ray Spectroscopy (SEM-EDX) in ancient dental calculus for the reconstruction of human habits

D. Fialova, **R. Skoupy**, E. Drozdova, A. Patak, J. Pinos, L. Sín, R. Benus, and B. Klima. The Application of Scanning Electron Microscopy with Energy-Dispersive X-Ray Spectroscopy (SEM-EDX) in Ancient Dental Calculus for the Reconstruction of Human Habits. *Microscopy and Microanalysis*, 23(6):1207–1213, 2017. doi:10.1017/s143192761701266198

Microsc. Microanal., page 1 of 7
doi:10.1017/S1431927617012661

Microscopy AND Microanalysis

MICROGRAPHIA

The Application of Scanning Electron Microscopy with Energy-Dispersive X-Ray Spectroscopy (SEM-EDX) in Ancient Dental Calculus for the Reconstruction of Human Habits

Dana Fialová,[1,*] Radim Skoupý,[2] Eva Drozdová,[1] Aleš Paták,[2] Jakub Piňos,[2] Lukáš Šín,[3] Radoslav Beňuš,[4] and Bohuslav Klíma[5]

[1]*Department of Experimental Biology, Faculty of Science, Masaryk University, Kamenice 5, 625 00 Brno, Czech Republic*
[2]*Institute of Scientific Instruments of the CAS, Královopolská 147, 612 64 Brno, Czech Republic*
[3]*Archaeological Centre Olomouc, U Hradiska 6, 779 00 Olomouc, Czech Republic*
[4]*Department of Anthropology, Faculty of Natural Sciences, Comenius University, Ilkovičova 6, 842 15 Bratislava 4, Slovak Republic*
[5]*Department of History, Faculty of Education, Masaryk University, Poříčí 9, 603 00 Brno, Czech Republic*

Abstract: The great potential of scanning electron microscopy with energy-dispersive X-ray spectroscopy (SEM-EDX) is in detection of unusual chemical elements included in ancient human dental calculus to verify hypotheses about life and burial habits of historic populations and individuals. Elemental spectra were performed from archeological samples of three chosen individuals from different time periods. The unusual presence of magnesium, aluminum, and silicon in the first sample could confirm the hypothesis of high degree of dental abrasion caused by particles from grinding stones in flour. In the second sample, presence of copper could confirm that bronze jewelery could lie near the buried body. The elemental composition of the third sample with the presence of lead and copper confirms the origin of individual to Napoleonic Wars because the damage to his teeth could be explained by the systematic utilization of the teeth for the opening of paper cartridges (a charge with a dose of gunpowder and a bullet), which were used during the 18th and the 19th century AD. All these results contribute to the reconstruction of life (first and third individual) and burial (second individual) habits of historic populations and individuals.

Key words: ancient dental calculus, SEM-EDX, human habits, the Great Moravian Empire, Napoleonic Wars

Introduction

Ancient human dental calculus is a very important bio-archeological material because it is formed from dental plaque during the life of an individual. Thus, it has been identified as a reservoir of various fragments of cereals, vegetable fibers, phytoliths, pollens, seeds, animal hairs, parasites, insects, microfossils, bacteria, fungi, other biomolecules and elements. Several different types of microscopes were used to examine ancient human dental calculus. Polarizing light microscopes were used for identification of microfossils such as phytoliths or starch grains, which are important in revealing the human diet (Boyadjian et al., 2007; Piperno & Henry, 2008; Hardy et al., 2009, 2012). Transmission electron microscopy (TEM) brought information about bacterial components, crystals (Kakei et al., 2009) and also proof that "reactive" bacterial ancient DNA (aDNA) exists in 4,000–5,000 years old human dental calculus (Preus et al., 2011). Scanning electron microscopy (SEM) gave a lot of information about human diet (Arensburg, 1996; Fox et al., 1996; Hardy et al., 2012; Power et al., 2014), oral bacterial flora (Vandermeersch et al., 1994; Pap et al., 1995; Linossier et al., 1996; Hershkovitz et al., 1997), environmental conditions (Fox et al., 1996), and the habits of historic populations and individuals (Blatt et al., 2011; Hardy et al., 2012).

Energy-dispersive X-ray spectroscopy (EDX) was used in connection with TEM and brought information about the inorganic elemental composition of the calculus of recent ethnic groups. Differences between two ethnic groups were shown mainly in the levels of sodium and magnesium and in relation to smoking (Roberts-Harry et al., 2000). The inorganic and crystallographic composition of recent calculus has been known for many years (Gron et al., 1967; Sundberg & Friskopp, 1985). The main elements in dental calculus are calcium, phosphorus, magnesium, fluoride, carbon dioxide and they mainly come from hydroxyapatite, whitlockite, octacalcium phosphate, and brushite (Gron et al., 1967). Other special elements are supposed to come from other sources dependent on diet, habits, environment, ethnic groups, etc.

SEM-EDX was also used in connection with SEM to focus on microfossils and starch in ancient dental calculus (Dudgeon & Tromp, 2014; Power et al., 2014). Only the

Received February 14, 2017; accepted October 18, 2017
*Corresponding author. danafialka@mail.muni.cz

Table 1. Information About Samples and Proposed Hypotheses.

Archeological Location	Dating of Locality	Sex	Age	Grave Goods	Hypothesis About Habits
Znojmo-Hradiště No. 464, Czech Republic	9th–10th century AD	Male	53–58	Yes	Using of grinding stones
Devín-Za kostolom No. 53, Slovak Republic	9th–10th century AD	Male	30–39	Unknown	Bronze jewelery in grave
Majetín No. 801, Czech Republic	19th century AD Napoleonic war (probably)	Male	30–50	No	Utilization of the teeth by opening paper cartridges

study made by Charlier (Charlier et al., 2010) confirmed different individual elemental compositions of dental calculus in five samples from the Etruscan-Celtic necropolis.

Therefore, EDX was used to verify hypotheses about life and burial habits of chosen individuals in the study presented here.

Materials and Methods

Anthropological Examination and Sampling

Three archeological samples of human dental calculus were taken (Table 1). The first sample came from individual No. 464 from the 9th century AD from the early Mediaeval Period—the Great Moravian Empire from the Znojmo-Hradiště burial site in the Czech Republic (Figs. 1a, 2a). The sample was taken from the buccal side of the lower left second incisor. The size of the sample was 3.5 × 4.5 mm and it had dark brown color outside and light brown color inside. When the SEM was used, there were seen crystals, bacteria (Fig. 1a), and vegetable/plant fibers (Fialová et al., 2017). Sex and age were estimated by anthropological methods (Sjøvold, 1975; Lovejoy et al., 1985; Bruzek, 2002). The individual was a 53–58-year-old man with a high degree of dental abrasion [5–6 on a scale to 8 (Smith, 1984)] (Fig. 2a), which was probably caused by particles from grinding stones in flour.

The second sample from green-colored teeth (Fig. 2b) came from individual No. 53 from the 9th century AD from the early Mediaeval Period—the Great Moravian Empire from the Devín-Za kostolom burial site in the Slovak Republic. The sample was taken from the buccal side of the

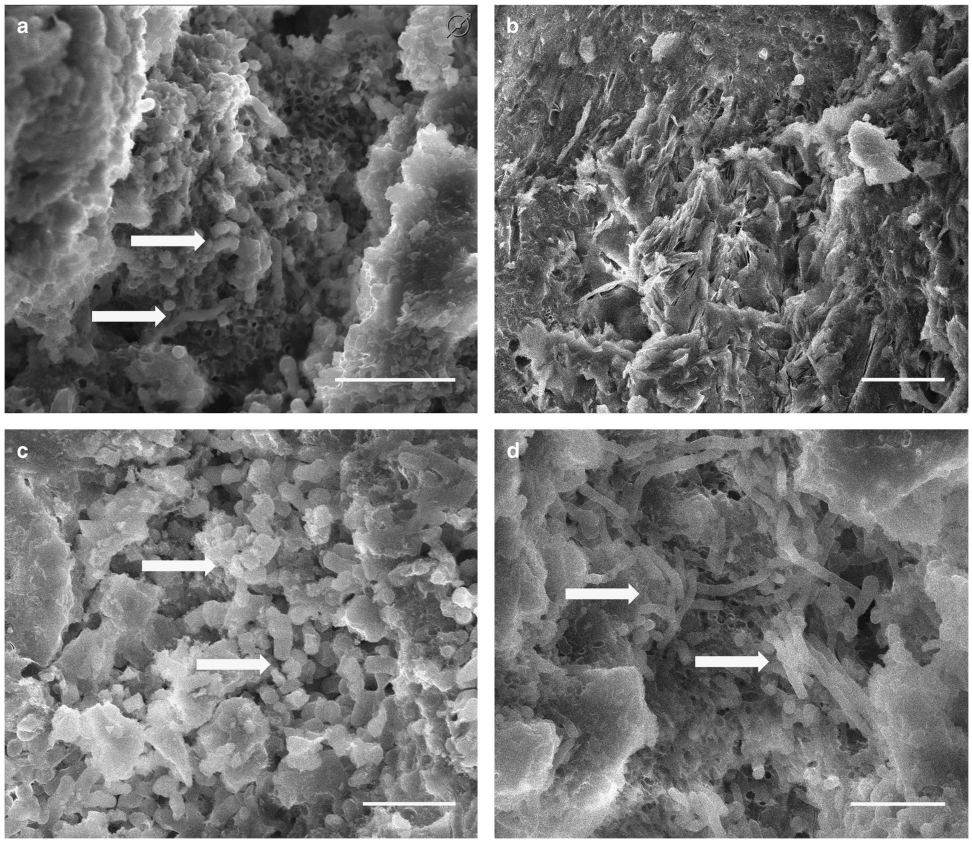

Figure 1. Electron micrographs of ancient human dental calculus where bacteria are visible (some of them marked with arrows), on or between various forms of crystals. Samples come from (**a**) Znojmo-Hradiště, bar = 10 μm; (**b**) Devín-Za kostolom (crystals only), bar = 5 μm; (**c**) Devín-Za kostolom, bar = 3 μm; and (**d**) Majetín, bar = 10 μm.

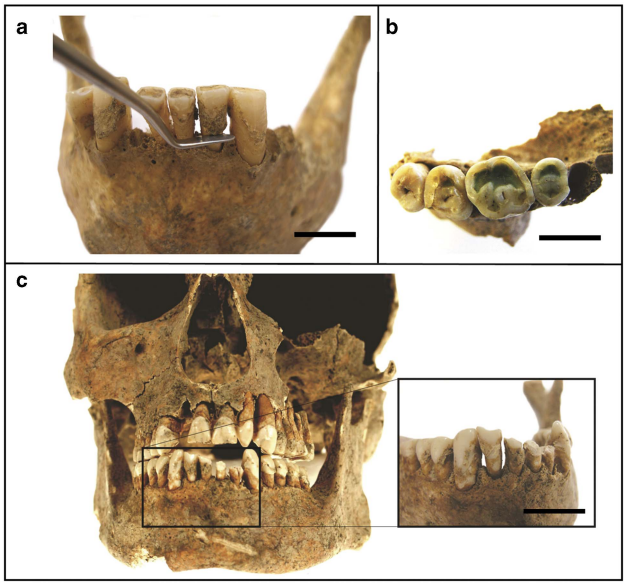

Figure 2. Images of the samples. Bar = 10 mm. **a:** The sampling of the ancient human dental calculus from a grave in Znojmo-Hradiště No. 464 in the Czech Republic. **b:** Green-coloured teeth of the man No. 53 from Devín-Za kostolom in the Slovak Republic. **c:** Man No. 801 from the site Majetín in the Czech Republic. Incisors of his lower jaw showed traces of a trauma with a military origin.

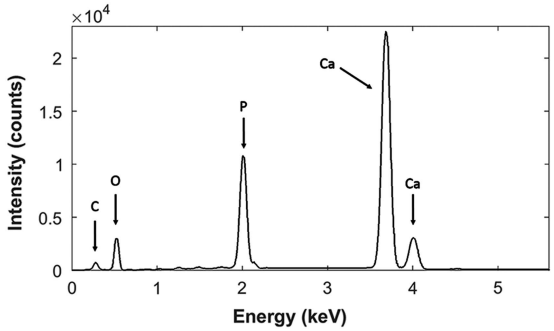

Figure 3. The usual energy-dispersive X-ray spectrum of the ancient human dental calculus.

upper left first molar. The size of the sample was 2.5 × 1.5 mm and it had light green brown color outside and light brown color inside. When the SEM was used, there were seen crystals, bacteria (Figs. 1b, 1c), and vegetable/plant fibers. Sex and age were estimated by anthropological methods (Lovejoy et al., 1985; Bruzek, 2002). The individual was a 30–39-year-old man with no goods in the grave according to archeological records (Harmadyová, 2009).

The third sample came from a 30–50-year-old man (No. 801) from the Majetín site in the Czech Republic. The sample was taken from the buccal side of the lower right first incisor. The size of the sample was 3 × 2 mm and it had dark brown color outside (Fig. 2c) and light brown color inside. When the SEM was used, there were seen crystals and bacteria (Fig. 1d). Sex and age were estimated by anthropological methods (Lovejoy et al., 1985; Bruzek, 2002). All the incisors of his lower jaw showed traces of the trauma of a military origin (Fig. 2c). The municipal chronicle of Majetín describes this area as a burial place of Napoleonic soldiers. No more sensitive dating material (such as parts of military equipment) was discovered there.

Samples of supragingival calculus (above the gum line) were taken manually in a flow box by germfree periodontal instruments (scaler, chisel) (Fig. 2a) into sterile plastic bags.

In total, we performed EDX analysis of almost 20 samples of calculus from several individuals (different historical periods), however, there were no interesting results nor any hypothesis of their habits. Therefore they are not attached in this work. A usual spectrum (from the ancient human dental calculus), however, is shown for comparison in Figure 3.

SEM-EDX

For the SEM-EDX analysis a Magellan 400 SEM (FEI) equipped with an ED APOLLO X Silicon Drift Detector (EDAX) was used. All measurements were taken at an acceleration voltage of 30 kV. The calculus samples were mounted on stubs by using double-sided carbon tape. Only one sample (from Devín-Za kostolom) was investigated both using the coating method and then also without any surface modification, in order to evaluate the pros and cons of coating and to decide which method would be better to use. This sample was at first examined without the use of surface modifications, and a 5 nm chromium layer (Quorum Q150T) was sputter-coated afterwards. However, the elemental spectra were comparable with each other, so we decided to choose the less destructive method, and all samples were generally investigated without the use of surface modifications. At least five measurements were performed on each sample, together with measurements of the inside and the outside of calculus to eliminate burial ground contamination (to determinate for which elements from the burial environment are the calculus permeable). To evaluate our results (by the nondestructive method) we performed EDX mapping on a sample from Majetín, embedded in epoxy resin. A sample of dental calculus was embedded in epoxy block using EpoFix kit (Struers). For the vacuum impregnation (needed due to the porosity of samples), an improvised apparatus was made. After that, the epoxy blocks were carefully ground and polished down to the final stage using 1 μm diamond suspension in Struers Tegramin. The sample was at first analyzed by low-energy electron microscopy (LEEM), then it was sputter coated with a 5 nm chromium layer (Quorum Q150T) for the EDX mapping.

Results and Discussion

The first sample of calculus from the left second lower incisor came from a man with high degree of dental abrasion, which was probably caused by particles of grinding stones in flour. This hypothesis was verified by comparison of the elemental

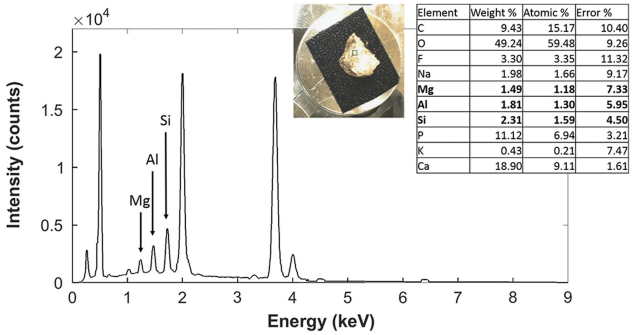

Element	Weight %	Atomic %	Error %
C	9.43	15.17	10.40
O	49.24	59.48	9.26
F	3.30	3.35	11.32
Na	1.98	1.66	9.17
Mg	**1.49**	**1.18**	**7.33**
Al	**1.81**	**1.30**	**5.95**
Si	**2.31**	**1.59**	**4.50**
P	11.12	6.94	3.21
K	0.43	0.21	7.47
Ca	18.90	9.11	1.61

Figure 4. The energy-dispersive X-ray spectrum and the result table of the dental calculus of the man No. 464 from Znojmo-Hradiště with magnesium, aluminum and silicon.

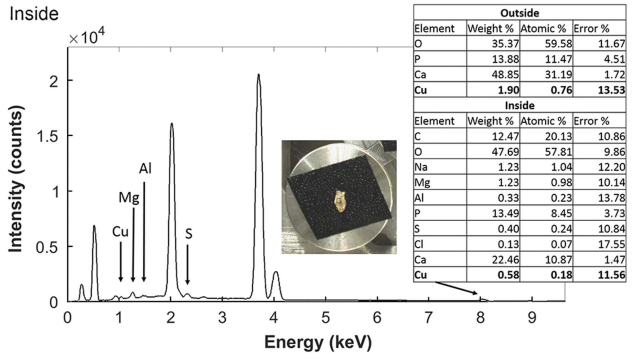

Outside			
Element	Weight %	Atomic %	Error %
O	35.37	59.58	11.67
P	13.88	11.47	4.51
Ca	48.85	31.19	1.72
Cu	**1.90**	**0.76**	**13.53**
Inside			
Element	Weight %	Atomic %	Error %
C	12.47	20.13	10.86
O	47.69	57.81	9.86
Na	1.23	1.04	12.20
Mg	1.23	0.98	10.14
Al	0.33	0.23	13.78
P	13.49	8.45	3.73
S	0.40	0.24	10.84
Cl	0.13	0.07	17.55
Ca	22.46	10.87	1.47
Cu	**0.58**	**0.18**	**11.56**

Figure 5. The energy-dispersive X-ray spectrum from inside and results tables from inside and outside of the dental calculus of the man from Devín-Za kostolom (No. 53).

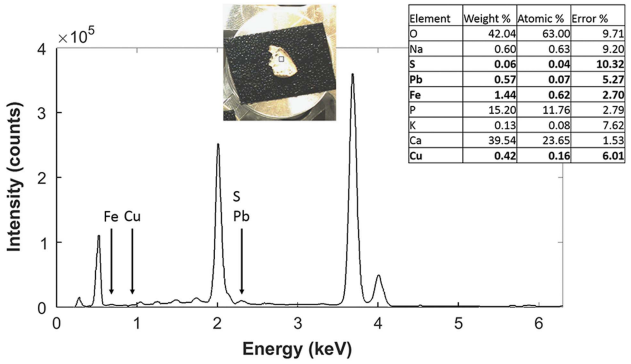

Element	Weight %	Atomic %	Error %
O	42.04	63.00	9.71
Na	0.60	0.63	9.20
S	**0.06**	**0.04**	**10.32**
Pb	**0.57**	**0.07**	**5.27**
Fe	**1.44**	**0.62**	**2.70**
P	15.20	11.76	2.79
K	0.13	0.08	7.62
Ca	39.54	23.65	1.53
Cu	**0.42**	**0.16**	**6.01**

Figure 6. The energy-dispersive X-ray spectrum and the result table of the dental calculus of the soldier No. 801 from Majetín with lead, sulphur, iron, and copper.

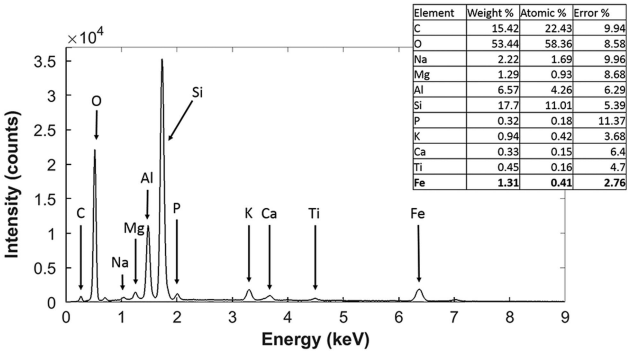

Element	Weight %	Atomic %	Error %
C	15.42	22.43	9.94
O	53.44	58.36	8.58
Na	2.22	1.69	9.96
Mg	1.29	0.93	8.68
Al	6.57	4.26	6.29
Si	17.7	11.01	5.39
P	0.32	0.18	11.37
K	0.94	0.42	3.68
Ca	0.33	0.15	6.4
Ti	0.45	0.16	4.7
Fe	**1.31**	**0.41**	**2.76**

Figure 7. The energy-dispersive X-ray spectrum from the burial ground from Majetín, where lead/sulphur are not present. Iron is a burial contamination.

composition between his dental calculus and grinding stones (found in the same burial site). Unusual elements like magnesium, aluminum, and silicon were found in dental calculus (Fig. 4). These are also the main elements of grinding stones from this population (Šichnárková, 2014). These results contribute to confirming the hypothesis about the high degree of dental abrasion being caused by particles of grinding stones introduced into flour and then consumed by the individual. The fact that magnesium, aluminum, and silicon are not permeable through the calculus from the burial environment (burial ground) is confirmed, because these elements are contained in every soil, yet they are not found in the calculus in any other case we analyzed (silicon, e.g., is not found in any of the two cases below, aluminum and magnesium are not found in the third case).

The second sample came from a man who had no goods in the grave according to archeological records (Harmadyová, 2009). Nevertheless, a green coloring of the three left upper teeth was noticed, so dental calculus was sampled from the left upper first molar (Fig. 2b). The green coloring suggests that some bronze jewelery could lie near the buried body. The elemental spectrum (Fig. 5 inside) shows the presence of copper (the essential element of bronze) and sulfur, which could be addition in this alloy and magnesium and aluminum which could be from a grinding stone like in the first case (which seems to be a more probable hypothesis considering the fact that these elements are not permeable through the dental calculus, as explained above). To determine a permeability of copper from the burial environment through the calculus, we analyzed the outside of the calculus, which was probably in contact with a copper artifact. The elemental spectra between outside and inside had the same shape, however, there was a higher amount of copper outside (Fig. 5 outside). That confirmed that the copper came from the burial environment. These results specify the burial habits of this man.

The third unique sample came from the lower second right incisor from the man from Majetín. All the incisors of his lower jaw showed traces of the trauma of a military origin (Fig. 2c). SEM-EDX analysis was done to confirm the hypothesis that damage to the teeth was caused by the systematic utilization of the teeth for opening paper cartridges (a charge with a dose of gunpowder and a bullet), that were used during the 18th and the 19th century (Šín & Vrána, 2014). Unusual elements in this sample such as lead, sulfur, iron, and copper are shown in Figure 6. These contribute to confirmation of the hypothesis presented. The authors are aware that lead and sulfur are not distinguishable in EDX spectrum at this concentration, but in this case even sulfur or a mixture of these two elements (which is expected)

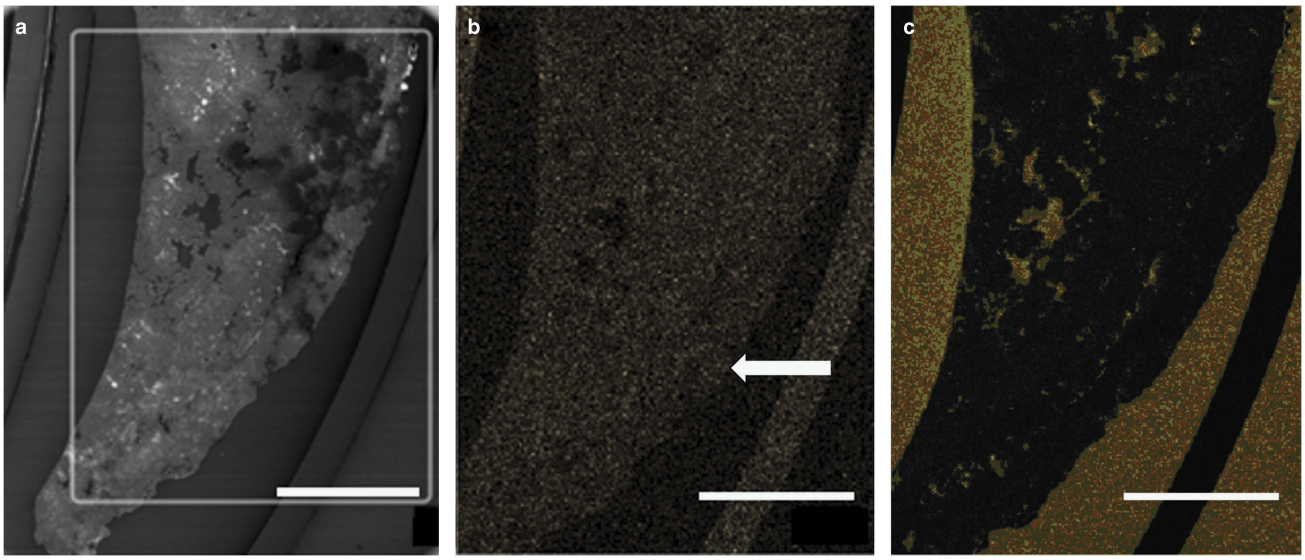

Figure 8. The sample of the dental calculus from Majetín (No. 801). Bar = 500 µm. **a:** SEM image. **b:** EDX lead map from the rectangular highlighted in (**a**). The arrow shows the sample. **c:** EDX carbon map.

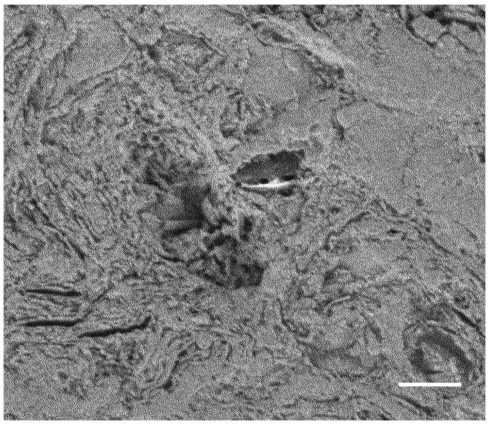

Figure 9. LEEM (landing energy 250 eV) image of dental calculus from Majetín (No. 801). Bar = 500 nm.

contributes to our hypothesis too. The reason is that sulfur is a compound of gunpowder and lead is used in the manufacture of bullets. The EDX spectrum was obtained from the burial ground, and it was confirmed that no lead or sulfur were present in it. Thus, these elements could not come from the burial environment Figure 7. The iron seems to be burial contamination (Figs. 6 and 7).

To evaluate our results, using EDX on a nonmodified dental calculus sample, we performed the EDX mapping on a sample embedded in an epoxy block, thereby the EDX results mentioned above were confirmed (Figs. 8a, 8b). The EDX mapping gave us extra information about sulfur/lead depositing during the calculus formation. Figures 8a and 8b show the equal distribution of sulfur/lead. Thus, the hypothesis arises that the soldier was using his teeth for opening paper cartridges during all the time the dental calculus was formed. The dental calculus could be from 2 weeks to several years old (Mutschelknauss, 2002). It is in agreement with significant traces of the trauma of all the incisors. In areas of lower concentration of lead/sulfur, higher amount of carbon is recognizable (Fig. 8c); these can be places of accumulation of organic material (bacteria, fibers, etc.). Before the coating (for the EDX mapping), the sample was analyzed by LEEM to display a detailed texture (Müllerová & Lenc, 1992) of the calculus (Fig. 9) in high magnification with landing energy 250 eV. Figure 9 suggests that the grain size of dental calculus crystals could be in the range of nanometers, which is similar to vascular calcified plaques (Curtze et al., 2016) where the EDX mapping was done with different techniques, including EBSD analysis. In this article (Curtze et al., 2016), the grain size in bone appears larger than in vascular calcified plaque, as well as fossil coralline skeletons (Cusacks et al., 2008) or fossil eggs (Grellet-Tinner et al., 2011) or shells (Pérez-Huerta & Cusacks, 2009).

Conclusions

Three samples of ancient human dental calculus from chosen individuals were studied in this study in order to verify hypotheses of life and burial habits by using SEM-EDX. Elemental spectra (Fig. 4) of the first sample (from the man dated to the 9th century AD) showed an unusual presence of magnesium, aluminum, and silicon, which contributes to confirmation of the hypothesis of a high degree of dental abrasion caused by particles from grinding stones in flour. Elemental spectra (Fig. 5) of the second sample (from the man from the 9th century AD with no goods according to archeological records but with green coloring of teeth) showed copper in dental calculus. This confirms the hypothesis that bronze jewelery could have lain near the buried body. Elemental spectra (Fig. 6) of the third sample (from the man without any grave goods from Majetín) showed the presence of lead, iron, and copper. This confirms that damage to the teeth was caused by the systematic

utilization of the teeth to open paper cartridges (a charge with a dose of gunpowder and a bullet), which were used during the 18th and the 19th century AD. All these results demonstrate the great potential of SEM-EDX in the study of life (in the case of the first and the third individual) and burial (in the case of the second individual) habits of historic populations or individuals through ancient human dental calculus analysis. It shows the capability of SEM-EDX analysis to support hypotheses about the origin of anomalies which can be founded in ancient bio-archeological material.

Acknowledgments

R.S. acknowledges the support from Ministry of Education, Youth and Sports of the Czech Republic (LO1212) together with the European Commission (ALISI No. CZ.1.05/2.1.00/01.0017). The authors declare no commercial or financial conflicts of interest.

References

Arensburg, B. (1996). Ancient dental calculus and diet. *Hum Evol* **11**, 139–145.

Blatt, S.H., Redmond, B.G., Cassman, V. & Sciulli, P.W. (2011). Dirty teeth and ancient trade: Evidence of cotton fibres in human dental calculus from Late Woodland, Ohio. *Int J Osteoarchaeol* **21**, 669–678.

Boyadjian, C.H.C., Eggers, S. & Reinhard, K. (2007). Dental wash: A problematic method for extracting microfossils from teeth. *J Archaeol Sci* **34**, 1622–1628.

Bruzek, J. (2002). A method for visual determination of sex, using the human hip bone. *Am J Phys Anthropol* **117**, 157–168.

Charlier, P., Huynh-Charlier, I., Munoz, O., Billard, M., Brun, L. & de la Grandmaison, G.L. (2010). The microscopic (optical and SEM) examination of dental calculus deposits (DCD). Potential interest in forensic anthropology of a bio-archaeological method. *Leg Med (Tokyo)* **12**, 163–171.

Curtze, S.C., Kratz, M., Steinert, M. & Vogt, S. (2016). Step down vascular calcification analysis using state-of-the-art nanoanalysis techniques. *Sci Rep* **6**, 23285.

Cusack, M., England, J., Dalbeck, P., Tudhope, A.W., Fallick, A.E. & Allison, N. (2008). Electron backscatter diffraction (EBSD) as a tool for detection of coral diagenesis. *Coral Reefs* **27**, 905–911.

Dudgeon, J.V. & Tromp, M. (2014). Diet, geography and drinking water in Polynesia: Microfossil research from archaeological human dental calculus, Rapa Nui (Easter Island). *Int J Osteoarchaeol* **24**, 634–648.

Fialová, D., Drozdová, E., Skoupý, R., Mikulík, P. & Klíma, B. (2017). Scanning electron microscopy of dental calculus from the Great Moravian necropolis Znojmo-Hradiště. *Anthropologie* **55**, 343–351.

Fox, C.L., Juan, J. & Albert, R.M. (1996). Phytolith analysis on dental calculus, enamel surface, and burial soil: Information about diet and paleoenvironment. *Am J Phys Anthropol* **101**, 101–113.

Gron, P., Van Campen, G.J. & Lindstrom, I. (1967). Human dental calculus. Inorganic chemical and crystallographic composition. *Arch Oral Biol* **12**, 829–837.

Grellet-Tinner, G., Sim, C.M., Kim, D.H., Trimby, P., Higa, A., An, S. L., Oh, H.S., Kim, T.J. & Kardjilov, N. (2011). Description of the first lithostrotian titanosaur embryo in ovo with Neutron characterization and implications for lithostrotian Aptian migration and dispersion. *Gondwana Res* **20**, 621–629.

Hardy, K., Blakeney, T., Copeland, L., Kirkham, J., Wrangham, R. & Collins, M. (2009). Starch granules, dental calculus and new perspectives on ancient diet. *J Archaeol Sci* **36**, 248–255.

Hardy, K., Buckley, S., Collins, M.J., Estalrrich, A., Brothwell, D., Copeland, L., García-Tabernero, A., García-Vargas, S., Rasilla, M., Lalueza-Fox, C., Huguet, R., Bastir, M., Santamaría, D., Madella, M., Wilson, J., Cortés, Á.F. & Rosas, A. (2012). Neanderthal medics? Evidence for food, cooking, and medicinal plants entrapped in dental calculus. *Naturwissenschaften* **99**, 617–626.

Harmadyová, K. (2009). Včasnostredoveká keramika z devínskeho mikroregiónu v 8.-10. storočí. Unpublished dissertation thesis. Comenius University, Bratislava.

Hershkovitz, I., Kelly, J., Latimer, B., Rothschild, B.M., Simpson, S., Polak, J. & Rosenberg, M. (1997). Oral bacteria in miocene Sivapithecus. *J Hum Evol* **33**, 507–512.

Kakei, M., Sakae, T. & Yoshikawa, M. (2009). Electron microscopy of octacalcium phosphate in the dental calculus. *J Electron Microsc (Tokyo)* **58**, 393–398.

Linossier, A., Gajardo, M. & Olavarria, J. (1996). Paleomicrobiological study in dental calculus: Streptococcus mutans. *Scanning Microsc* **10**, 1005–1013. discussion 1014.

Lovejoy, C.O., Meindl, R.S., Pryzbeck, T.R. & Mensforth, R.P. (1985). Chronological metamorphosis of the auricular surface of the ilium: a new method for the determination of adult skeletal age at death. *Am J Phys Anthropol* **68**, 15–28.

Müllerová, I. & Lenc, M. (1992). Some approaches to low-voltage scanning electron microscopy. *Ultramicroscopy* **41**(4), 399–410.

Mutschelknauss, R.E. (2002). *Praktická parodontologie: klinické postupy*. Prague, CZ: Quintessenz.

Pap, I., Tillier, A.-M., Arensburg, B., Weiner, S. & Chech, M. (1995). First scanning electron microscope analysis of dental calculus from European Neanderthals: Subalyuk, (Middle Paleolithic, Hungary). Preliminary report. *Bull Mem Soc Anthropol Paris* **7**, 69–72.

Pérez-Huerta, A. & Cusack, M. (2009). Optimizing electron backscatter diffraction of carbonate biominerals – resin type and carbon coating. *Microsc Microanal* **15**, 197–203.

Piperno, D.R. & Henry, A.G. (2008). Using plant microfossils from dental calculus to recover human diet: a case study from Tell al-Raqā'i, Syria. *J Archaeol Sci* **35**, 1943–1950.

Power, R.C., Salazar-García, D.C., Wittig, R.M. & Henry, A.G. (2014). Assessing use and suitability of scanning electron microscopy in the analysis of micro remains in dental calculus. *J Archaeol Sci* **49**, 160–169.

Preus, H.R., Marvik, O.J., Selvig, K.A. & Bennike, P. (2011). Ancient bacterial DNA (aDNA) in dental calculus from archaeological human remains. *J Archaeol Sci* **38**, 1827–1831.

Roberts-Harry, E.A., Clerehugh, V., Shore, R.C., Kirkham, J. & Robinson, C. (2000). Morphology and elemental composition of subgingival calculus in two ethnic groups. *J Periodontol* **71**, 1401–1411.

Šichnárková, S. (2014). Petrografický výzkum raně středověkých žernovů ze Znojma-Hradiště. 2014th ed. Unpublished Master's thesis. Masaryk University, Brno.

Šín, L. & Vrána, J. (2014). Charakter pohřebního ritu jako odraz událostí 19. století na střední Moravě. *Český lid* **101**, 149–169.

Sjøvold, T. (1975). Tables of the combined method for determination of age at death given by Nemeskéri, Harsányi and Acsádi. *Anthropol Kozl* **19**, 9–22.

Smith, B.H. (1984). Patterns of molar wear in hunter–gatherers and agriculturalists. *Am J Phys Anthropol* **63**, 39–56.

Sundberg, M. & Friskopp, J. (1985). Crystallography of supragingival and subgingival human dental calculus. *Scand J Dent Res* **93**, 30–38.

Vandermeersch, B., Arensburg, B., Tillier, A.M., Rak, Y., Weiner, S., Spiers, M. & Aspillaga, E. (1994). Middle palaeolithic dental bacteria from Kebara, Israel. *C R Acad Sci Serie Ii* **319**, 727–731.

B.5 Size-segregated urban aerosol characterization by electron microscopy and dynamic light scattering and influence of sample preparation

S. Marvanova, P. Kulich, **R. Skoupy**, F. Hubatka, M. Ciganek, J. Bendl, J. Hovorka, and M. Machala. Size-segregated urban aerosol characterization by electron microscopy and dynamic light scattering and influence of sample preparation. *Atmospheric Environment*, 178:181–190, 2018. doi:10.1016/j.atmosenv.2018.02.004

Atmospheric Environment 178 (2018) 181–190

Contents lists available at ScienceDirect

Atmospheric Environment

journal homepage: www.elsevier.com/locate/atmosenv

Size-segregated urban aerosol characterization by electron microscopy and dynamic light scattering and influence of sample preparation

Soňa Marvanová[a], Pavel Kulich[a], Radim Skoupý[b], František Hubatka[c], Miroslav Ciganek[a], Jan Bendl[d], Jan Hovorka[d], Miroslav Machala[a,*]

[a] Veterinary Research Institute, Department of Chemistry and Toxicology, Hudcova 296/70, 62100 Brno, Czech Republic
[b] Institute of Scientific Instruments of the CAS, Královopolská 147, 612 64 Brno, Czech Republic
[c] Veterinary Research Institute, Department of Pharmacology and Immunotherapy, Hudcova 296/70, 62100 Brno, Czech Republic
[d] Institute for Environmental Studies, Faculty of Science, Charles University, Benátská 2, 12801 Prague 2, Czech Republic

ARTICLE INFO

Keywords:
Particulate matter
Size-segregated
Electron microscopy
Energy dispersive X-ray spectroscopy
Dynamic light scattering
Agglomeration

ABSTRACT

Size-segregated particulate matter (PM) is frequently used in chemical and toxicological studies. Nevertheless, toxicological *in vitro* studies working with the whole particles often lack a proper evaluation of PM real size distribution and characterization of agglomeration under the experimental conditions. In this study, changes in particle size distributions during the PM sample manipulation and also semiquantitative elemental composition of single particles were evaluated. Coarse (1–10 μm), upper accumulation (0.5–1 μm), lower accumulation (0.17–0.5 μm), and ultrafine (< 0.17 μm) PM fractions were collected by high volume cascade impactor in Prague city center. Particles were examined using electron microscopy and their elemental composition was determined by energy dispersive X-ray spectroscopy. Larger or smaller particles, not corresponding to the impaction cut points, were found in all fractions, as they occur in agglomerates and are impacted according to their aerodynamic diameter. Elemental composition of particles in size-segregated fractions varied significantly. Ns-soot occurred in all size fractions. Metallic nanospheres were found in accumulation fractions, but not in ultrafine fraction where ns-soot, carbonaceous particles, and inorganic salts were identified. Dynamic light scattering was used to measure particle size distribution in water and in cell culture media. PM suspension of lower accumulation fraction in water agglomerated after freezing/thawing the sample, and the agglomerates were disrupted by subsequent sonication. Ultrafine fraction did not agglomerate after freezing/thawing the sample. Both lower accumulation and ultrafine fractions were stable in cell culture media with fetal bovine serum, while high agglomeration occurred in media without fetal bovine serum as measured during 24 h.

1. Introduction

Particulate matter (PM) is a ubiquitous pollutant in the ambient air that is known to contribute to cardiovascular and respiratory diseases (WHO, 2004). Recently, PM in outdoor air pollution was also classified as carcinogenic to humans, Group 1 (IARC, 2015). Coarse particles such as rock-forming minerals and other dust particles contribute especially to respiratory diseases, while the combustion-derived fine ($PM_{2.5}$) and ultrafine particles have a higher toxic potential, leading to increased mortality and to cardiovascular and respiratory diseases (WHO, 2004). Moreover, ultrafine particles contain among others various organic compounds, e.g. polycyclic aromatic hydrocarbons (Boström et al., 2002; Jalava et al., 2015; Topinka et al., 2015) and trace metal oxides of Fe, Zn, Ti, Cr, As, Cu, V, Mn, Ni being the most abundant (Cass et al., 2000; Pennanen et al., 2007), and are supposed to cause cancer (Donaldson et al., 2005), especially diesel exhaust particles (IARC, 2014). Toxic effects and mode of action of the PM particles of aerodynamic diameter d_{ae} < 10 μm (PM_{10}) or < 2.5 μm ($PM_{2.5}$) have been studied *in vitro* using their organic or water extracts (Gutierrez-Castillo et al., 2006; Hornberg et al., 1998; Libalova et al., 2014a, 2014b) or isolated whole particles (Billet et al., 2007, 2008; Gualtieri et al., 2012; Gualtieri et al., 2009; Lepers et al., 2014; Longhin et al., 2013; Upadhyay et al., 2003). The particles of d_{ae} < 100 nm (ultrafine particles or nanoparticles) appear to be of great importance due to their high specific surface area and high number concentration (Hughes et al., 1998). Ultrafine particles also easily enter and transfer within organisms, and they interact with cells and subcellular components (Oberdorster et al., 2005). As the significance of ultrafine PM is being

* Corresponding author.
E-mail addresses: marvanova@vri.cz (S. Marvanová), kulich@vri.cz (P. Kulich), ras@isibrno.cz (R. Skoupý), hubatka@vri.cz (F. Hubatka), ciganek@vri.cz (M. Ciganek), Jan.Bendl@natur.cuni.cz (J. Bendl), jan.hovorka@natur.cuni.cz (J. Hovorka), machala@vri.cz (M. Machala).

https://doi.org/10.1016/j.atmosenv.2018.02.004
Received 26 July 2017; Received in revised form 8 December 2017; Accepted 1 February 2018
Available online 02 February 2018

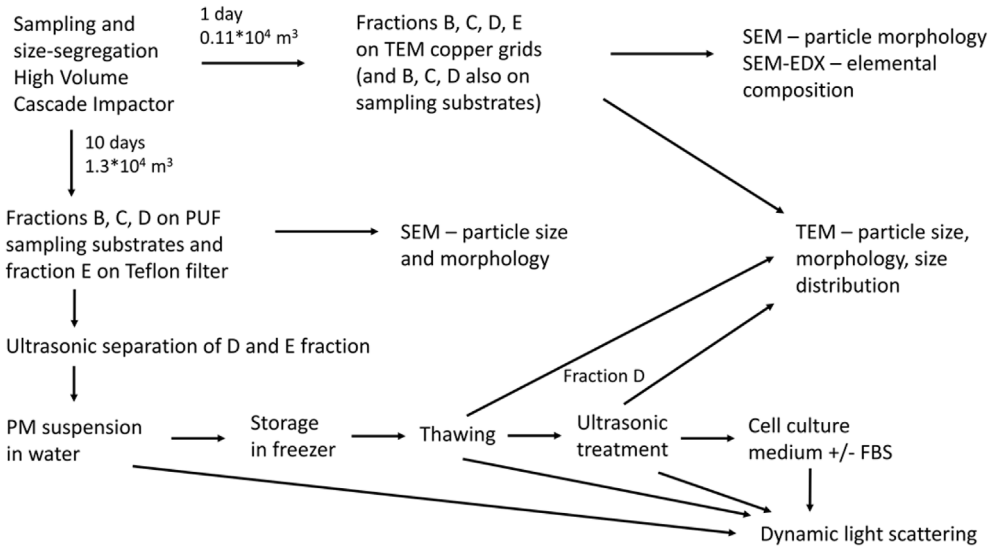

Fig. 1. The experimental design scheme.

increasingly recognized, size-segregated PM fractions are employed in a number of studies using cell cultures or isolated cells, to which they are applied either as organic extracts of size-segregated PM fractions (Topinka et al., 2013, 2015) or as directly size-segregated PM fractions (Becker et al., 2003; Jalava et al., 2006, 2015; Loxham et al., 2013; Ramgolam et al., 2009; Reibman et al., 2002; Thomson et al., 2015).

Nevertheless, the procedures of the aerosol sample collection and preparation are highly variable. The main differences are in the composition of the liquid into which the particles are detached, storage and homogenization of PM suspensions prior to the cell culture exposure, including presence or absence of fetal bovine serum (FBS) in cell culture media. In some studies, $PM_{2.5}$ were collected on impacting plates without any filters and prior to use, the PM sample was resuspended in cell culture media (Andre et al., 2011; Billet et al., 2007, 2008; Lepers et al., 2014). Gualtieri and Longhin et al. (Gualtieri et al., 2009, 2012; Longhin et al., 2013) sampled $PM_{2.5}$ on Teflon filters using low volume gravimetric samplers and detached the particles from the filter by sonication into deionized water. Size-segregated PM fractions, sampled by various cascade impactors, were also detached by sonication from the impaction substrates or filters directly into the cell culture media (Ramgolam et al., 2009; Reibman et al., 2002) or into methanol, followed by additional steps of homogenization (Jalava et al., 2006, 2015; Thomson et al., 2015). Changes in the agglomeration/coagulation of the particles in suspension, caused by various conditions during the PM sample handling, are often not described in sufficient detail in many studies. In recent years, a need to define the nanomaterial together with its environment in toxicological experiments has been emphasized. This should include not only information on particle size and distribution, chemical composition, morphology, surface chemistry and area, but also carefully reported description of nanomaterial agglomeration/aggregation under the experimental conditions, which is influenced especially by the presence of serum in the cell culture media (Krug and Wick, 2011; Nature Nanotechnology Editorial, 2012).

Therefore, we aimed in the present study to characterize changes of the size-segregated PM occurring during sampling, preparation and in cell culture medium. The size-segregated PM was sampled by a high volume cascade impactor, allowing large quantities of particles to be sampled for toxicological and particle characterization studies (Demokritou et al., 2002). Prior to characterization of size-segregated aerosol PM fractions in each step of sample handling, we examined the size, morphology, and elemental composition of aerosol particles on individual impaction substrates, backup filter, and copper grids used for electron microscopy. Scanning and transmission electron microscopy (SEM and TEM) was employed as a tool for direct imaging of individual aerosol particles (Buseck et al., 2014; Deshmukh et al., 2010). High resolution SEM coupled with energy dispersive X-ray spectroscopy was used for determination of individual particle elemental composition (Chen et al., 2006). Then, number size distributions of particles of $0.17 < d_{ae} < 0.5\,\mu m$ and $d_{ae} < 170\,nm$ and their agglomerates/aggregates after the ultrasonic extraction in water were evaluated by electron microscopy and dynamic light scattering. Finally, the influence of freezing/thawing and sonication on the agglomeration/disintegration of the PM water suspension was evaluated, as well as the stability of the PM sample in cell culture medium unsupplemented or supplemented with fetal bovine serum (FBS).

2. Materials and methods

2.1. Aerosol collection

Ambient aerosol particles were collected in Prague city center (GPS: 50.072068 N, 14.423721 E) by high-volume cascade impactor (BGI-900, USA) at a flow-rate of $900\,l\,min^{-1}$. The sampling site is situated in the Charles University botanical garden near a school yard with a small parking lot used by the university staff. The impactor was at a height of 4 m. Coarse ($1 < d_{ae} < 10\,\mu m$, denoted B), upper accumulation ($0.5 < d_{ae} < 1\,\mu m$, denoted C), lower accumulation ($0.17 < d_{ae} < 0.5\,\mu m$, denoted D) aerosol particles were collected on polyurethane foam (PUF) impaction substrates and ultrafine fraction ($d_{ae} < 0.17\,\mu m$, denoted E) on PTFE-coated Glass Micro-Fiber Absolute filters (Pallflex Emfab TX40HI20WW). Before exposure, the PUF substrates were thoroughly cleaned (BGI 900 High Volume Cascade Impactor Guidance Manual, 2008) by consecutive hourly leaching for each solvent (ultrapure water, hexane, methanol, and dichlormethane, p.a. grade) in an ultrasonic bath. After the sonication, the substrates were dried in a clean air hood for 48 h. Then, the substrates and the ultrafilters were equilibrated for 24 h in a desiccator (~50% humidity, saturated $Mg(NO_3)_2{*}6H_2O$, T = 21 °C), weighed (MC210S semi-micro balance, Sartorius) in an air conditioned weighing room, wrapped in aluminum foil, placed in double sealed plastic bags with a zipper and stored in a sealed container at laboratory temperature. Immediately after the sampling, the exposed substrates underwent the same weighing procedure and stored at −20 °C till next use.

Sampling occurred from 27th February to 9th March 2015 for 10 days (about 13 000 m^3 of air) resulting in aerosol mass of 101, 73, 37, and 27 mg for B, C, D and E fractions respectively (Fig. 1). For electron

microscopy, five pieces of formvar coated TEM copper grids (300 mesh grid, Agar Scientific, Austria) stabilized with evaporated carbon film were placed on the surface of the PUF substrates on each stage of the high volume cascade impactor while the last stage was modified by replacing ultrafilter with PUF substrate. In this case, one day sampling went from the 9th to 10th March 2015 (1070 m^3 of air). The grids were kept in a storage box at room temperature in a desiccator.

2.2. Scanning and transmission electron microscopy

Aerosol particle size and morphology were determined by scanning electron microscopy (SEM). Pieces of PUF substrate or Teflon coated filter were mounted on cylindrical Hitachi aluminium sample stubs using carbon conductive tabs (Pelco, Ted Pella, USA) and coated with Pt/Pd or Cr layers using Cressington sputter coater 208HR (Cressington Scientific Instruments, UK). Particles were observed with scanning electron microscope SU8010 (Hitachi, Japan) at magnifications up to 80 000×, at acceleration voltage 12–16 kV. The largest dimension of particles was measured.

Energy dispersive X-ray spectra (EDX) of particles captured on microscopic copper grids coated with formvar film (Sigma-Aldrich, Germany) were measured by detector APOLLO X (EDAX, USA) installed at a high resolution scanning electron microscope Magellan 400 L (FEI, Czech Republic). The acceleration voltage 30 kV and probe current from 0.2 to 3.2 nA in field free mode were used. Particles were imaged in both conventional SEM and STEM (scanning transmission electron microscopy) modes.

Transmission electron microscope (TEM) EM Philips 208 S Morgagni (FEI, Czech Republic) at a voltage of 80 kV was used to examine the size and appearance of particle fractions sampled directly on dry TEM copper grids and of particle suspensions in water dropped on the TEM grids.

2.3. Particle separation

Particles of fraction D and E were separated from PUF substrates or Teflon filter using slightly modified procedure according to Gualtieri et al. (2009). PUF substrates or Teflon filter were placed into glass beaker with deionized MilliQ water and sonicated in ultrasonic bath (Teson 10, 650 W, Tesla, Czech Republic). The PUF substrates were sonicated three times for 20 min, while the E fraction Teflon filter three times for 30 min. Each time the particle suspension was collected and pure MilliQ water was added to the substrate or filter. Mass of extracted particles was determined gravimetrically from the difference of mass of PUF substrate or filter before and after sonication into the water; particle concentrations were 980 or 410 μg/ml for fraction D or E respectively. Particle suspension was aliquated and stored in glass vials at −20 °C until use.

Prior to TEM analysis, frozen aliquot of airborne particle suspension of fraction D was thawed, vortexed and again sonicated for 20 min in an ultrasonic bath. A drop of particle suspension in water was then placed on a TEM grid, blotted from the edge of the grid, and directly viewed by the TEM. The largest dimension of individual particles or agglomerates was measured for 250–700 particles per sample. Size distributions of fraction D treated and not treated by sonication were compared.

2.4. Dynamic light scattering

To determine changes in size distribution for suspensions of D and E fractions under various conditions, Dynamic Light Scattering (DLS) was used (ZetaSizer Nano ZS, Malvern, UK, wavelength of 633 nm). Aliquotes of these particle suspensions were examined just after the ultrasonic extraction from PUF substrates and Teflon filter to water. Next examinations were carried out on samples stored at −20 °C, thawed and mixed thoroughly, and on samples again sonicated for 20 min. The measurements were carried out at 37 °C. Results are presented in the form of number-weighted size distributions, intensity based harmonic mean (Z-average), and polydispersity index (PdI).

To evaluate the stability of PM fractions in cell culture medium D-MEM without phenol red (Dulbecco's Modified Eagle's medium, D2902, Sigma-Aldrich, USA) supplemented with fetal bovine serum (HyClone, GE Healthcare, USA) at concentration 0%, 1%, and 5%, samples were incubated in a Cool-Hotter Dry Bath incubator (Major Science, USA) at 37 °C for 24 h. The DLS measurements were conducted after 1, 2, 3, 4, 6, and 24 h of incubation.

3. Results

SEM, TEM and DLS were used to examine size fractions of particles sampled on TEM grids, PUF substrates, and Teflon filter, and their suspensions in deionized water and cell culture medium. The experimental design is shown in Fig. 1.

3.1. Elemental composition and morphology of particles in size-segregated fractions sampled for 1 day

Ambient air was sampled for one day in order to allow observation of particle morphology directly on TEM grids (Fig. 2) and PUF substrates (Fig. S1). Particles captured on TEM grids were analysed for elemental composition by EDX detector using SEM and STEM mode. The data from EDX analysis of all fractions are presented in Table 1 and supplementary figures (Fig. S2-S6).

Clusters or chains of carbon nanospheres, denoted here as nanosphere-soot (ns-soot) (Buseck et al., 2014), trapped on TEM grids were observed in all fractions (Fig. 2). Other types of carbonaceous particles, differing from ns-soot by their morphology, size, and origin, such as tar balls and organic particles with or without inorganic inclusions (Hand et al., 2005; Pósfai et al., 2003, 2004), are collectively termed carbonaceous particles.

In fraction B (Fig. S2) some clusters of ns-soot reached several micrometers in size. Similar large clusters of ns-soot occurred also in fraction C. Fraction B was predominantly composed of rock-forming minerals among which Ca-amphibole, clinopyroxene, quartz, calcite, and biotite were determined. Perfectly spherical particles of 2 μm and 630 nm in diameter were identified as aluminosilicates containing K, Ca, Fe, most probably originating from high temperature industrial combustion process. Moreover, metallic particles of irregular shape containing Fe with diameter 200 nm were also found.

In fraction C (Fig. S3), carbonaceous particles occurred in form of ns-soot and in the form of larger (< 100 nm) individual spheres with trace amounts of N. On the surface of some carbon nanospheres forming ns-soot, individual particles of 10–25 nm in diameter were found (Fig. 2d). Furthermore, inorganic particles such as crystalline calcium sulphates and sporadically polysulphides, K-aluminosilicates, and high-temperature spherical aluminosilicates were also found. In addition, spherical or irregular particles of diameter > 300 nm containing aluminium were observed. Finally, agglomerates of spherical metallic nanoparticles of diameter 5 nm - 80 nm with Fe as a dominating element and Mn, S, and Si in minor amounts were identified rather frequently.

Fraction D (Fig. S4) contained ns-soot, carbonaceous particles with trace amounts of N and S, particles sensitive to electron beam containing K, Na, S (presumably sulphates), which had in several cases crystalline structure. Additionally, metallic nanospheres of diameter 5 nm - 120 nm with Fe as a dominating element and Mn, Si, S in minor amounts were identified (Fig. 3, Fig. S5).

Ultrafine fraction E (Fig. S6) contained ns-soot, carbonaceous particles, and individually occurring inorganic particles, which were sensitive to electron beam. The inorganic particles in thin layer of irregular shape with fuzzy contour were predominantly composed of Ca or K and S, while possible occurrence of C and O could not be exactly determined, as these elements occurred as background on formvar

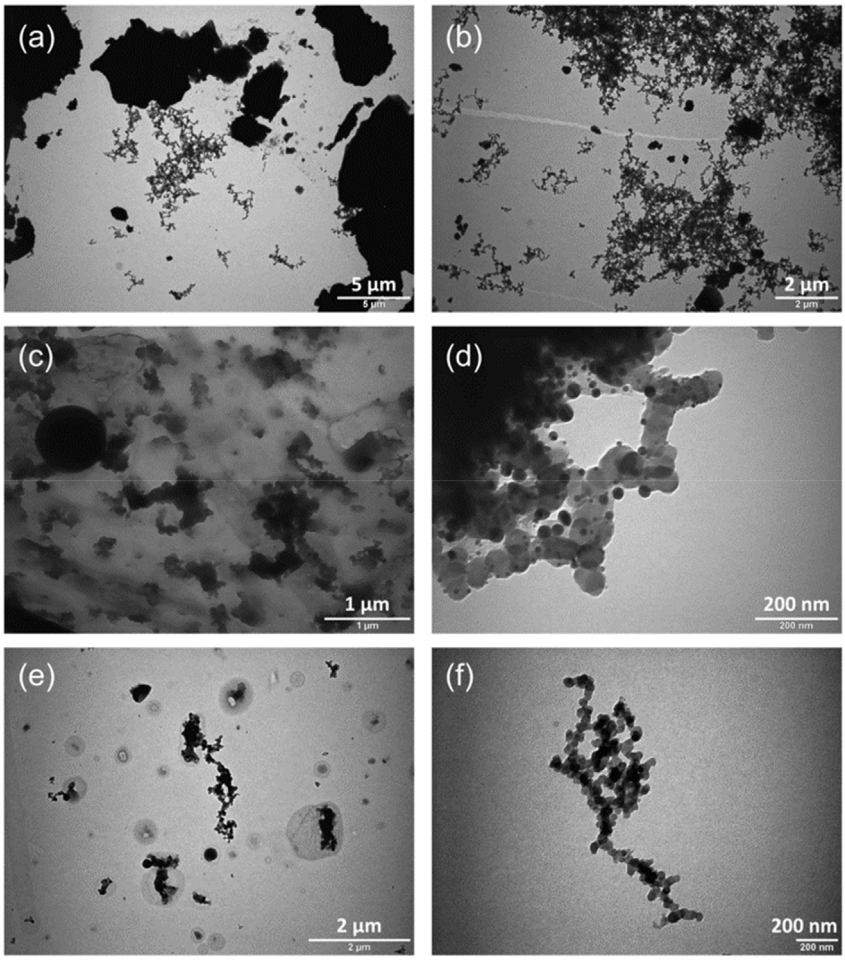

Fig. 2. TEM micrographs of particles collected directly on TEM copper grids. Grids were placed on each stage of the high-volume cascade impactor, following one day sampling. (a) Fraction B, large particles, mostly of mineral origin, together with ns-soot; (b) fraction B, mostly large clusters of ns-soot, but also single ns-soot chains; (c) fraction C, sphere with diameter almost 1 µm, agglomerates/aggregates including ns-soot; (d) fraction C, small nanoparticles, probably metallic, attached to carbon nanospheres of ns-soot, taken at high magnification; (e) fraction D, ns-soot and carbonaceous particles; (f) fraction E, ns-soot.

membrane. We expect that these might be inorganic salts as Ca and K sulphates, or eventually carbonates. Interestingly, no metallic particles were found in fraction E, although the presence of metals cannot be excluded in the ultrafine fraction.

Morphology of size-segregated fractions is presented in Fig. 4. Size distribution of individual particles was determined using SEM in fractions impacted for 10 days. The PUF substrates of fraction B, C, and D, contained significant number of particles smaller than their corresponding cut points (Fig. 5). In contrast, certain number of particles larger than the respective cut points was found on substrates of fractions B, C, and D (Fig. 5). Concerning the particle morphology, fraction B contained particles of various irregular shapes, but also spherical ones, some of them concave. Elongated particles occurred rarely. Fraction C consisted of mostly spherical particles, but irregular particles occurred as well. Fraction D was morphologically similar to fraction C (Fig. 4 and Fig. S1). Teflon filter with fraction E contained ns-soot, but also significant number of larger particles and amorphous agglomerates, so that almost half of the particles on the filter had larger dimension than the corresponding cut point (40 ± 11% of particles with dimension between 170 and 500 nm), (Fig. 5). The larger particles are probably formed by coalescence and agglomeration of smaller particles during the prolonged sampling. This process was pronounced on substrates and filter sampled for 10 days (Fig. 4); nevertheless, it occurred already on substrates sampled for one day. Moreover, some larger particles might represent inorganic salts, similarly to the study of Pósfai et al. (2003), who found several micrometer-sized sea-salt particles together with submicrometer carbonaceous particles on the grids on stage with d_{ae} < 300 nm. These particles, if water soluble, are lost after

Table 1
Types of particles identified by EDX analysis in PM size fractions sampled directly on TEM copper grids for one day.

Fraction	Particles identified by EDX analysis
B (1–10 µm)	Minerals (Ca-amphibole, clinopyroxene, quartz, calcite, biotite); high-temperature aluminosilicate spheres; ns-soot; metallic particles.
C (0.5–1 µm)	Carbonaceous particles; ns-soot; inorganic particles (calcium sulphates/polysulphides, potassium aluminosilicate; high-temperature aluminosilicate spheres); metallic nanospheres (iron-rich).
D (0.17–0.5 µm)	Ns-soot; carbonaceous particles; inorganic particles (potassium/sodium sulphates); metallic nanospheres (iron-rich).
E (< 0.17 µm)	Ns-soot; carbonaceous particles; inorganic particles (calcium/potassium sulphates).

Size distribution of individual particles determined in 10-day fractions.

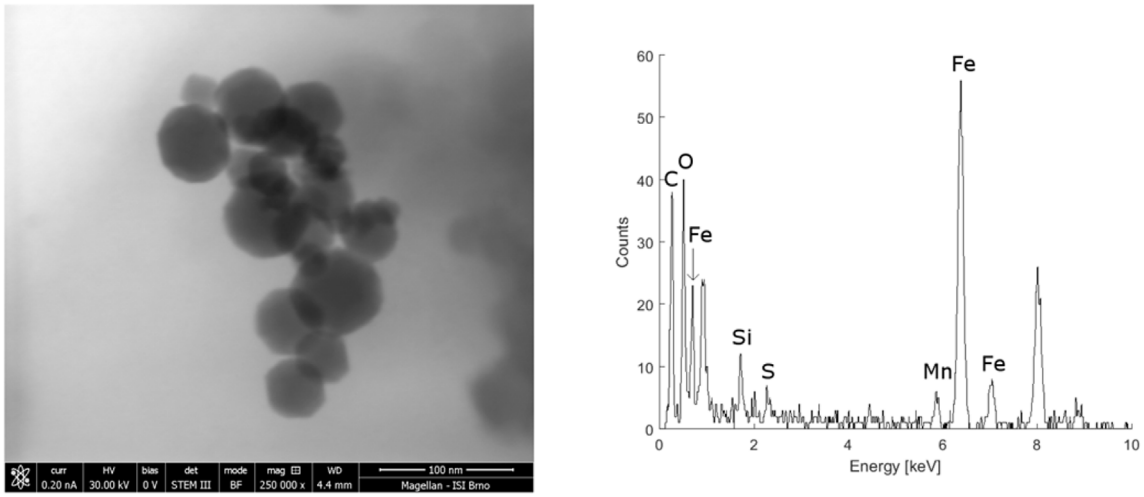

Fig. 3. STEM micrograph of iron-rich nanoparticle agglomerate and its EDX spectrum. The iron-rich agglomerate (a) was identified in fraction D on copper grid sampled for one day. Diameters of individual particles ranged from 15 nm to 65 nm. The EDX spectrum of the agglomerate (b) displays, in addition to iron, also trace amounts of Si, S and Mn. Cu originates from the background, C and O partly originate from the formvar membrane on the grid.

the ultrasonic detachment into water.

3.2. Characterization of particle suspension in water after ultrasonic extraction, storage and ultrasonic homogenization

The extraction of particles directly into the water by sonication was very efficient for PUF substrates. Nevertheless, the efficiency of this procedure was very low for fraction E sampled on Teflon filter, where the majority of particles remained attached to the filter after ultrasonic treatment as verified by SEM (data not shown). Since we intended to use especially the lower accumulation and ultrafine fraction for future cell culture experiments, we focused our attention on fractions D and E. Particle size distribution of water suspension was evaluated using TEM for fraction D, but not E, since there was too low concentration of particles in water suspension. Individually occurring particles or agglomerates/aggregates were divided according their size into categories corresponding to size range of each fraction (Fig. 6). After ultrasonic treatment the percentage of particles in size range 170–500 nm remained almost the same, while the number of particles larger than 500 nm was significantly reduced and number of particles smaller than 170 nm in diameter was significantly elevated. This suggests that treatment in ultrasonic bath caused disagglomeration to smaller agglomerates or individual particles.

Size distributions of particles suspended in water were determined using Dynamic Light Scattering. Z-average and polydispersity index (PdI) were used as parameters comparing the characteristics of distributions. Z-Average is a hydrodynamic parameter used to reflect an overall mean size. Polydispersity index is a dimensionless parameter used as a measure of size distribution width and represents degree of homogeneity (Dynamic Light Scattering, Common terms defined, Malvern Instruments Limited, 2011).

The number-weighed size distributions of particle fractions D and E

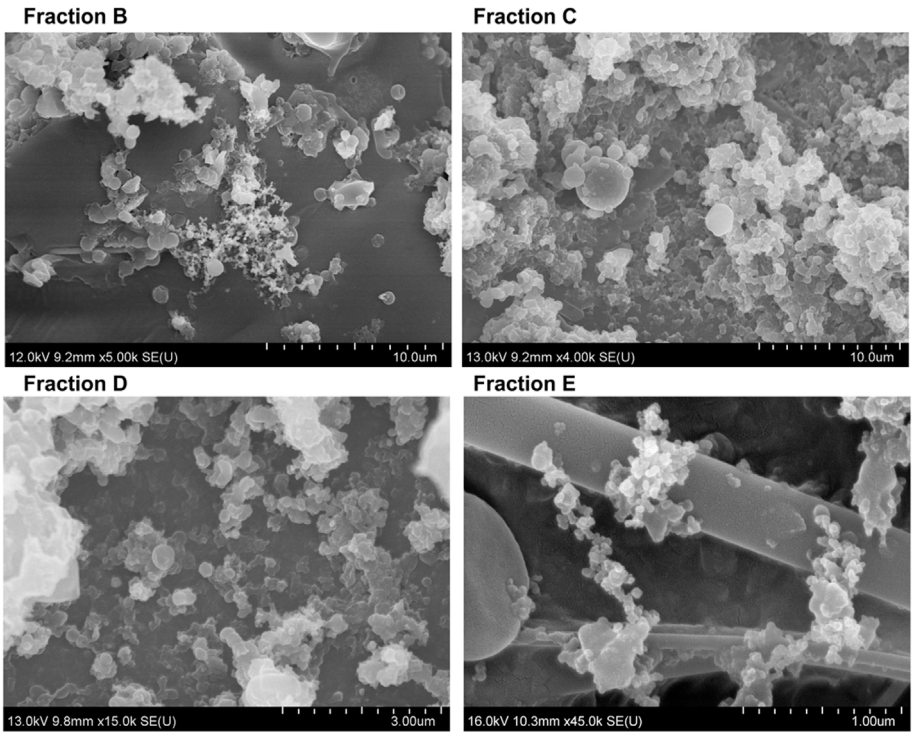

Fig. 4. Representative SEM micrographs showing morphology of airborne particle fractions. Fractions B, C, D (on PUF substrate) and E (on Teflon filter) were sampled for 10 days. Ns-soot can be seen on the image of fraction B and E. On the image of fraction E, teflon filter fibres can also be observed. The respective magnifications were 5000× (B), 4000× (C), 15000× (D), and 45000× (E).

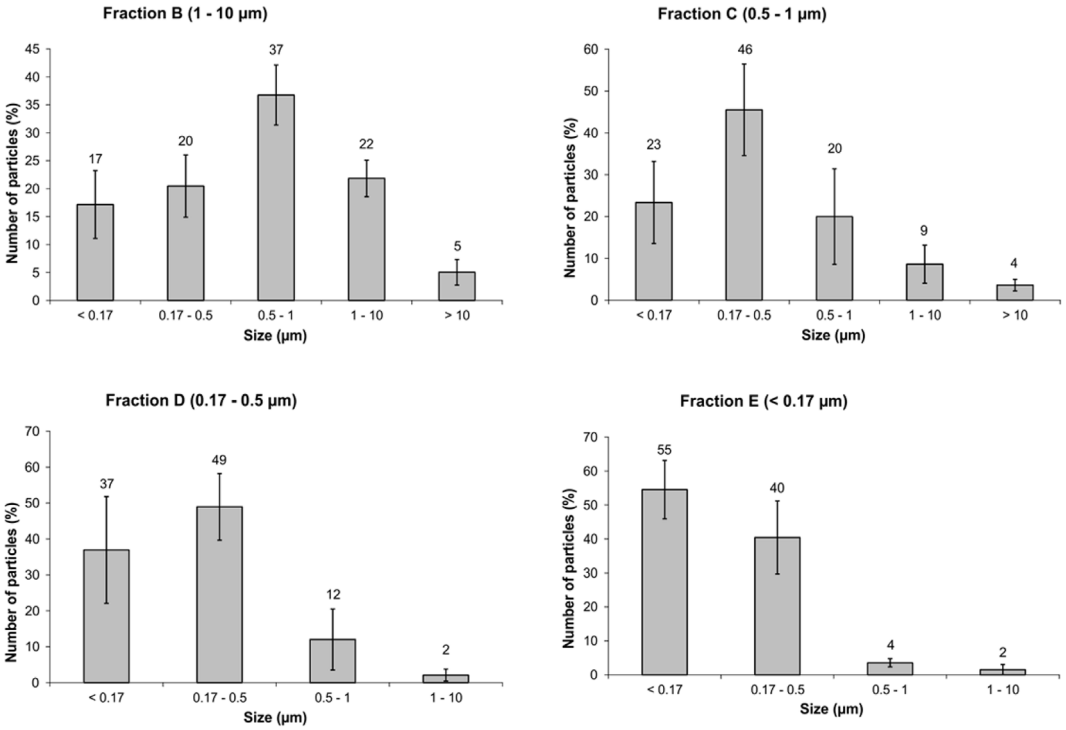

Fig. 5. Particle size distribution of each fraction sampled for 10 days. Size of individual particles on PUF substrate and Teflon filter was determined using SEM as the longest dimension. Three replicates of PUF substrates or filter were evaluated. Error bars represent standard deviations calculated from triplicates in each size category.

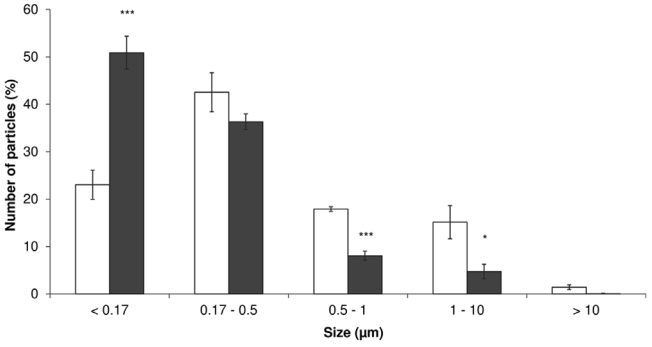

Fig. 6. The effect of sonication on particle number size distribution of fraction D (0.17–0.5 µm). PM water suspension was not treated by sonication (white columns) and treated by sonication (dark columns) after the storage in freezer and thawing. Particle sizes were determined using TEM as the longest dimension of individual particles or agglomerates/aggregates. The data represent average of three independent experiments, with 250–700 particles being measured in each individual experiment. Significant differences between the respective sonicated and non sonicated suspensions were determined by Student's *t*-test (*$p < 0.05$ and ***$p < 0.001$).

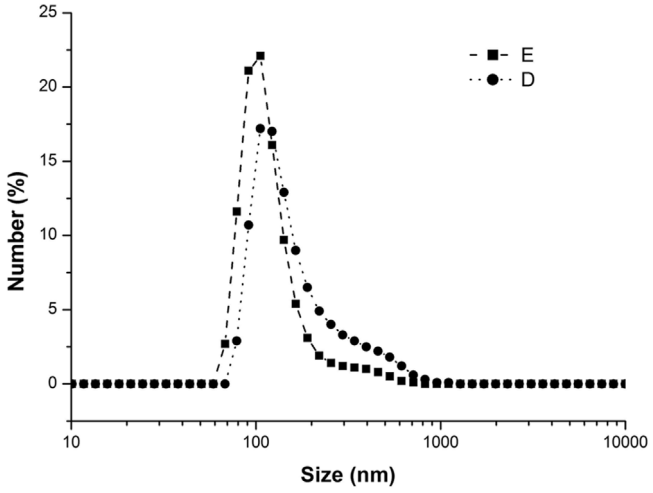

Fig. 7. The number-weighed size distributions of particle fractions D and E suspended in water as determined by DLS. The distributions were measured right after ultrasonic detachment of PM from PUF substrate and Teflon filter.

suspended in water as determined by the DLS right after ultrasonic extraction from PUF substrate and Teflon filter indicated that homogeneity of both fractions after extraction was rather similar. The only significant difference was in the concentration (weigh of particles/ml), as the extraction efficiency of the Teflon filter was low (Fig. 7 and Table 2).

Further, the effect of the storage in freezer and ultrasound homogenization after thawing was studied. By comparing corresponding parameters in Table 2 it can be concluded that while homogeneity of the fraction D after freezing and thawing decreased significantly, there were no major changes for E fraction. Differential behaviour could be caused by either different concentration of the samples, or by their composition, or by the combination of both factors.

After the sonication, significant improvement in the homogeneity of both the samples was observed. However, this step is not beneficial for

Table 2
Z-average (Z-avg) and Polydispersity Index (PdI) values determined using DLS in particle suspension of fraction D and E in water. The samples were measured right after the ultrasonic extraction into the water (no treatment), after storage at −20 °C, thawing and vortexing (frozen-thawed), and after the same treatment followed by 20 min ultrasonication (frozen-thawed and ultrasonicated).

Sample Type	Treatment	Z-avg (nm)	PdI
Fraction D	no treatment	364	0.401
	frozen-thawed	2263	0.655
	frozen-thawed and ultrasonicated	580	0.491
Fraction E	no treatment	325	0.519
	frozen-thawed	393	0.448
	frozen-thawed and ultrasonicated	195	0.265

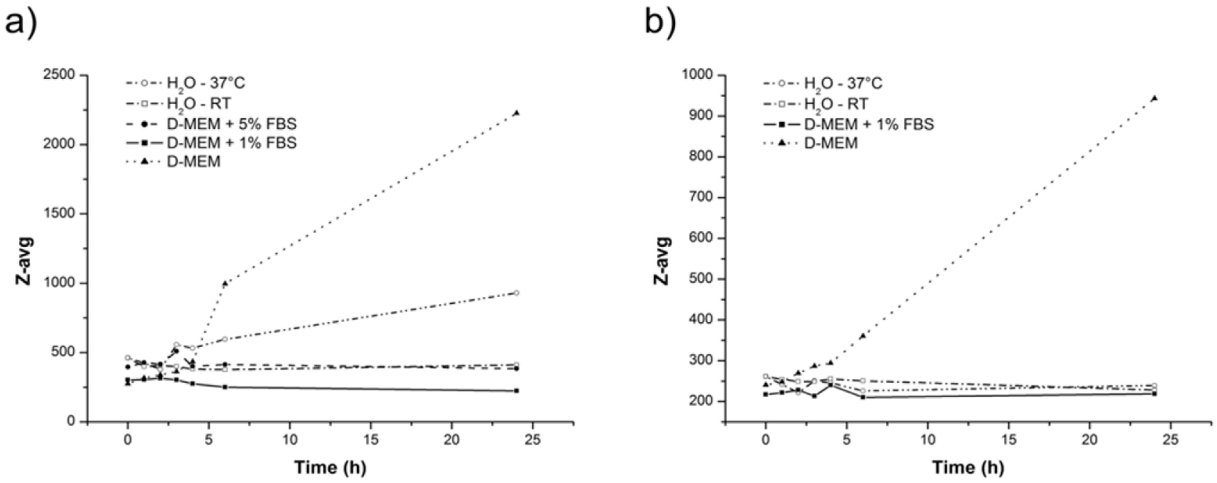

Fig. 8. Agglomeration of PM fractions in cell culture medium without FBS. Stability of (a) lower accumulation fraction D and (b) ultrafine fraction E, represented by Z-average was determined by DLS in particle suspensions in water (at room temperature and at 37 °C), medium D-MEM without FBS and with 1% and 5% FBS (at 37 °C).

fraction E, as freezing and thawing had no effect on either Z-average or Polydispersity Index.

3.3. Changes of particle suspensions in growth medium used for in vitro toxicological experiments

The Z-average obtained by DLS technique was used as the most appropriate parameter to evaluate changes in particle number size distribution induced by medium used for *in vitro* exposure of cell cultures. The Z-average is the most stable parameter produced by the DLS technique and is sensitive to even small changes in the sample (Dynamic Light Scattering, Common terms defined, Malvern Instruments Limited, 2011).

Further, the stability of the particle suspensions during 24 h incubation at 37 °C was studied. Samples were incubated in water, cell culture medium (D-MEM), and in medium supplemented with FBS (1 or 5%) (Fig. 8). For fraction E, cell culture medium supplemented with 5% FBS was not used, because the signal of FBS proteins overlapped the signal of the particles. As it can be observed from Fig. 8, whereas both samples were stable in medium supplemented with FBS, there was a massive agglomeration in the case of medium without FBS. Based on this evidence it can be concluded, that, for exposure of cells cultivated *in vitro*, medium supplemented by FBS is more suitable than the medium without FBS.

4. Discussion

In contrast to the organic or water extracts of aerosols, studies employing whole particles are challenging, because the handling of PM samples and experimental conditions may significantly affect the characteristics of the samples. Particle agglomeration and precipitation may often occur during the preparation of samples for *in vitro* studies. Regardless of this, these events are only rarely being monitored in many studies, although the use of incorrectly prepared PM samples for cell culture studies may affect their results and interpretations. Therefore, the characterization of PM size distribution in samples, as well as its monitoring in cell culture media before and during the exposure, should be an integral part of *in vitro* studies (Nature Nanotechnology Editorial, 2012; Krug and Wick, 2011).

One of major aims of this study was to investigate the changes in particle size distribution during the sample preparation. Our preliminary experiments showed that methanol extraction followed by evaporation led to formation of coarse precipitates, which resisted the ultrasonic homogenization after the resuspension in water (data not shown). The presence of coarse precipitates in the lower accumulation and ultrafine fractions in water implicated that the precipitated particles could become unavailable for cellular uptake in cell culture experiments. Therefore, we used the ultrasonic extraction into water according Gualtieri et al. (2009). This procedure had excellent efficiency in particle extraction from PUF substrates, but poor in the case of Teflon filter. In compliance with our finding, Thomson et al. (2015) reported 90% extraction efficiency for PUF substrates and 40% for polypropylene backup filters sampled by the same high volume cascade impactor, but employing methanol extraction. Large precipitates were not observed in the ultrafine and lower accumulation PM fractions ultrasonically extracted into the water in the present study.

In order to describe the impact of the ultrasonic treatment in detail, we then used TEM to evaluate the size of the individually occurring particles and agglomerates/aggregates in fraction D thawed and vortexed before and after the ultrasonic treatment. We found by TEM that freezing and thawing of lower accumulation fraction D suspended in water resulted in the agglomeration, but the treatment in ultrasonic bath indeed caused disagglomeration to smaller agglomerates or individual particles. Although simple determination of agglomerate/aggregate diameter in TEM may not provide accurate information in comparison with other more complex parameters, such as aspect ratio, or fractal-like dimension D_f and pre-exponential factor k (the last two used to characterize the ns-soot with branched fractal-like structure) (Eggersdorfer and Pratsinis, 2012; Murr et al., 2006; Wozniak et al., 2012), here we preferred to use this single parameter to provide the information about the changes of the sample during its handling.

As the water suspension of fraction E (< 170 nm) did not contain enough particles for TEM evaluation, this fraction was characterized only by the DLS method, together with the lower accumulation fraction D. Although the DLS is more suitable for less polydisperse samples than aerosol PM fractions, basic information about the disagglomeration of the sample can easily be gained from the changes of parameters as Z-average and index of polydispersity. DLS confirmed, that freezing and thawing caused agglomeration of the lower accumulation fraction D, and ultrasonic treatment de-agglomerated them to the level similar to that after the ultrasonic extraction from the PUF substrate to water. Contrary, Z-average and index of polydispersity were only slightly modulated after freezing/thawing in the water suspension of ultrafine fraction E.

The state of agglomeration of PM water suspension may also change after their addition into the cell culture media due to the presence of proteins, which may adsorb to particles in seconds forming nanoparticle-protein corona (Ehrenberg et al., 2009; Lynch and Dawson, 2008; Monopoli et al., 2012; Saptarshi et al., 2013). The DLS measurement of the agglomeration state of various engineered nanoparticles showed that

nanomaterials in solution might form coarse agglomerates in cell culture media without serum, which was dimished in the presence of serum. Nevertheless, different types of particles might interact in different ways (Murdock et al., 2008; Rischitor et al., 2016; Saptarshi et al., 2013; Sun et al., 2011; Tantra et al., 2010). To our knowledge, the DLS measurement of agglomeration state of aerosol samples during experimental conditions has not been evaluated so far. In our study, aerosol lower accumulation and ultrafine fractions were stable in cell culture media supplemented with 1% or 5% FBS during 24 h as detected by DLS analysis, while in media without FBS, a high degree of agglomeration was observed. This is in accordance with DLS measurement of diesel particulate matter SRM 2975, a sample close in character to the aerosol samples used in this study, which agglomerated in PBS without stabiliser, while agglomeration did not occur in PBS containing human serum albumin, Tween or mouse serum (Bihari et al., 2008).

Characterization of elemental composition, particle types and size distribution in size-segregated fractions was another aim of this study. The size-segregated samples were not clearly differentiated according to particle size, as they were segregated according to their aerodynamic diameter (Demokritou et al., 2002), therefore might frequently contain also particles of larger and/or smaller geometric diameter, that do not correspond to the respective cut points. This could be also related to agglomeration/aggregation of particles (Loxham et al., 2013; Ondov et al., 1978) in the ambient air or during the sampling.

Moreover, the stated cut points of the size fractions collected by each impaction stage are not perfectly sharp cut-offs, but correspond to 50% collection efficiency inflection points on S-shaped curves. Therefore, on each stage there will also be a tail of smaller d_{ae} particles which are collected with < 50% efficiency, as well as a tail of larger d_{ae} particles which had < 50% collection efficiency in the previous (larger d_{ae}) size stage, and are therefore still remaining in the air stream to be collected by the stage in question which follows. Wall and interstage losses or bounce-off may also occur in cascade impactors (Ondov et al., 1978), but these events are reduced in the case of using PUF as impaction substrates in high volume cascade impactor (Demokritou et al., 2002; Sillanpaa et al., 2003).

Although there were differences in the composition of fractions (Table 1), ns-soot occurred in all size fractions as already noted in other recent studies (Čupr et al., 2013; Smith et al., 2012). In summary, fraction B (1–10 μm) contained rock-forming minerals, high-temperature derived aluminosilicates, metallic particles, and ns-soot. In fraction C (0.5–1 μm) carbonaceous particles, ns-soot, inorganic particles, and Fe-rich metallic nanospheres were identified. Lower accumulation fraction D (0.17–0.5 μm) contained ns-soot, carbonaceous particles, inorganic particles sensitive to electron beam (K, Na and S-rich), and Fe-rich metallic nanospheres. In ultrafine fraction E (< 170 nm) ns-soot and Ca/K and S-rich inorganic particles sensitive to electron beam were identified.

Fe-rich metallic nanospheres with diameter 5 nm up to 120 nm, which were frequently identified in fraction C and D, were not found in our ultrafine sample. The occurrence of Fe-rich nanospheres in fraction C and D in our study suggests, that certain ultrafine nanoparticles may be impacted on higher size fractions and therefore not included in the ultrafine fraction, although iron belongs to the most abundant metals detected by chemical analysis of ultrafine fractions in several studies (Jalava et al., 2015; Pennanen et al., 2007), reviewed by (Sanderson et al., 2014). Due to the size and spherical shape of Fe-rich nanoparticles identified in this study, their traffic origin can be assumed (Kukutschova et al., 2011; Liati et al., 2015; Miller et al., 2007). Nevertheless, as the sampling site was not located in the proximity to any high traffic road, but in the University garden near a school yard with an episodically used small parking lot, the rather frequent occurrence of Fe-rich nanoparticles in our samples is noteworthy. Similar combustion-derived iron-rich nanospheres were recently found in human brain samples, pointing out that such polluting nanoparticles may have, among others, impact on neurodegenerative diseases (Maher et al., 2016).

5. Conclusions

In this study, electron microscopy, energy dispersive X-ray spectroscopy, and dynamic light scattering were used for characterization of the size segregated particulate matter trapped on the sampling substrates and during sample preparation preceding toxicological *in vitro* tests. The size-segregated samples were not clearly differentiated according to particle size. Ns-soot occurred in all size fractions and metallic nanospheres were found on higher impaction stages. However, certain differences in elemental composition of size-segregated fractions were found. Particulate matter was extracted by sonication from the PUF substrates and Teflon filter directly into water. The extraction efficiency was high for particles sampled on PUF substrates, but low for ultrafine particles on Teflon filter. Stability of extracted aerosol particles differs with respect to presence of fetal bovine serum (FBS). While the lower accumulation and ultrafine fractions were stable in cell culture media supplemented with FBS, high agglomeration occurred in media without FBS as measured during 24 h. This confirms that the character of the particulate matter sample might not change during the cell culture experiments while using media with FBS.

It is also important to take into account, that actual ambient air particulate size distribution may differ from that determined by a cascade impactor. The conversion of integrated impactor measurements to continuous size distribution is a rather complicated task. Therefore, concurrent on-line aerosol particle size distribution measurements should be conducted when performing toxicological studies of size fractionated samples. Also, detailed aerosol particle characterization in cell culture media both prior and during the exposure should be an integral part of such *in vitro* studies.

Funding

This work was supported by the Czech Science Foundation project No. P503-12-G147.

Conflicts of interest

None.

Acknowledgement

The authors would like to thank to Martin Racek (Institute of Petrology and Structural Geology, Faculty of Science, Charles University, Prague) for the determination of mineral types according to EDX spectra, as well as Jan Vondráček (Institute of Biophysics of the CAS, Department of Cytokinetics) for critical reading of the manuscript.

Appendix B. Supplementary data

Supplementary data related to this article can be found at http://dx.doi.org/10.1016/j.atmosenv.2018.02.004.

List of abbreviations

DLS	dynamic light scattering
D-MEM	Dulbecco's Modified Eagle's medium
EDX	energy-dispersive X-ray spectroscopy
FBS	fetal bovine serum
NPs	nanoparticles
PdI	polydispersity index
PM	particulate matter
PUF	polyurethane foam
SEM	scanning electron microscopy
STEM	scanning electron microscopy in transmission mode
TEM	transmission electron microscopy

References

Andre, V., Billet, S., Pottier, D., Le Goff, J., Pottier, I., Garcon, G., Shirali, P., Sichel, F., 2011. Mutagenicity and genotoxicity of PM2.5 issued from an urbano-industrialized area of Dunkerque (France). J. Appl. Toxicol. 31, 131–138.

Becker, S., Soukup, J.M., Sioutas, C., Cassee, F.R., 2003. Response of human alveolar macrophages to ultrafine, fine, and coarse urban air pollution particles. Exp. Lung Res. 29–44.

Bihari, P., Vippola, M., Schultes, S., Praetner, M., Khandoga, A.G., Reichel, C.A., Coester, C., Tuomi, T., Rehberg, M., Krombach, F., 2008. Optimized dispersion of nanoparticles for biological in vitro and in vivo studies. Part. Fibre Toxicol. 5, 14.

Billet, S., Garcon, G., Dagher, Z., Verdin, A., Ledoux, F., Cazier, F., Courcot, D., Aboukais, A., Shirali, P., 2007. Ambient particulate matter (PM2.5): physicochemical characterization and metabolic activation of the organic fraction in human lung epithelial cells (A549). Environ. Res. 105, 212–223.

Billet, S., Abbas, I., Le Goff, J., Verdin, A., Andre, V., Lafargue, P.E., Hachimi, A., Cazier, F., Sichel, F., Shirali, P., Garcon, G., 2008. Genotoxic potential of Polycyclic Aromatic Hydrocarbons-coated onto airborne Particulate Matter (PM 2.5) in human lung epithelial A549 cells. Canc. Lett. 270, 144–155.

Boström, C.-E., Gerde, P., Hanberg, A., Jernström, B., Johansson, C., Kyrklund, T., Rannug, A., Törnqvist, M., Victorin, K., Westerholm, R., 2002. Cancer risk assessment, indicators, and guidelines for polycyclic aromatic hydrocarbons in the ambient air. Environmental health Perspectives 110 (Suppl. 3), 451–488.

Buseck, P.R., Adachi, K., Gelencsér, A., Tompa, É., Pósfai, M., 2014. Ns-soot: a material-based term for strongly light-absorbing carbonaceous particles. Aerosol. Sci. Technol. 48, 777–788.

Cass, G.R., Hughes, L.A., Bhave, P., Kleeman, M.J., Allen, J.O., Salmon, L.G., 2000. The chemical composition of atmospheric ultrafine particles. Phil. Trans. Biol. Sci. 358, 2581–2592.

Chen, Y., Shah, N., Huggins, F.E., Huffman, G.P., 2006. Microanalysis of ambient particles from Lexington, KY, by electron microscopy. Atmos. Environ. 40, 651–663.

Čupr, P., Flegrová, Z., Franců, J., Landlová, L., Klanová, J., 2013. Mineralogical, chemical and toxicological characterization of urban air particles. Environ. Int. 54, 26–34.

Demokritou, P., Kavouras, I.G., Ferguson, S.T., Koutrakis, P., 2002. Development of a high volume cascade impactor for toxicological and chemical characterization studies. Aerosol. Sci. Technol. 36, 925–933.

Deshmukh, A.A., Mhlanga, S.D., Coville, N.J., 2010. Carbon spheres. Mater. Sci. Eng. R Rep. 70, 1–28.

Donaldson, K., Tran, L., Jimenez, L.A., Duffin, R., Newby, D.E., Mills, N., MacNee, W., Stone, V., 2005. Combustion-derived nanoparticles: a review of their toxicology following inhalation exposure. Part. Fibre Toxicol. 2, 10.

Eggersdorfer, M.L., Pratsinis, S.E., 2012. The structure of agglomerates consisting of polydisperse particles. Aerosol. Sci. Technol. 46, 347–353.

Ehrenberg, M.S., Friedman, A.E., Finkelstein, J.N., Oberdorster, G., McGrath, J.L., 2009. The influence of protein adsorption on nanoparticle association with cultured endothelial cells. Biomaterials 30, 603–610.

Gualtieri, M., Mantecca, P., Corvaja, V., Longhin, E., Perrone, M.G., Bolzacchini, E., Camatini, M., 2009. Winter fine particulate matter from Milan induces morphological and functional alterations in human pulmonary epithelial cells (A549). Toxicol. Lett. 188, 52–62.

Gualtieri, M., Longhin, E., Mattioli, M., Mantecca, P., Tinaglia, V., Mangano, E., Proverbio, M.C., Bestetti, G., Camatini, M., Battaglia, C., 2012. Gene expression profiling of A549 cells exposed to Milan PM2.5. Toxicol. Lett. 209, 136–145.

Gutierrez-Castillo, M.E., Roubicek, D.A., Cebrian-Garcia, M.E., De Vizcaya-Ruiz, A., Sordo-Cedeno, M., Ostrosky-Wegman, P., 2006. Effect of chemical composition on the induction of DNA damage by urban airborne particulate matter. Environ. Mol. Mutagen. 47, 199–211.

Hand, J.L., Malm, W.C., Laskin, A., Day, D., Lee, T., Wang, C., Carrico, C., Carrillo, J., Cowin, J.P., Collett, J., Iedema, M.J., 2005. Optical, physical, and chemical properties of tar balls observed during the yosemite aerosol characterization study. J. Geophys. Res. 110, D21210.

Hornberg, C., Maciuleviciute, L., Seemayer, N.H., Kainka, E., 1998. Induction of sister chromatid exchanges (SCE) in human tracheal epithelial cells by the fractions PM-10 and PM-2.5 of airborne particulates. Toxicol. Lett. 215–220.

Hughes, L.S., Cass, G.R., Gone, J., Ames, M., Olmez, I., 1998. Physical and chemical characterization of atmospheric ultrafine particles in the Los Angeles area. Environ. Sci. Technol. 32, 1153–1161.

IARC, 2014. Diesel and Gasoline Engine Exhausts and Some Nitroarenes. France, Lyon.

IARC, 2015. Outdoor Air Pollution. France, Lyon.

Jalava, P.I., Salonen, R.O., Halinen, A.I., Penttinen, P., Pennanen, A.S., Sillanpaa, M., Sandell, E., Hillamo, R., Hirvonen, M.R., 2006. In vitro inflammatory and cytotoxic effects of size-segregated particulate samples collected during long-range transport of wildfire smoke to Helsinki. Toxicol. Appl. Pharmacol. 215, 341–353.

Jalava, P.I., Wang, Q., Kuuspalo, K., Ruusunen, J., Hao, L., Fang, D., Väisänen, O., Ruuskanen, A., Sippula, O., Happo, M.S., Uski, O., Kasurinen, S., Torvela, T., Koponen, H., Lehtinen, K.E.J., Komppula, M., Gu, C., Jokiniemi, J., Hirvonen, M.R., 2015. Day and night variation in chemical composition and toxicological responses of size segregated urban air PM samples in a high air pollution situation. Atmos. Environ. 120, 427–437.

Krug, H.F., Wick, P., 2011. Nanotoxicology: an interdisciplinary challenge. Angew Chem. Int. Ed. Engl. 50, 1260–1278.

Kukutschova, J., Moravec, P., Tomasek, V., Matejka, V., Smolik, J., Schwarz, J., Seidlerova, J., Safarova, K., Filip, P., 2011. On airborne nano/micro-sized wear particles released from low-metallic automotive brakes. Environ. Pollut. 159, 998–1006.

Lepers, C., Dergham, M., Armand, L., Billet, S., Verdin, A., Andre, V., Pottier, D., Courcot, D., Shirali, P., Sichel, F., 2014. Mutagenicity and clastogenicity of native airborne particulate matter samples collected under industrial, urban or rural influence. Toxicol. Vitro 28, 866–874.

Liati, A., Pandurangi, S.S., Boulouchos, K., Schreiber, D., Arroyo rojas Dasilva, Y., 2015. Metal nanoparticles in diesel exhaust derived by in-cylinder melting of detached engine fragments. Atmos. Environ. 101, 34–40.

Libalova, H., Krckova, S., Uhlirova, K., Klema, J., Ciganek, M., Rossner Jr., P., Sram, R.J., Vondracek, J., Machala, M., Topinka, J., 2014a. Analysis of gene expression changes in A549 cells induced by organic compounds from respirable air particles. Mutat. Res. 770, 94–105.

Libalova, H., Krckova, S., Uhlirova, K., Milcova, A., Schmuczerova, J., Ciganek, M., Klema, J., Machala, M., Sram, R.J., Topinka, J., 2014b. Genotoxicity but not the AhR-mediated activity of PAHs is inhibited by other components of complex mixtures of ambient air pollutants. Toxicol. Lett. 225, 350–357.

Longhin, E., Holme, J.A., Gutzkow, K.B., Arlt, V.M., Kucab, J.E., Camatini, M., Gualtieri, M., 2013. Cell cycle alterations induced by urban PM2.5 in bronchial epithelial cells: characterization of the process and possible mechanisms involved. Part. Fibre Toxicol. 10.

Loxham, M., Cooper, M.J., Gerlofs-Nijland, M.E., Cassee, F.R., Davies, D.E., Palmer, M.R., Teagle, D.A., 2013. Physicochemical characterization of airborne particulate matter at a mainline underground railway station. Environ. Sci. Technol. 47, 3614–3622.

Lynch, I., Dawson, K.A., 2008. Protein-nanoparticle interactions. Nano Today 3, 40–47.

Maher, B.A., Ahmed, I.A.M., Karloukovski, V., MacLaren, D.A., Foulds, P.G., Allsop, D., Mann, D.M.A., Torres-Jardon, R., Calderon-Garciduenas, L., 2016. Magnetite pollution nanoparticles in the human brain. Proc. Natl. Acad. Sci. 113, 10797–10801.

Miller, A., Ahlstrand, G., Kittelson, D., Zachariah, M., 2007. The fate of metal (Fe) during diesel combustion: morphology, chemistry, and formation pathways of nanoparticles. Combust. Flame 149, 129–143.

Monopoli, M.P., Aberg, C., Salvati, A., Dawson, K.A., 2012. Biomolecular coronas provide the biological identity of nanosized materials. Nat. Nanotechnol. 7, 779–786.

Murdock, R.C., Braydich-Stolle, L., Schrand, A.M., Schlager, J.J., Hussain, S.M., 2008. Characterization of nanomaterial dispersion in solution prior to in vitro exposure using dynamic light scattering technique. Toxicol. Sci. 101, 239–253.

Murr, L.E., Soto, K.F., Garza, K.M., Guerrero, P.A., Martinez, F., Esquivel, E.V., Ramirez, D.A., Shi, Y., Bang, J.J., Venzor, J.r, 2006. Combustion-generated nanoparticulates in the El Paso, TX, USA/Juarez, Mexico Metroplex: their comparative characterization and potential for adverse health effects. Int. J. Environ. Res. Publ. Health 3, 48–66.

Nature Nanotechnology Editorial, 2012. Join the dialogue. Nat. Nanotechnol. 7, 545.

Oberdorster, G., Oberdorster, E., Oberdorster, J., 2005. Nanotoxicology: an emerging discipline evolving from studies of ultrafine particles. Environ. Health Perspect. 113, 823–839.

Ondov, J.M., Ragaini, R.C., Biermann, A.H., 1978. Elemental particle-size emissions from coal-fired power plants: use of an inertial cascade impactor. Atmos. Environ. 12, 1175–1185.

Pennanen, A.S., Sillanpaa, M., Hillamo, R., Quass, U., John, A.C., Branis, M., Hunova, I., Meliefste, K., Janssen, N.A., Koskentalo, T., Castano-Vinyals, G., Bouso, L., Chalbot, M.C., Kavouras, I.G., Salonen, R.O., 2007. Performance of a high-volume cascade impactor in six European urban environments: mass measurement and chemical characterization of size-segregated particulate samples. Sci. Total Environ. 374, 297–310.

Pósfai, M., Simonics, R., Li, J., Hobbs, P.V., Buseck, P.R., 2003. Individual aerosol particles from biomass burning in southern Africa: 1. Compositions and size distributions of carbonaceous particles. J. Geophys. Res. Atmos. 108, 8483.

Pósfai, M., Gelencsér, A., Simonics, R., Arató, K., Li, J., Hobbs, P.V., Buseck, P.R., 2004. Atmospheric tar balls: particles from biomass and biofuel burning. J. Geophys. Res. Atmos. 109, D06213.

Ramgolam, K., Favez, O., Cachier, H., Gaudichet, A., Marano, F., Martinon, L., Baeza-Squiban, A., 2009. Size-partitioning of an urban aerosol to identify particle determinants involved in the proinflammatory response induced in airway epithelial cells. Part. Fibre Toxicol. 6, 10.

Reibman, J., Hsu, Y., Chen, L.C., Kumar, A., Su, W.C., Choy, W., Talbot, A., Gordon, T., 2002. Size fractions of ambient particulate matter induce granulocyte macrophage colony-stimulating factor in human bronchial epithelial cells by mitogen-activated protein kinase pathways. Am. J. Respir. Cell Mol. Biol. 27, 455–462.

Rischitor, G., Parracino, M., La Spina, R., Urban, P., Ojea-Jimenez, I., Bellido, E., Valsesia, A., Gioria, S., Capomaccio, R., Kinsner-Ovaskainen, A., Gilliland, D., Rossi, F., Colpo, P., 2016. Quantification of the cellular dose and characterization of nanoparticle transport during in vitro testing. Part. Fibre Toxicol. 13.

Sanderson, P., Delgado-Saborit, J.M., Harrison, R.M., 2014. A review of chemical and physical characterisation of atmospheric metallic nanoparticles. Atmos. Environ. 94, 353–365.

Saptarshi, S.R., Duschl, A., Lopata, A.L., 2013. Interaction of nanoparticles with proteins: relation to bio-reactivity of the nanoparticle. J. Nanobiotechnol. 11.

Sillanpaa, M., Hillamoa, R., Makela, T., Pennanen, A.S., Salonen, R.O., 2003. Field and laboratory tests of a high volume cascade impactor. J. Aerosol Sci. 34, 485–500.

Smith, S., Ward, M., Lin, R., Brydson, R., Dall'Osto, M., Harrison, R.M., 2012. Comparative study of single particle characterisation by Transmission Electron Microscopy and time-of-flight aerosol mass spectrometry in the London atmosphere. Atmos. Environ. 62, 400–407.

Sun, L., Li, Y., Liu, X., Jin, M., Zhang, L., Du, Z., Guo, C., Huang, P., Sun, Z., 2011. Cytotoxicity and mitochondrial damage caused by silica nanoparticles. Toxicol. Vitro 25, 1619–1629.

Tantra, R., Tompkins, J., Quincey, P., 2010. Characterisation of the de-agglomeration effects of bovine serum albumin on nanoparticles in aqueous suspension. Colloids Surf. B Biointerfaces 75, 275–281.

Thomson, E.M., Breznan, D., Karthikeyan, S., MacKinnon-Roy, C., Charland, J.P., Dabek-Zlotorzynska, E., Celo, V., Kumarathasan, P., Brook, J.R., Vincent, R., 2015. Cytotoxic and inflammatory potential of size-fractionated particulate matter collected repeatedly within a small urban area. Part. Fibre Toxicol. 12.

Topinka, J., Milcova, A., Schmuczerova, J., Krouzek, J., Hovorka, J., 2013. Ultrafine particles are not major carriers of carcinogenic PAHs and their genotoxicity in size-segregated aerosols. Mutat. Res. 754, 1–6.

Topinka, J., Rossner Jr., P., Milcova, A., Schmuczerova, J., Pencikova, K., Rossnerova, A., Ambroz, A., Stolcpartova, J., Bendl, J., Hovorka, J., Machala, M., 2015. Day-to-day variability of toxic events induced by organic compounds bound to size segregated atmospheric aerosol. Environ. Pollut. 202, 135–145.

Upadhyay, D., Panduri, V., Ghio, A., Kamp, D.W., 2003. Particulate matter induces alveolar epithelial cell DNA damage and apoptosis: role of free radicals and the mitochondria. Am. J. Respir. Cell Mol. Biol. 29, 180–187.

WHO, 2004. Health aspects of air pollution. In: Results from the WHO Project "Systematic Review of Health Aspects of Air Pollution in Europe". WHO, Kopenhagen, Denmark.

Wozniak, M., Onofri, F.R.A., Barbosa, S., Yon, J., Mroczka, J., 2012. Comparison of methods to derive morphological parameters of multi-fractal samples of particle aggregates from TEM images. J. Aerosol Sci. 47, 12–26.

Fig. S1. SEM micrographs showing morphology of airborne particle fractions B, C and D on PUF substrates, one day samples. Ns-soot can be seen on the image of fraction B and C. Magnification 7000x (fraction B and C), and 15000x (fraction D). Part of the PUF substrate is shown at lower magnification (100x).

Fraction B

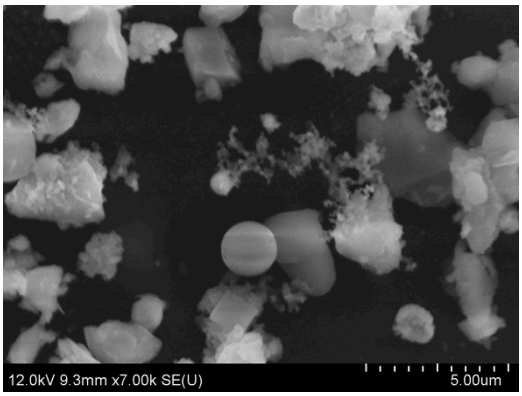

Fraction C

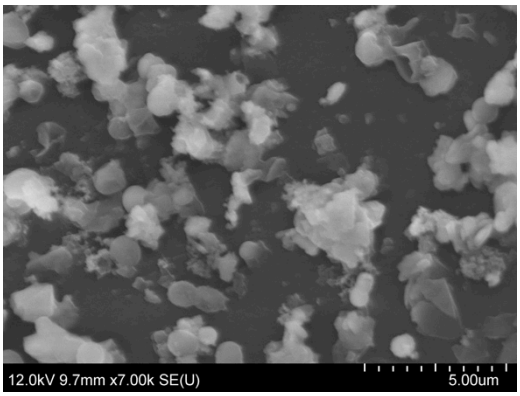

Fraction D

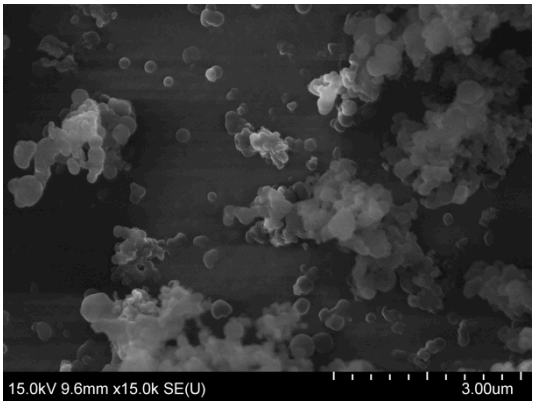

Fraction D

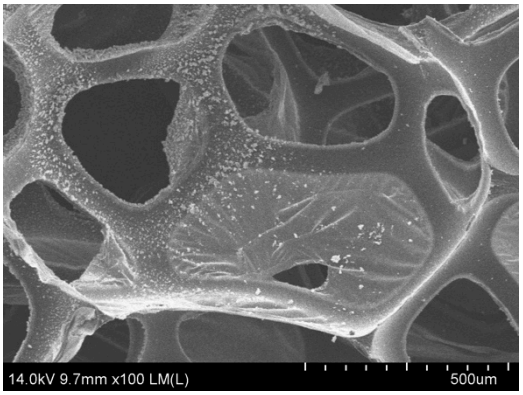

Fig. S2. Fraction B sampled 1 day on microscopic copper grid. (a) SEM micrograph of various particles. EDX analysis of (b) spherical aluminosilicate containing K, Ca, Fe; (c) mixture of various particles including aluminosilicates; (d) individual carbonaceous particle with diameter approx. 700 nm; (e) quartz; (f) iron oxide particle with diameter 200 x 250 nm. (g) STEM micrograph of ns-soot and its EDX spectrum (h). Cu on EDX graphs originates from background.

(a)

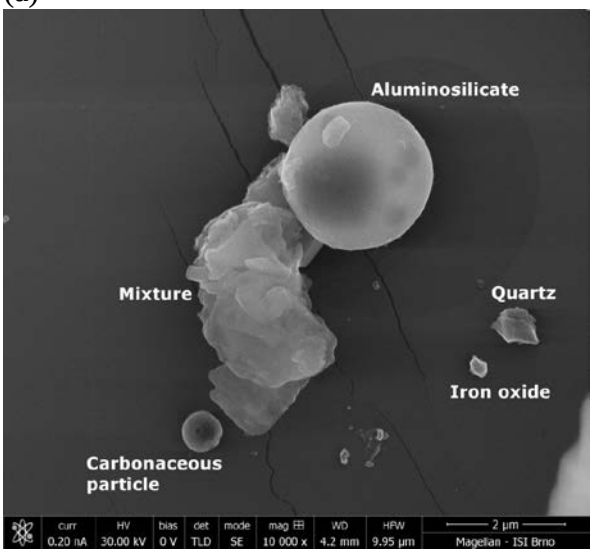

(b)

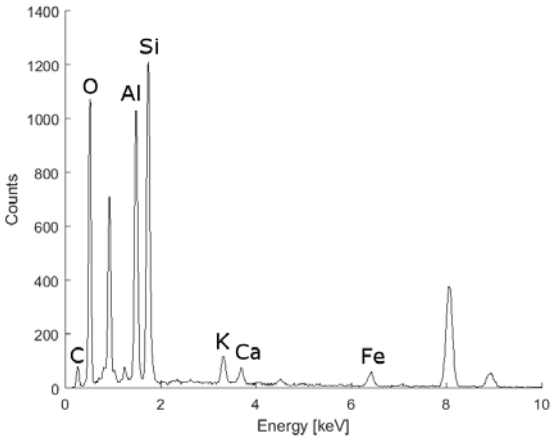

(c)

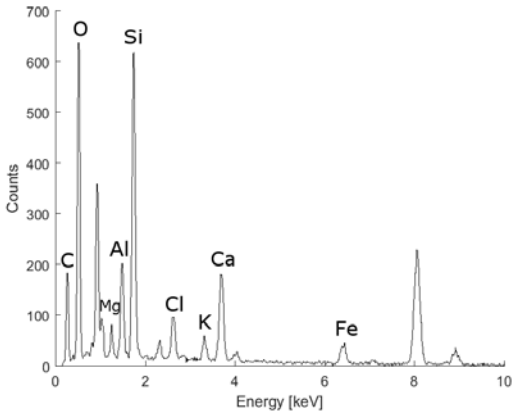

(d)

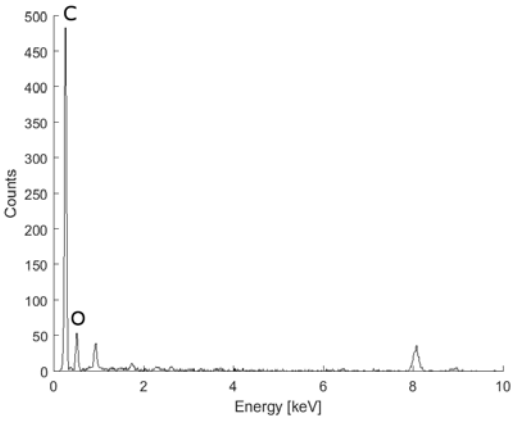

(e)

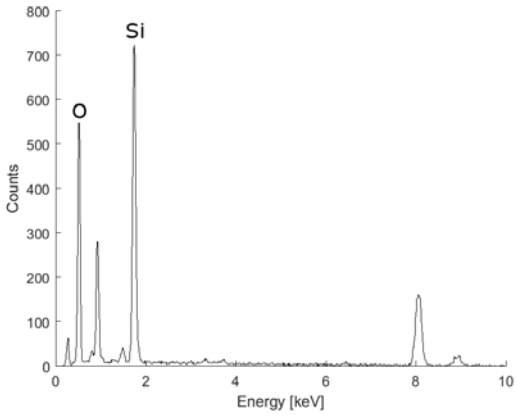

(f)

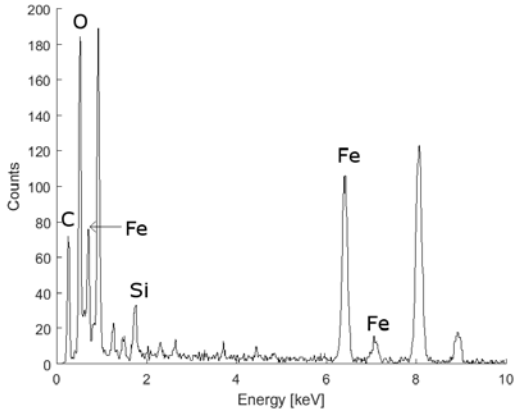

(g)

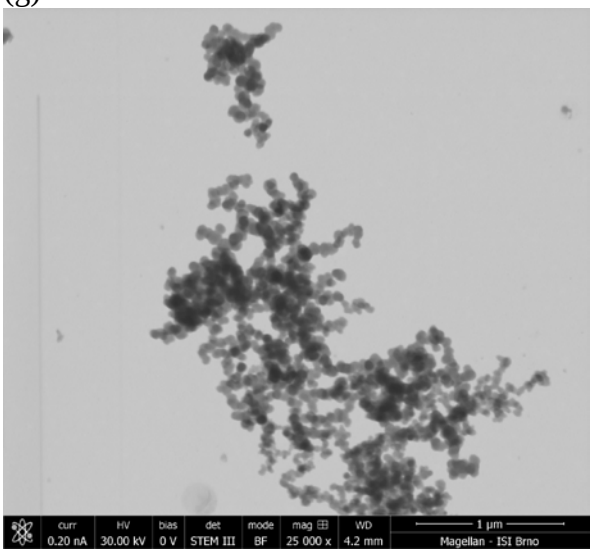
curr
0.20 nA
HV
30.00 kV
bias
0 V
det
STEM III
mode
BF
mag
25 000 x
WD
4.2 mm
1 µm
Magellan - ISI Brno

(h)

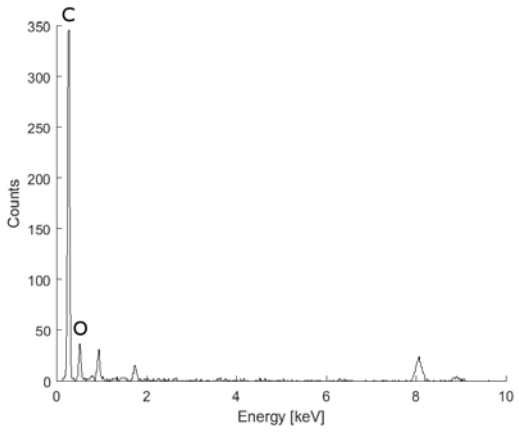
C
O
Counts
Energy [keV]
0
50
100
150
200
250
300
350
0
2
4
6
8
10

Fig. S3. Fraction C sampled 1 day on microscopic copper grid. (a) SEM micrograph and corresponding EDX spectra of carbonaceous sphere with diameter 950 nm (b) and aggregate of carbonaceous particles (c). STEM micrograph of crystalline calcium polysulphide (d) and its EDX spectrum (e). Agglomerate of iron nanoparticles with diameters ranging from 5 to 55 nm (f) and its EDX spectrum (g). Cu on EDX graphs originates from background.

(a)

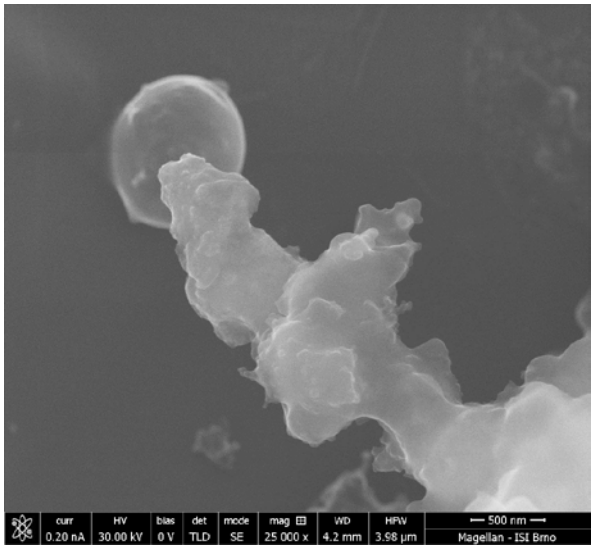

(b)

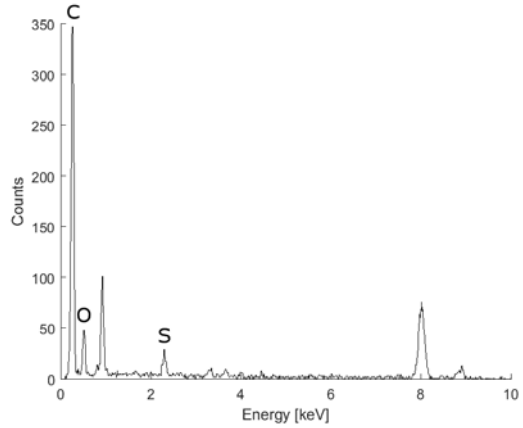

(c)

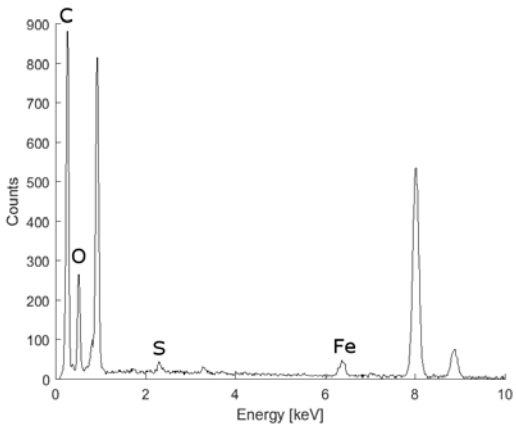

(d)

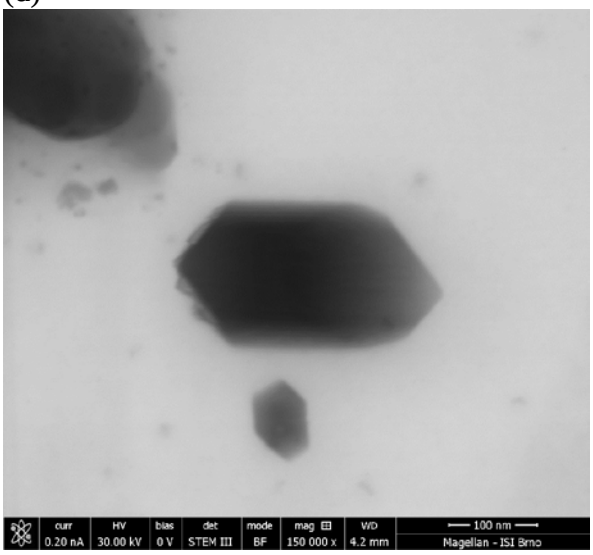
curr
0.20 nA
HV
30.00 kV
bias
0 V
det
STEM III
mode
BF
mag
150 000 x
WD
4.2 mm
100 nm
Magellan - ISI Brno

(e)

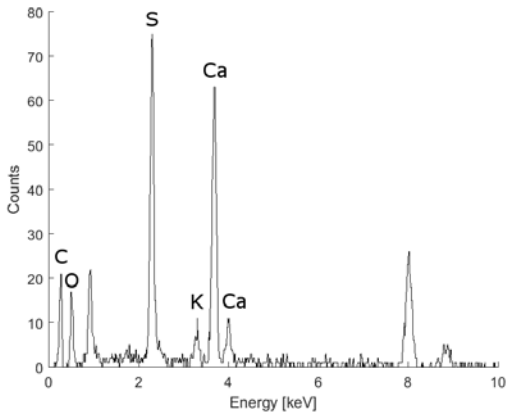
S
Ca
C
O
K
Ca
Counts
Energy [keV]

(f)

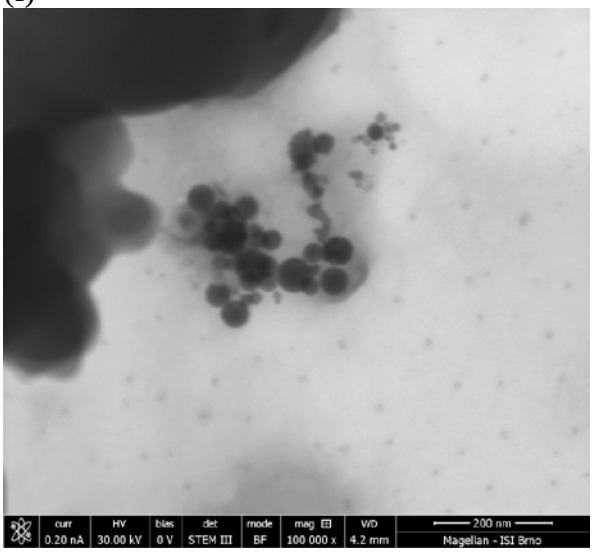
curr
0.20 nA
HV
30.00 kV
bias
0 V
det
STEM III
mode
BF
mag
100 000 x
WD
4.2 mm
200 nm
Magellan - ISI Brno

(g)

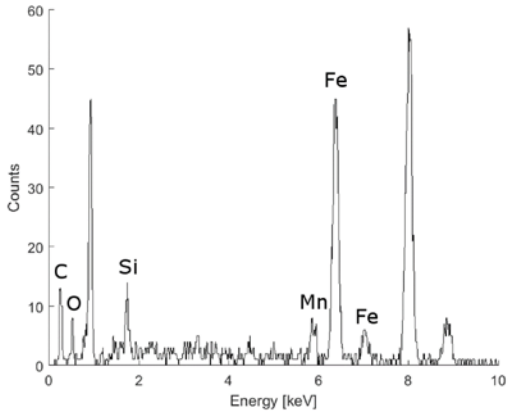
Fe
C
O
Si
Mn
Fe
Counts
Energy [keV]

Fig S4. Fraction D sampled 1 day on microscopic copper grid. (a) STEM micrograph of aged ns-soot agglomerated with crystallic potassium/sodium sulphate. EDX spectrum of ns-soot (b) and potassium/sodium sulphate (c).

(a)

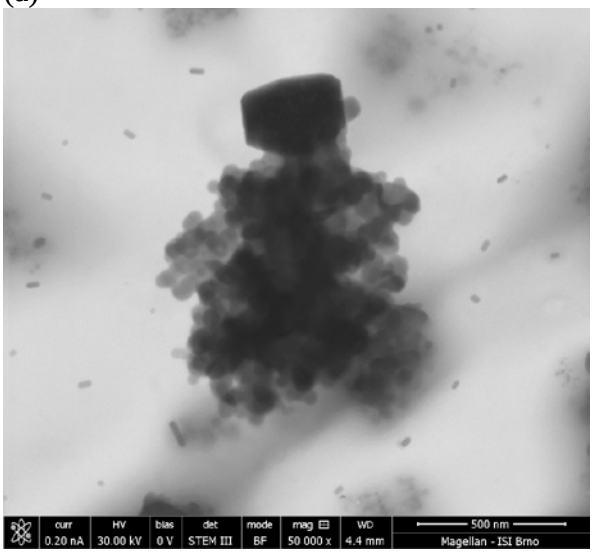

(b)

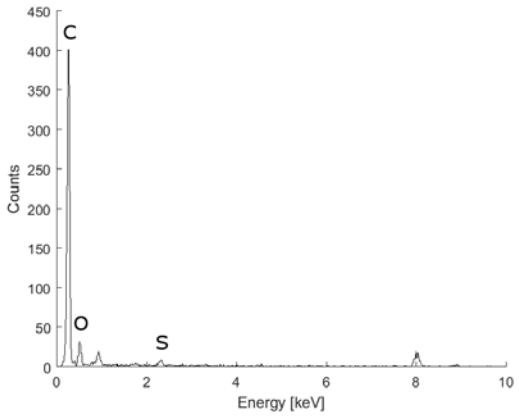

(c)

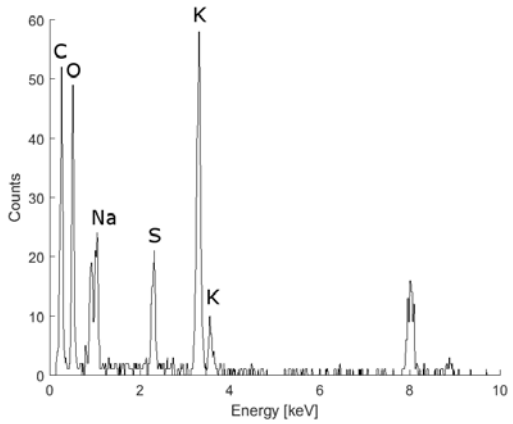

Fig S5. Iron-rich nanoparticles forming agglomerates of various sizes identified by EDX analysis in fraction D sampled 1 day on copper grids. Diameter of individual nanoparticles ranges from 5 nm to 120 nm. The EDX graphs (not shown here) are almost identical with the one shown on Fig. 3, containing Fe and trace amount of Si, S and Mn. The unsharpness of two images below is caused by higher probe current, which was used to increase EDX signal and improve the quality of captured spectra.

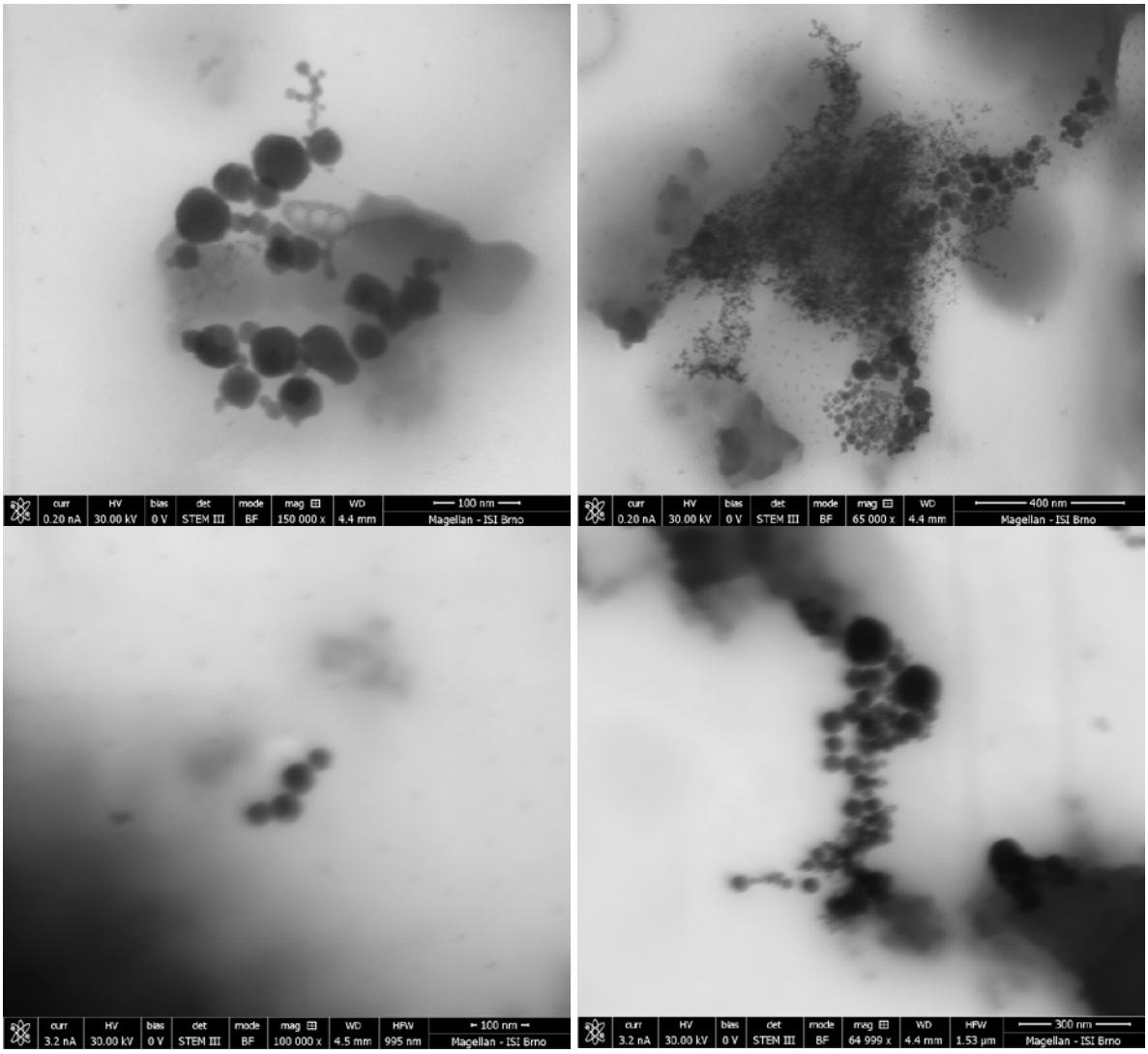

Fig S6. Fraction E sampled 1 day on microscopic copper grid. (a, b) STEM micrograph of ns-soot and its corresponding EDX spectrum. The unsharpness of the image is caused by higher probe current, which was used to increase EDX signal and improve the quality of captured spectrum. The quality of EDX spectrum is therefore higher, although the image is blurred. (c, d) STEM micrograph of calcium sulphate. Cu and Si originate from the background.

(a)

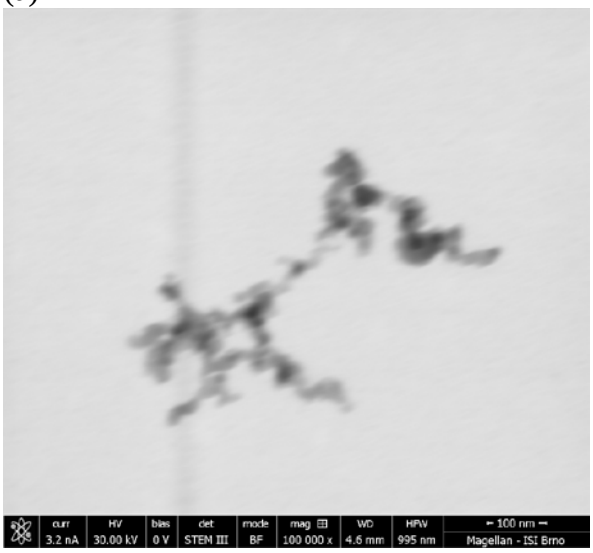

(b)

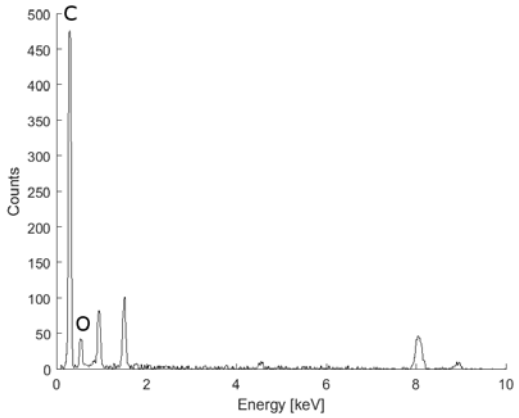

(c)

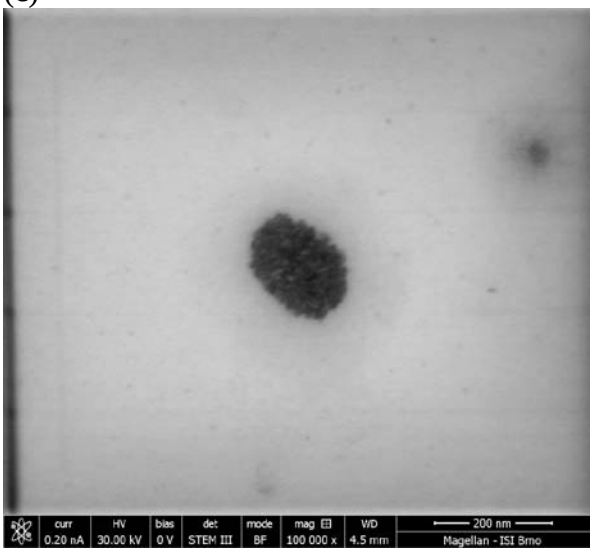

(d)

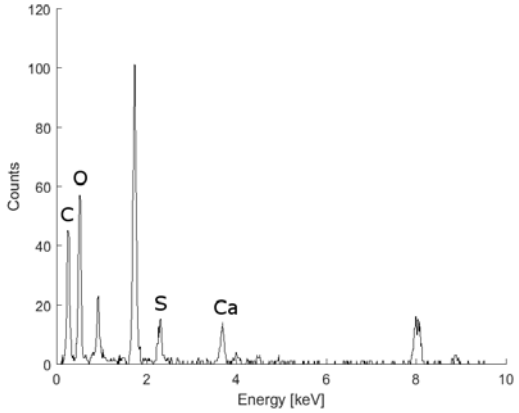

B.6 Application of advanced microscopic methods to study the interaction of carboxylated fluorescent nanodiamonds with membrane structures in THP-1 cells: Activation of inflammasome NLRP3 as the result of lysosome destabilisation

P. T. Knotigova, J. Masek, F. Hubatka, J. Kotoucek, P. Kulich, P. Simeckova, E. Bartheldyova, M. Machala, T. Svadlakova, J. Krejsek, N. Vaskovicova, **R. Skoupy**, V. Krzyzanek, S. Macaulay, M. Katzuba, L. Fekete, P. Ashcheulov, M. Raska, I. Kratochvilova, and J. Turanek. Application of Advanced Microscopic Methods to Study the Interaction of Carboxylated Fluorescent Nanodiamonds with Membrane Structures in THP-1 Cells: Activation of Inflammasome NLRP3 as the Result of Lysosome Destabilization. *Molecular Pharmaceutics*, 16(8):3441–3451, 8 2019. doi:10.1021/acs.molpharmaceut.9b00225

molecular pharmaceutics

Article

Cite This: Mol. Pharmaceutics 2019, 16, 3441−3451

pubs.acs.org/molecularpharmaceutics

Application of Advanced Microscopic Methods to Study the Interaction of Carboxylated Fluorescent Nanodiamonds with Membrane Structures in THP-1 Cells: Activation of Inflammasome NLRP3 as the Result of Lysosome Destabilization

Pavlína Turánek Knötigová,[†] Josef Mašek,[†] František Hubatka,[†] Jan Kotouček,[†] Pavel Kulich,[†] Pavlína Šimečková,[†] Eliška Bartheldyová,[†] Miroslav Machala,[†] Tereza Švadláková,[‡] Jan Krejsek,[‡] Naděžda Vaškovicová,[§] Radim Skoupý,[§] Vladislav Krzyžánek,[§] Stuart Macaulay,[∥] Michael Katzuba,[∥] Ladislav Fekete,[⊥] Petr Ashcheulov,[⊥] Milan Raška,*[,†,#] Irena Kratochvílová,*[,⊥] and Jaroslav Turánek*[,†]

[†]Veterinary Research Institute, Brno 62100, Czech Republic

[‡]Faculty of Medicine, Department of Clinical Immunology and Allergology, Charles University, Hradec Králové 500 03, Czech Republic

[§]Institute of Scientific Instruments, Czech Academy of Sciences, Brno 61264, Czech Republic

[∥]Malvern Instruments, Great Malvern WR14 1XZ, U.K.

[⊥]Institute of Physics of the Czech Academy of Sciences, Na Slovance 2, CZ-182 21, Prague 8, Czech Republic

[#]Department of Immunology, Faculty of Medicine and Dentistry, Palacky University Olomouc, Olomouc 775 15, Czech Republic

Supporting Information

ABSTRACT: Nanodiamonds (ND), especially fluorescent NDs, represent potentially applicable drug and probe carriers for in vitro/in vivo applications. The main purpose of this study was to relate physical−chemical properties of carboxylated NDs to their intracellular distribution and impact on membranes and cell immunity—activation of inflammasome in the in vitro THP-1 cell line model. Dynamic light scattering, nanoparticle tracking analysis, and microscopic methods were used to characterize ND particles and their intracellular distribution. Fluorescent NDs penetrated the cell membranes by both macropinocytosis and mechanical cutting through cell membranes. We proved accumulation of fluorescent NDs in lysosomes. In this case, lysosomes were destabilized and cathepsin B was released into the cytoplasm and triggered pathways leading to activation of inflammasome NLRP3, as detected in THP-1 cells. Activation of inflammasome by NDs represents an important event that could underlie the described toxicological effects in vivo induced by NDs. According to our knowledge, this is the first in vitro study demonstrating direct activation of inflammasome by NDs. These findings are important for understanding the mechanism(s) of action of ND complexes and explain the ambiguity of the existing toxicological data.

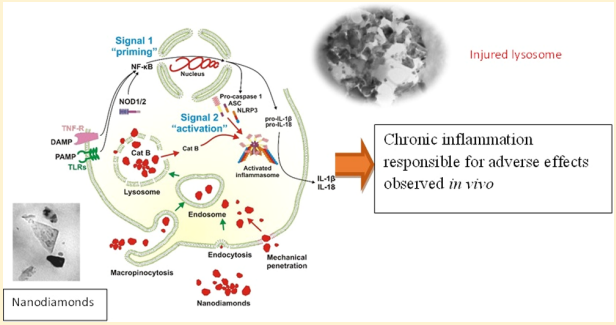

KEYWORDS: *fluorescent nanodiamonds, cell immunopathology, nanodiamond intercellular distribution, inflammation, inflammasome NLRP3, AFM, TEM, cathodoluminescence, macropinocytosis, THP-1 cells, cathepsin B, lysosomal disruption*

1. INTRODUCTION

Nanodiamonds (ND) have attracted a great deal of scientific attention for their potential in bioimaging and for their possible therapeutic applications due to their chemical inertness, useful surface properties, and stable fluorescence without photobleaching.[1−8] The fluorescence properties of NDs, as well as their cathodoluminescence, are of special interest for the development of nanosensors for in vivo and in vitro applications.[9−13] There is also increasing interest in exploring the modification of the surface of NDs, and alteration of their functionality by the attachment of various biomolecules to mediate interaction with specific cellular targets.[14] The broad area of applications includes the

Received: February 23, 2019
Revised: June 8, 2019
Accepted: June 11, 2019
Published: June 11, 2019

DOI: 10.1021/acs.molpharmaceut.9b00225
Mol. Pharmaceutics 2019, 16, 3441−3451

production of biosensors/biochips and biomedical nanorobots, drug, gene and protein carriers, protein purification, implant coating, and imaging probes.[15] Functionalized ND can be extremely useful for tumor targeting, intravascular bioimaging, and diagnostic and therapeutic purposes.[9,16,17] ND surface chemical modifications (e.g., by carboxylation, amination, PEGylation, biotinylation, etc.) could serve as a unique platform for bioconjugation.[1,17]

The potential applications of NDs in medicine raise questions regarding biosafety assessment.[18,19] Many papers addressed the important topics of ND biocompatibility and toxicity. Data on in vivo toxicity of NDs are limited and rather equivocal and conflicting. Although some reports indicate the safety of NDs documented in vitro using various cell lines as well as in vivo using murine animal models, several others have reported in vitro and in vivo toxicity and genotoxicity of various ND preparations.[19−21] Cell-specific toxicity correlated with NDs in macrophages and lymphocytes[22,23] has been reported recently. General cytotoxicity of NDs ranging in size from 2 to 10 nm was reported by in ref 24. The uptake of NDs into natural killer cells and monocytes has been studied in ref 25. ND concentration-dependent cytotoxic and inflammatory responses were described in the monoblastoid cell line U937 possibly via the TLR4 receptor and activation of the NF-κB signaling pathway.[26] But more specifically the activation of inflammasome has not been shown before. As a whole, immunopathology seems to be the main phenomenon behind the observed toxic effect induced by NDs.

Therefore, in this work we used pure carboxylated fluorescence NDs of 100 nm in size to study the effect of ND on activation of inflammasome as the key event responsible for inducing tissue inflammation. To explain the specific behavior of ND in cells, we used advanced physicochemical methods [dynamic light scattering (DLS) and nanoparticle tracking analysis (NTA)] and microscopic methods [confocal microscopy, electron microscopy (EM), cathodoluminescence, and atomic force microscopy (AFM)]. The main purpose of this study was to relate the physical−chemical properties of carboxylated NDs to their effect on biological membranes and activation of inflammasome in vitro THP-1 cell line derived from human monocytes. Activation of inflammasome and uncontrolled chronic inflammation is responsible for a variety of immunopathologies. Chronic inflammation can be induced by a variety of nanoparticles which are difficult to remove from the organism and tend to accumulate in particular tissues and organs. NDs represent such particles, and activation of inflammasome can be assumed to be the main factor responsible for the observed in vivo toxic effect of NDs. According to our knowledge this is the first in vitro study demonstrating direct activation of inflammasome by NDs. Fluorescent NDs with proper chemical terminations can be used for monitoring the processes and states in the living cells but it should be taken into account that the cell can be destructed by the penetration of the ND. Finding the right biological application of technically very attractive diamond nanoparticles is a great challenge for the future.

2. EXPERIMENTAL SECTION

2.1. ND Particles. Fluorescent ND slurries denoted as ND-NV-100 nm were purchased from Adámas Nanotechnologies (Raleigh, NC, USA). (http://adamasnano.com/fnd100nmndnv.html). These were 1 mg/mL suspensions of carboxylated ND in deionized water; their nominal average particle size was 100 nm.

2.2. DLS, Multiangle Light Scattering, and NTA. The batch measurements of the size distribution of the samples were carried out both by DLS (Zetasizer Ultra, Malvern, UK) and by the NTA technique using an instrument NanoSight NS500-HS (Malvern, UK) with a laser wavelength of 488 nm, sCMOS camera, and NTA 3.0 software. The effect of pH on the ζ potential of carboxylated NDs was measured using the Zetasizer Ultra a ζ-potential cuvette (DTS 1061, Malvern). Sodium phosphate buffer (10 mM; pH range 2−8) was used. Software ZS explorer was applied for calculation of particle concentration.

Multiangle light scattering (MALS) batch measurement was done by the instrument DAWN HELIOS II (Wyatt) at a concentration 20 μg/mL in deionized water.

2.3. Electron Microscopy. *2.3.1. Transmission EM.* Samples of NDs were suspended in a drop of MilliQ water. The resulting suspension was covered with a carbon-coated grid (300 Old Mesch, Agar Scientific, Austria). The grid was removed from the suspension after 1 min and the residual water was dried with a strip of filtration paper. The samples were observed under a Philips 208 S Morgagni transmission electron microscope (FEI, Czech Republic) at 7500× magnification and at an accelerating voltage of 80 kV. The size of 100 prisms was measured.

The ultrathin section method was performed as follows: 3% glutaraldehyde-fixed THP-1 cells 24 h exposed to fND (10 μg/mL) were centrifuged and the pellet was rinsed in Millonig buffer, postfixed in 1% OsO4 solution in Millonig buffer, dehydrated in 50, 70, 90, and 100% ethanol, embedded in LR white resin (Sigma-Aldrich, Germany) and polymerized at 60 °C for 72 h. Ultrathin sections (the thickness of 70 nm) were cut with glass knives on a UC 7 ultramicrotome (UC 7, Leica, Austria). Afterwards, they were directly observed without being previously contrasted to prevent objectionable artifacts. The sections were examined under a Philips EM 208 S Morgagni transmission electron microscope (FEI, Czech Republic) at an accelerating voltage 80 kV.

2.3.2. Scanning EM and Freeze Fracture Techniques. A dense suspension of cells (density 10^8 per mL) was frozen by a high pressure freezer Leica EM ICE (Leica Microsystems) on 3 mm gold carriers. The samples were totally freeze-dried in a high vacuum sputter coater Leica EM ACE 600 (Leica Microsystems) at a temperature −95 °C overnight. For imaging, the samples were transferred to a high resolution scanning EM (SEM) Magellan 400L (FEI) via cryo transfer system Leica EM VTC 100 (Leica Microsystems). The SEM is equipped with a detector MonoCL4 Plus (Gatan) for cathodoluminescence investigations. High resolution secondary electron images were captured at an acceleration voltage in the range 2−3 kV in a low dose, the cathodoluminescence investigations were performed at the acceleration voltage in the range 7−15 kV and the probe current of 6.4 nA.

For transmission EM (TEM) imaging, 70 nm sections of cells were prepared. This section size was considered optimum for TEM imaging because of a good contrast and resolution, while keeping an acceptable percentage of samples not destroyed by cutting and tearing by using large NDs (examples in Supporting Information).

2.3.3. Atomic Force Microscopy. NDs were characterized by a Dimension Icon AFM from Bruker Company. Standard tips Tap150al-g with a resonant frequency of 150 kHz and

DOI: 10.1021/acs.molpharmaceut.9b00225
Mol. Pharmaceutics 2019, 16, 3441−3451

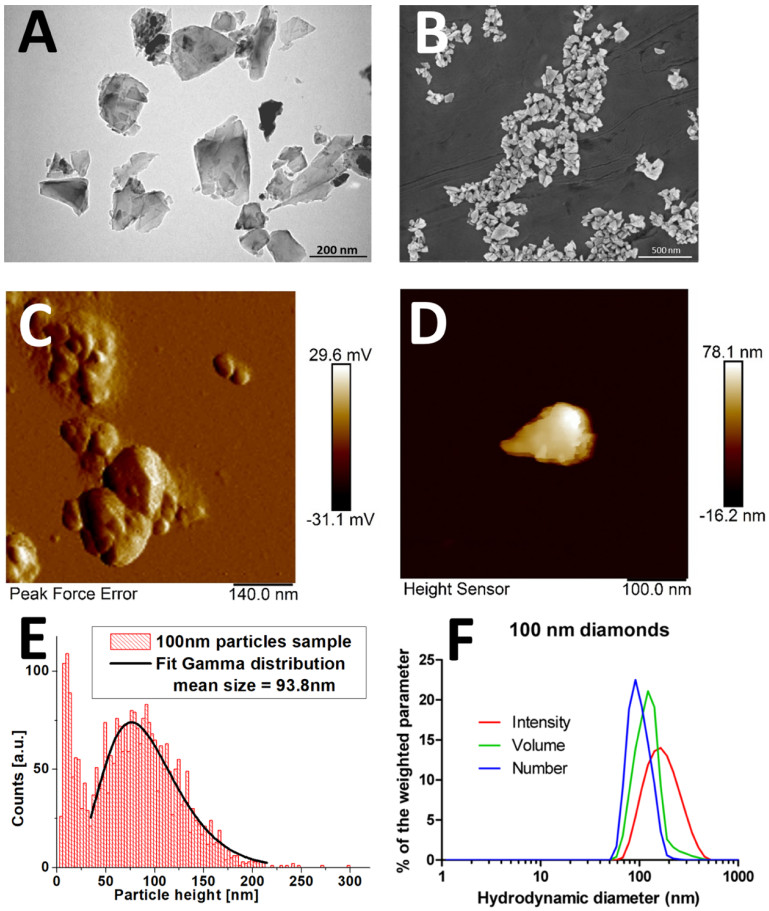

Figure 1. Characterization of ND—shape, size, and size distribution. Transmission and scanning electron micrographs of the 100 nm ND samples revealing their specific morphology and variability in their shape and size; (A) TEM detail of the structure of the 100 nm sample; (B) SEM of NDs. (C) Atomic force micrographs of the ND samples; (D) detail of the structure of the 100 nm ND sample; (E) size distribution of ND analyses by AFM; (F) the size distribution of the ND samples as determined by DLS (Zetasizer Nano-ZS, Malvern, UK); batch measurements, milliQ-water suspensions, *Z*-average (d.nm) 181.8, PDI 0.127.

nominal tip radius of 10 nm were used for the measurements. The particles were dissolved in ultra-pure deionized water and dropped on Si wafer. In the case of images for the analysis of the particle size distribution the areas of 5 μm × 5 μm were depicted with a resolution of 512 points × 512 points. All images were taken in the ScanAsyst measurement mode. The size of the particles was determined as the measured height of the particles.

2.4. Confocal Microscopy. A SP-2 confocal microscope (Leica) was used to visualize fluorescent ND in cells, colocalization studies of NDs with early endosomes and lysosomes, and release of cathepsin B from lysosomes. The images were scanned at 400 Hz using a 63× Leica oil immersion objective (numeric aperture, 1.4). An argon 488 nm laser was used for excitation of the Rab5a-GFP protein and LysoTracker, 561 nm laser was used for fluorescence excitation of NDs, and 458 nm laser was used for visualization of NDs in the reflectance mode.

2.4.1. Colocalization of NDs with Early Endosomes and Lysosomes. Early endosomes: THP-1 cells were transfected using CellLight® Rab5a-GFP *BacMam 2.0 (Molecular Probe, cat. No. C10586) according to the manufacturer's instructions, prior to the treatment with NDs. Lysosomes: THP-1 cells were incubated with 100 nM LysoTracker® Green DND-26 (molecular probe, Cat. no. L7526) 1 hour prior to observation by confocal microscopy, according to the manufacturer's instructions. The THP-1 cells were incubated with ND (final concentration 10 μg/mL and observed in μ-slide 8 well ibiTreat (IBIDI, Martinsried, Germany) after 4 h incubation.

2.4.2. Release of Cathepsin B. Detection of cathepsin B was performed by a cathepsin B detection kit (Enzo Life Sciences) according to the manufacturer's protocol. CV-(RR)2 was used as the substrate for the cathepsin B cleavage. As a positive control, lysosomal disruptor Leu-Leu methyl ester hydrobromide (LLME) (Sigma-Aldrich) in the final concentration of 100 μM was used. THP-1 null cells were pretreated by a lysosomal disruptor for 2 h. THP-1 null cells not exposed to ND were used as a negative control.

2.5. Activation of NLRP3 (Inflammasome). The test was performed using HEK-Blue IL-1β cells exactly according to the manufacturer manual (InvivoGen). See Supporting Information for details.

2.6. Raman Spectroscopy. Prior to measurements a suspension containing NDs has been drop-casted on the glass slide surface and dried under room temperature to obtain a 2 mm spot of NDs. Measurements have been carried out at room temperature using a Renishaw InVia Raman microscope under the following conditions: laser excitation wavelength of 488 nm

DOI: 10.1021/acs.molpharmaceut.9b00225
Mol. Pharmaceutics 2019, 16, 3441−3451

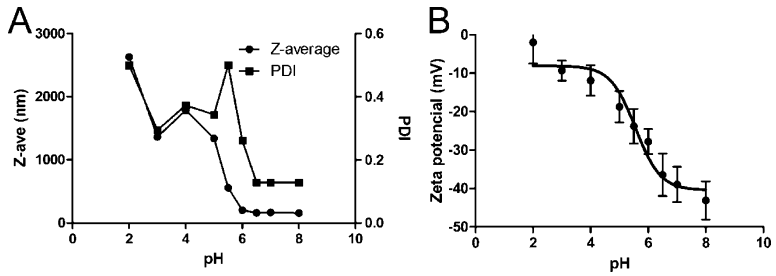

Figure 2. The effect of pH on ζ-potential of carboxylate NDs (100 nm) were dispersed in 10 mM sodium phosphate buffer with a pH ranging from 2 to 8. The size (expressed as *Z*-average) and polydispersity (PDI) (A) and ζ-potential (B) were measured at different pH values. Huckel approximation was used for calculation of the ζ-potential.

with laser power at sample of 6 mW, ×50 Olympus objective, 65 μm slits, spot focus, and grating of 2400 lines/mm.

3. RESULTS

3.1. Electron Microscopy. NDs form irregular structures with flat, cuboidal, or block 3D shapes. EM and AFM are methods for detailed characterization of the shape, structure, and surface features of NDs. Individual particles were visualized, and their detailed size distribution over a wide range, importantly also below 20 nm calculated. Heterogeneity of ND preparations with respect to the particle morphology and size distribution is clearly evident by EM, as is the tendency of NDs to form clusters consisting of ND nanoparticles of various sizes. The irregular shapes and blade-like edges of NDs are clearly visible in the TEM image (Figure 1A) as well as the SEM image (Figure 1B). These features make NDs an ideal cutter of biological membranes, as demonstrated later in this study. The flat shape of NDs must also be considered as an important parameter for their separation by flow field fractionation (manuscript in preparation) and must be taken into account when the hydrodynamic radius (R_h) and the radius of gyration (R_g) are used in the characterization of their size distribution.

3.2. Atomic Force Microscopy. A detailed analysis of the size distribution of NDs was made by AFM equipped with software for size distribution analyses. Figure 1C shows representative micrographs of the ND preparation used for size distribution analyses and visualization of the surface details of NDs (Figure 1D). AFM analysis demonstrated a bimodal distribution of the ND size; the distribution curves are presented in Figure 1E. The first and dominant peak in the distribution curve represents larger particles. This peak, which is asymmetrical, was fitted to a γ-distribution with very good approximation. The second peak is produced by very small ND particles. The small peak of the particles present in the ND sample includes 580 particles that are smaller than 30 nm (the total number of analyzed particles is 2800) and represents 0.14% of the total volume of all particles.

The total volume of the small ND particles is very small and therefore difficult to observe by other methods [e.g., DLS, NTA, tunable resistive pulse sensing, and resonant mass measurement (RMM)]. The lower detection limit for nanoparticles is approximately 20−50 nm for the NTA, TRPS, and RMM methods. NDs are unique owing to their high refractive index and relatively high mass density, but in spite of the optimization of the settings of the instruments, we were not able to detect the fraction of smaller NDs by NTA, TRPS, and RMM.

If a basic model is considered in which the volume of the particle is taken as the cube of the height of the particle, the ND particles smaller than 10 nm make up only 0.04% of the total volume of all particles. The size distribution analysis showed a mean of 93.8 nm for the ND sample. The data obtained by manual measurement and analyses of micrographs obtained by EM yielded a mean of 91−100 nm for the ND preparation (histograms not shown). These values are in perfect agreement with the parameters specified by the manufacturer, but the information provided by the manufacturer does not mention the presence of small particles. A small portion of the larger ND was demonstrated as well.

Both TEM and AFM are suitable and precise methods for the characterization of NDs in dry form, but the study of aggregation phenomena is outside their main scope, and other methods must be applied for this purpose.

3.3. Characterization of NDs by DLS, NTA, and Raman Spectroscopy. In contrast to EM and AFM, the size of NDs measured by the DLS and NTA methods is expressed as a hydrodynamic radius (nm), which means that the shape of the particles is approximated as a spherical one. Differences in the size and character of the milieu, in which the particles are measured, (dry powder vs water dispersion) lead to differences in the measured size values. In spite of that NTA gave the data which are in good accordance with AFM analyses (NTA data is presented in the Supporting Information Figure S1). DLS has the advantages of high sensitivity, a wide dynamic range of size determination (0.6−6000 nm), and low consumption of the sample (as low as 12 μL when a microcuvette is used). On the other hand, complex samples with polymodal size distributions are difficult to analyze by this method. Moreover, larger particles can mask the presence of smaller ones owing to their stronger scattering of light, which produces a signal that can obscure the weaker light-scattering signals produced by small particles.

The size distribution of the ND samples was determined using DLS (Zetasizer Ultra, Malvern Instruments, UK). The signals were difficult to obtain from very small NDs, and it was necessary to prepare and analyze serial dilutions of the material to observe the marginal signals produced by very small NDs. These data are difficult to analyze quantitatively, and underestimation of the presence of small particles is evident as demonstrated by the analyses of particle numbers (Figure 1F). The number of ND particles was analyzed by DLS, and thQ value of 2.68×10^{10} nanoparticles per 1 mg of solid ND has been calculated by software ZS explorer.

Figure S1 shows histograms of the NTA results and summarizes the size distribution data for the ND preparation. Because the limits of size detection are in the range of 20−

DOI: 10.1021/acs.molpharmaceut.9b00225
Mol. Pharmaceutics 2019, 16, 3441−3451

2000 nm, the fraction of small NDs is difficult to observe owing to the low light-scattering signal produced by small NDs. Increasing the signal intensity and hence the sensitivity of the measurement would have decreased the quality of the data obtained for larger particles without improving the detection of small ones. Individual larger particles and particle clusters in the sample, which were also observed by AFM, were efficiently detected by NTA. In comparison to the AFM data, the NTA data suggest that a small proportion of the NDs do aggregate in spite of the relatively high ζ-potential of NDs, as demonstrated in Figure 2A,B.

Raman spectra obtained from 100 nm-sized fND demonstrate the presence of the sharp line located at 1332 cm^{-1} which is attributed to the sp^3 phase of carbon. For comparison, the Raman spectra of the 15 nm sized NDs display features attributed to the presence of the disordered carbon (broadband centered at 1340 cm^{-1}) and sp^2-bonded carbon (broadband centered at ~1580 cm^{-1}) (see Supporting Information Figure S5).

3.4. Shape Analysis. The shape factor (p) was calculated using eq 1

$$p = R_g/R_h \quad (1)$$

The mean R_h (measured by DLS) and R_g (measured by MALS technique) values of the NDs were 39.8 and 48.3 nm, respectively. The shape factor (p) was calculated as 1.213; this value falls within the range 0.95−1.30, which is typical of "platy" particles. The theoretical value for a solid sphere is 0.778; a value of 0.816 is characteristic of a coil, and a value of 1.732 is characteristic of a rod.[27,28] The obtained values are in good agreement with the shapes of individual ND particles observed by TEM, SEM, and AFM.

3.5. ζ-Potential of Carboxylated NDs. The presence of a carboxyl group endows NDs with a negative surface charge; due to the presence of this group, a negative ζ-potential value is expected in water milieu at basic and neutral pH values. The high negative ζ-potential of NDs prevents their aggregation (Figure 2A,B), and the NDs exist in a slurry presumably as individual particles. Zetasizer Ultra was used to determine the ζ-potential of NDs.

As expected, high negative values of ζ-potential were found for the ND samples, predicting high colloidal stability of the ND dispersions in water. This fact is important with respect to the analysis of size distribution by methods based on light scattering. In general, these methods cannot discriminate between monocomposite particles and aggregates of similar R_h formed by smaller particles or NDs with a size of approximately 100 nm occluded by very small (5−15 nm) NDs. Acidification of the water milieu leads to a rapid decrease in the ζ-potential, and this is accompanied by extensive aggregation as reflected by an increase in the size (Z-average) and PDI of the particles (Figure 2A,B). Because this effect begins to appear at a pH near 6, the possibility that the pH within lysosomes induces colloidal instability of the ND dispersion must be considered.

3.6. Localization of NDs in THP-1 Cells. The NDs present in THP-1 cells were either localized in vesicles that were identified by immunochemical staining as lysosomes or in the form of aggregates in the cytoplasm. Individual ND particles were observed in the cytoplasm. Rarely, some NDs were observed in the nucleus (see Supporting Information Figure S4). Clusters of NDs in the cytoplasm appeared as fluorescent spots when examined by confocal microscopy (Figure 3A). The detailed structures of the ND clusters were revealed by TEM (Figure 3B). It should be noted that in the

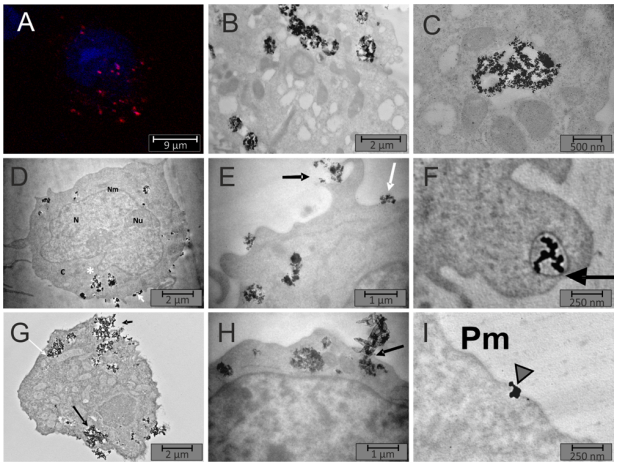

Figure 3. Penetration and intracellular localization of NDs in THP-1 cells revealed by confocal microscopy and TEM. TEM micrographs visualizing various steps of ND internalization by THP-1 cells. (A) Confocal microscopy pictures demonstrated cytoplasmic localization of fND (red spots). NDs were not localized in the nucleus (stained in blue). (B) TEM revealed localization of NDs in the cytoplasm and presumably NDs were found associated with vesicles. NDs were not localized in the nucleus. The presence of NDs in nuclei was demonstrated only sporadically in some cells (Figure S4) (C) Detailed picture of NDs associated with intracellular vesicles. (D) Overall view of the THP-1 cell showing adhesion of individual or aggregated NDs onto the cell membrane (white short arrow), aggregates of NDs in the cytoplasm (white asterisk). N—nucleus, Nu—nuclei, C—cytoplasm, and Nm—nucleic membrane. (E) Detailed picture of the internalization process of aggregated NDs via macropinocytosis (black arrows) and adhesion (white arrow). (F) Detailed picture of NDs inside of freshly formed pinocytotic vesicle (black arrow). (G) Overall view of the THP-1 cell after 24 h exposure to NDs. Formation of large aggregates of NDs in the cytoplasm (black arrow) and mechanical squeezing of mitochondrion (white arrow). Egestion of large aggregate of NDs out of cell (short black arrow). Detailed picture of mitochondrion—ND aggregate interaction in the Supporting Information (Figure S2). (H) Detailed picture of the ND cluster penetrating the cell membrane (black arrow). (I) Detailed picture of the small ND cluster and individual ND crossing cell membrane (grey arrow head) Concentration of fND was 10 μg/mL. Incubation time 2 h with exception of (G) (incubation time 24 h).

cytoplasm there are various vesicles (e.g., endosomes, lysosomes, microsomes, transport vesicles, secretion vesicles, precursors of exosomes, etc.) differing in their content. Therefore their contrast in TEM is different. Most NDs were localized in the vesicles in close contact with the vesicle membrane. Some vesicles had intact structures, whereas others appeared to possess damaged membranes (Figure 3C−G). We observed a similar pattern of ND distribution in human lung A549 carcinoma cells (results not shown). The vesicles surrounding the NDs were identified as early endosomes and lysosomes by confocal microscopy of the samples in which Rab5a-GFP protein and LysoTracker were used as specific markers of early endosomes and lysosomes, respectively. NDs were present in some but not all lysosomes. ND clusters localized in the cytoplasm outside of lysosomes were not colocalized with LysoTracker-stained organelles. Injury and destabilization of the lysosomal membrane was visualized by

DOI: 10.1021/acs.molpharmaceut.9b00225
Mol. Pharmaceutics 2019, 16, 3441−3451

TEM and confirmed by enzymatic assay of cathepsin B activity in the cytoplasm after its release from endosomes and lysosomes destabilized by NDs.

Our TEM data demonstrate various ways in which NDs enter the cell. The initial step includes interaction of individual NDs or ND aggregates with the cell membrane and their adhesion to its surface (Figure 3, Supporting Information S2). Clusters of adhered NDs induce their internalization in a process that displays the morphological features of macropinocytosis (Figure 3D,F). Because of the sharp edges of NDs and the presence of ND aggregates, NDs can also penetrate the cell membrane directly and enter the cytoplasm (Figure 3F; Supporting Information Figure S3). Inside the cells, NDs are localized within and around the vesicles identified as endosomes and lysosomes, as demonstrated by TEM and confocal microscopy (Figures 3–5). TEM pictures demonstrating various localization of NDs and their interaction with cell membrane are presented in Figure S4.

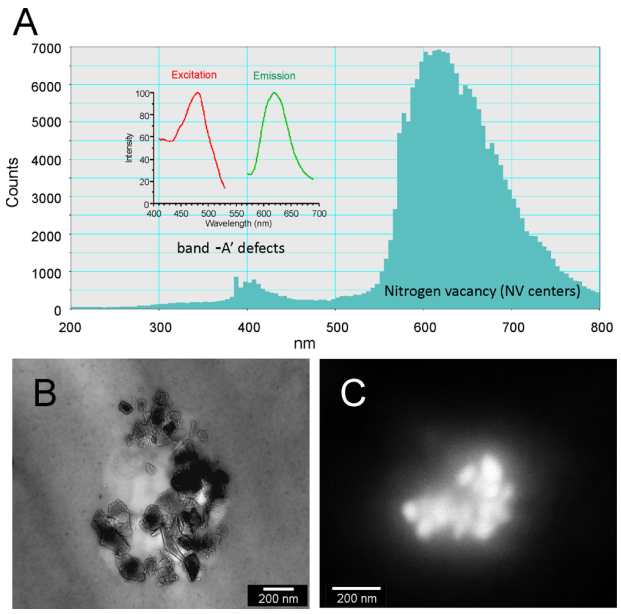

Figure 4. Visualization of fND in cell by application of EM with cathodoluminescence: (A) Cathodoluminescence spectrum of fluorescent NDs measured in an electron microscope and fluorescence spectrum (inset) of the same sample (B) detailed picture of intracellular vesicle coated by fluorescent NDs visualized by TEM. (C) Detailed picture of the cluster of fluorescent NDs associated with intracellular vesicle in THP-1 cells. NDs were visualized by SEM—cathodoluminescence. THP-1 cells were incubated with NDs (final concentration 10 μg/mL), and the specimen for TEM was prepared after 4 h incubation.

Cathodoluminescence is a unique property of fluorescent NDs and can be used to specifically visualize fND within cells by TEM. As demonstrated in Figure 4A, the fluorescence spectrum of fND is similar to the cathodoluminescence spectrum of the fND in imaged cells. Applications of confocal microscopy, monoclonal antibodies, and lysosomal fluorescent probes pointed to a fraction of lysosomes as intracellular structures containing fND. We used cathodoluminescence to confirm the localization of fND in intracellular vesicles, supposed to be lysosomes (Figure 4B,C). One must consider the fact that the number of fluorescent nitrogen-vacancy (NV) centers in fND varies and that a small portion of the fND may contain low numbers of fluorescent NV centers; therefore, both their fluorescence and their cathodoluminescence can be very weak, and these fND are difficult to detect by these methods. Nevertheless, low fluorescent or nonfluorescent NDs can be visualized by reflectance confocal microscopy owing to the high refractive index of NDs (Figure 5).

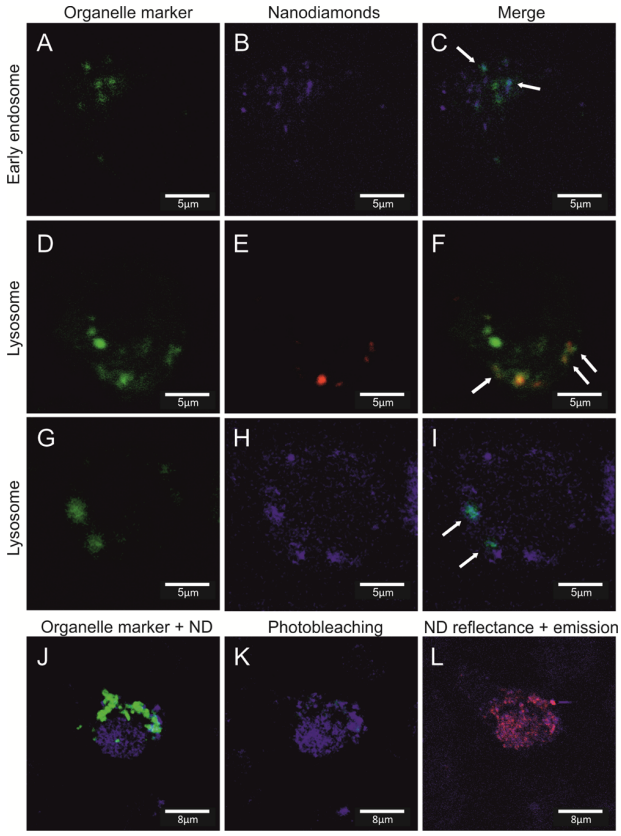

Figure 5. Colocalization of fND with early endosomes and lysosomes in THP-1 cells viewed by confocal microscopy. (A–C) colocalization of NDs with early endosomes, green (early endosome marker, cells were transfected by Rab5 protein), blue (visualization of ND using reflectance mode) (D–F) colocalization of NDs with lysosomes, green (LysoTracker was used as the lysosome marker), red (fluorescence signal of NDs). Lysosomes containing fND appeared as yellow-orange colored objects (G–I): colocalization of NDs with lysosomes, green (LysoTracker was used as lysosome marker), blue (visualization of NDs using reflectance mode) (J–K): photobleaching of a LysoTracker probe was used to clearly identify signals coming from the fluorescence probe of the lysosome and reflectance signal from NDs, whereas the fluorescence signal of LysoTracker as well as light reflected by the NDs is clearly visible before photobleaching (J), only the reflected light is observed after photobleaching (K), (L) colocalization of reflectance and fluorescence signal of internalized NDs (note that some ND are not fluorescent owing to the low content of NV centers). Concentration of fND 10 μg/mL in incubation medium, incubation time 4 h.

3.7. Release of Cathepsin B from Lysosomes Destabilized by ND. The protease cathepsin B is localized in lysosomes, and under normal conditions is not present in detectable concentrations in the cytoplasm. Destabilization of lysosomes by various lysosomal disruptors leads to the release of cathepsin B into the cytoplasm and induces several

DOI: 10.1021/acs.molpharmaceut.9b00225
Mol. Pharmaceutics 2019, 16, 3441–3451

pathways, including pathways that lead to the stimulation of inflammasomes. We used a cell-penetrating fluorogenic substrate of cathepsin B to obtain evidence for the release of cathepsin B from lysosomes injured by NDs. Cathepsin B is not the component of early endosome, and injury to the membrane of early endosome did not cause its release into the cytoplasm. Identification of lysosomes and early endosomes as the organelles in which NDs are accumulated was approved by the colocalization study using a Lyso Tracker probe and Rab5a-GFP (Figure 5).

As a positive control, we used a disruptor -LLME, which is known to be a strong and selective lysosomal disruptor. NDs were visualized by confocal microscopy in the light scattering mode at wavelengths corresponding to the excitation spectrum of the fluorescent product of CV-(RR)2 substrate cleavage by cathepsin B. After treatment with NDs at 10 μg/mL, most THP-1 cells became fluorescent (Figure 6).

The fluorescence was present in the cytoplasm but not in the nucleus. The fluorescence micrographs showed fluorescence signals both distributed throughout the cytoplasm and localized in intensely fluorescent spots. The observed fluorescence pattern suggests that several events occurred within the treated cells. First, the fluorogenic probe penetrated the slightly injured lysosomes that still contained molecules of cathepsin B. Second, cathepsin B was released into the cytoplasm from the lysosomes that were severely injured by NDs, giving rise to fluorescent staining with a disperse pattern. No substantial differences in the fluorescence patterns of THP-1 cells treated with NDs or with lysosomal disruptors that induce the release of cathepsin B were observed.

3.8. Stimulation of Inflammasomes in THP-1 Cells.

Stimulation of inflammasomes is a key event leading to the production of IL-1β, which is the key proinflammatory cytokine. THP-1 cells are a well-accepted in vitro model for testing the induction of inflammasomes. NDs were able to induce inflammasome NRLP-3 in a dose-dependent manner in the range of ND 1−100 μg/mL. Representative results are presented in Figure 7.

4. DISCUSSION

The favorable physicochemical properties of NDs for construction of drug delivery systems and diagnostic preparations for in vivo imaging must be viewed from the perspective of biocompatibility. In this work we correlated physicochemical properties of ND particles with their penetration into cells, their intracellular distribution and their ability to induce activation of inflammasomes. For this purpose various modern microscopic and physicochemical methods were used in this work to fully characterize ND.[29,30] As engineered nanoparticles, NDs are inevitably recognized by the immune system and are internalized by various mechanisms. Any persistence of NDs in tissues can lead to sustained activation of inflammasome resulting in chronic inflammation. Therefore, the ability of NDs to activate inflammasome can be assumed to be the main factor responsible for the toxicity of NDs observed in vivo.[29] Induction of inflammation is the key event that has an impact on the whole organism, and it may represent the general mechanism behind the observed adverse effects caused by NDs.

From a pharmacological point of view, aggregation of nanoparticles represents a serious problem for their possible application as drug carriers. Precise estimation of ND size distribution and their tendency to form aggregates in the biological milieu, is a requisite for all valid toxicological studies. Modification of NDs by carboxylation is one possible solution to suppress inherent tendency of NDs for aggregation owing to strong adhesive forces. Electrostatic repulsion because of negative ζ-potential of carboxylated ND diminishes their tendency for aggregation. This tendency is pH dependent (Figure 2) and can be further influenced in vivo by various components in biological fluids (e.g., proteins, peptides, and inorganic ions). It is of particular interest in the case of an organelle like lysosomes having mild acidic interior with pH around the value of 5.5−4.7. TEM and confocal microscopy visualizations of NDs accumulated in lysosomes confirmed the tendency of NDs to aggregate under mild acidic conditions inside lysosomes (Figures 3−5). Aggregation of NDs, to some extent, was also observed outside the cells in the cultivation medium. Carboxylated NDs behave like a cation exchanger binding proteins with a positive charge, it means that proteins

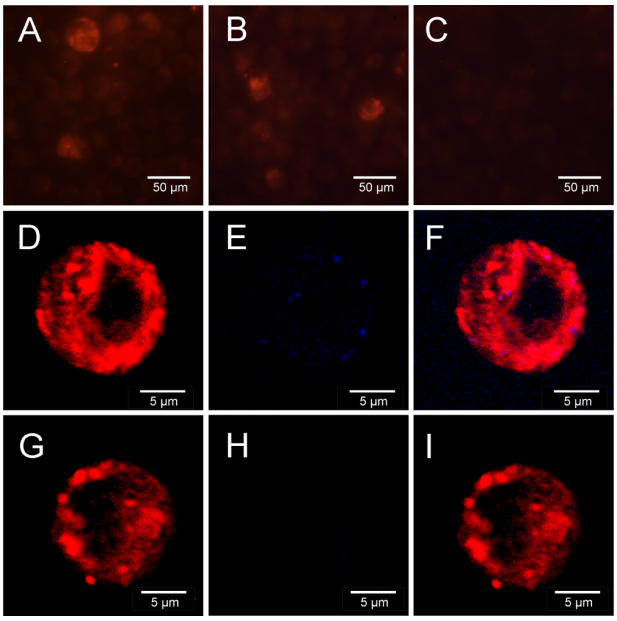

Figure 6. Release of cathepsin B into the cytoplasm in the THP-1 cell revealed by bright field and confocal fluorescence microscopy. Visualization of cathepsin B released into the cytoplasm from lysosomes injured by NDs (cathepsin B proteolytic activity was detected by fluorogenic product of CV-$(RR)_2$ substrate localized in the cytoplasm, red color). (A) release of cathepsin B after incubation of THP-1 cells with NDs visualized by bright field fluorescence microscopy. (B) release of cathepsin B after incubation of THP-1 cells with a lysosomal disruptor LLME visualized by fluorescence microscopy. (C) untreated control cells. (D−F): detailed picture of the THP-1 cell incubated with ND observed by confocal microscopy; (D) red fluorescence indicating cytosolic activity of cathepsin B, (E) blue reflectance signal of the NDs, (F) merge of (C,D). Visualization of fND in the cell by confocal reflection microscopy (scattering mode) (blue points represent ND scattered light. Wavelength of the light beam used for detection of fND was selected to be 458 nm, out of the wavelength range used for excitation of the fluorescence product generated from the substrate cleaved by cathepsin B; (G): detailed picture of THP-1 cell incubated with a LLME lysosomal disruptor observed by confocal microscopy; red fluorescence indicating cytosolic activity of cathepsin B; (H), blue—no reflectance signal observed. I—merged picture of G and H. Concentration of THP-1 cells was 10^6 cells/mL. Concentration of fND was 10 μg/mL, incubation time 2 h.

DOI: 10.1021/acs.molpharmaceut.9b00225
Mol. Pharmaceutics 2019, 16, 3441−3451

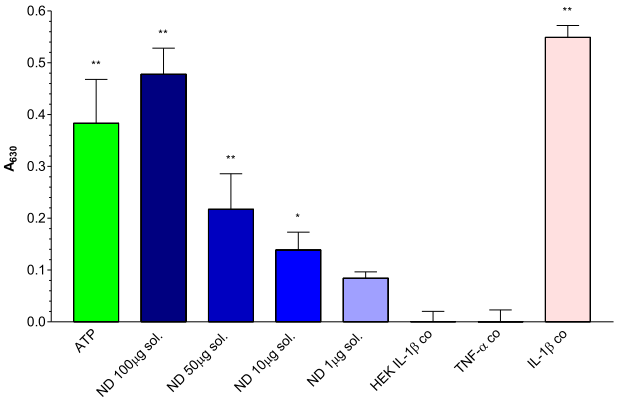

Figure 7. Stimulation of inflammasome NLRP-3 in THP-1 cells by fND. Activation of NLRP-3 was measured as conversion of proIL-1β to IL-1β. ND were tested in the concentration range 1−100 μg/mL and dose dependency of IL-1β production was demonstrated after 24 h incubation. ATP was used as a positive standard of NLRP-3 induction. IL-1β was used as the positive control in the test. Dunett's Multiple Comparison Test negative control column (HEK-Blue IL-1β cells) versus the other columns *p < 0.05; **p < 0.01; ***p < 0.001.

with low pI. Carboxylated NDs lost its negative charge, at a low pH, therefore the tendency to form protein corona via electrostatic interaction is lower. Nevertheless, the tendency to form protein corona is a general feature of nanoparticles, and NDs are no exception. Because in vitro data of ζ-potential dependence correlate well with the effect observed by TEM and confocal microscopy in cells, we can conclude that a lower pH in lysosomes contributes to ND aggregation. Of course, selective interaction of NDs (with or without biocorona) with surface proteins on intracellular vesicles cannot be excluded. But this is over the scope of this manuscript focused on activation of inflammasome.

The sharp edges of NDs produced by detonation technology make them potentially dangerous to cell membrane structures as demonstrated in Figures 3, 4, and 6. Cell membranes form compartments that separate various biochemical processes taking place inside the cell and are involved in a majority of the vital cell functions. Therefore, NDs can affect key cell structures and biochemical pathways, therefore the adverse effects can be induced, as observed in vitro and in vivo.[19,21] The THP-1 cell line in vitro model provided us with experimental evidence pointing to the mechanism of toxic effects of NDs via activation of inflammasome NLRP3 (Figure 7).

Based on pH, ionic strength, and composition of water milieu NDs can exist as individually separated nanoparticles or can form aggregates of various sizes. NDs can enter the cytoplasm by (i) mechanical penetration through the cell membrane; (ii) by pinocytosis/macropinocytosis; (iii) by endocytosis/phagocytosis). Within the cell the NDs accumulate in lysosomes or form clusters in the cytoplasm. Interaction with other organelles is not yet proved, but influence of NDs on mitochondria must be considered too with respect to possible induction of oxidative stress, apoptosis, pyroptosis, and autophagy.[29,31−33] Recently it was published that NDs at noncytotoxic concentrations were able to increase both total NO and ROS production in the A549 and BV-2 cells. The treatment negatively affected concentrations of high-energy phosphates, nicotinic coenzymes, and GSH, indicating an imbalance of energy metabolism and mitochondrial functions and sustained oxidative/nitrosative stress.[32]

On the molecular level interactions of proteins and other biomolecules with the surface of NDs can alter the conformations of proteins such as receptors, enzymes, structural proteins, hormones, and cell signaling molecules and can lead to alteration in or even a complete loss of their functionality.[34,35] NDs are chemically inert; therefore, their possible adverse effects on cells result from mechanical injury of the cell membrane structures owing to thermal motion and the sharp edges of NDs. Injury of lysosomes induced by NDs is demonstrated by the release of the lysosomally-localized protease cathepsin B (Figure 5). Other organelles like mitochondria can also be mechanically disturbed by NDs presented in the cytoplasm (Figure 3G). Oxidative stress and apoptosis can be the results of adverse effects of NDs on mitochondria.[32] A noncytotoxic dose may produce relevant biochemical alterations involving not only sustained oxidative/nitrosative stress, but also a profound imbalance in energy metabolism, mitochondrial functions, as well as triggering proinflammatory pathways.[32,33,36] Altogether, the observed effect on the subcellular level can manifest in vivo in inflammation, as will be discussed below.

The above mentioned examples provide evidence for the ability of NDs to injure the membrane structures of exposed cells in vivo as well as in vitro. Blood coagulation and inflammation are two strong defense systems that are precisely controlled to prevent the possible lethal consequences of injury. Our data on the induction of inflammasomes (Figure 7) strongly suggest that inflammation instead of thromboembolism[37] is one of the mechanisms responsible for the observed toxicity of NDs in vivo described in the literature. The inflammasome concept was first introduced approximately 15 years ago.[38−40] Priming and activation of these intracellular macromolecular complexes that sense cell stress or danger signals trigger the maturation of proinflammatory chemokines and cytokines, most notably IL-1β and IL-18, and thereby initiate innate immune defense mechanisms. The role of inflammasomes in the development of autoinflammatory diseases[41,42] must be considered in relation to NDs because of their potential to act as permanent inducers of inflammasomes, for example of NLRP3 (Figure 7). The complex role of inflammasomes in disease raises new questions about the application of NDs and in general all engineered bioresistant nanoparticles in medicine, especially with respect to their use as drug carriers that are resistant to biological degradation and rapid excretion from organisms. Accumulation of NDs in various organs such as lung, spleen, kidney, and liver can produce local concentrations of NDs that are sufficient to trigger inflammation, and consequently result in the pathological status of the affected tissues and organs.

By analogy with other engineered nanoparticles such as carbon nanotubes and endogenously produced crystalline structures such as cholesterol and urate crystals, we propose a scheme that describes, at the molecular and subcellular level, the mechanism responsible for the observed in vivo toxicity of ND (Figure 8). Our work demonstrated that the injury of the lysosomes by NDs is the central event that triggers the pathways leading to the activation of inflammasomes. Cathepsin B is released from the injured lysosomes, and its presence in the cytoplasm is a strong "signal 2" that induces the oligomerization of NLRP3. Various pathogen-associated molecular patterns (PAMPs) and damage-associated molecular

DOI: 10.1021/acs.molpharmaceut.9b00225
Mol. Pharmaceutics 2019, 16, 3441−3451

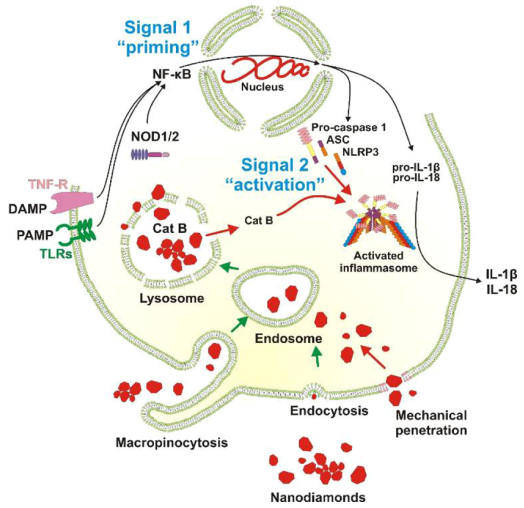

Figure 8. Schematic description of ND interaction with immune cells and mechanism of inflammasome activation. NDs enter the cytoplasm by mechanical penetration through the cell membrane, macropinocytosis, and endocytosis/phagocytosis. Sharp edges of NDs disrupt the membranes of lysosomes. Lysosomal content, including cathepsin B (CatB), is released into the cytoplasm providing the second signal triggering activation of inflammasome. The first signal is provided by various PAMP/DAMP via various cell receptors (e.g., TLRs and NOD1/2). This signal primes immune cells for activation of inflammasome. Therefore, bioresistant NDs accumulated in the tissue can induce chronic inflammation responsible for in vivo observed adverse and toxic effects.

patterns (DAMPs) provide the "signal 1", which triggers the synthesis of proIL-1β and proIL-18 together with that of inactive NLRP3 monomers. It is important to note that activation of inflammasomes by NDs is enhanced by various PAMPs, such as muramyl dipeptide, via NOD1/2 cytoplasmic receptors.[43] Because the mature cytokines IL-1β and IL-18 are potent proinflammatory cytokines, their expression at high levels in organs and tissues such as lung, brain, bone marrow, spleen, and kidney could have disastrous consequences if left uncontrolled. For example, prolonged expression of these cytokines in the brain could lead to the malignancies observed in Alzheimer's disease and other forms of dementia.[44]

The fluorescent properties of fND, together with their cathodoluminescence[45,46] make fND suitable probes for both confocal and EM. Quantum dots are of limited application because their fluorescence is quenched by osmium tetroxide fixation,[21] limiting the applicability of quantum dots for multimodal imaging. Gold nanoparticles (AuNPs) lack the biosensing capabilities of NDs and are not easily distinguished from OsO_4-stained cytosolic lipid droplets based on their appearance in electron micrographs.[47] The unique fluorescence properties of fND make them appropriate markers for correlated optical/electron bioimaging, as demonstrated recently.[48] Our results show that the use of cathodoluminescence can extend the application of fND in multimodal optical/electron bioimaging.

5. CONCLUSIONS

NDs are expected as a tool for in vitro and in vivo imaging and are currently considered as new biocompatible nanocarriers for drugs. Surprisingly, the toxicological data published in the literature show a lack of complex understanding of the mechanism(s) that govern the biodistribution of NDs in organisms, their penetration into cells and their effects on molecular structures, particularly on biological membranes. The main purpose of this study was to relate physical–chemical properties of carboxylated NDs (100 nm) to their intracellular distribution and impact on biological membranes and cell immunity—activation of inflammasome in vitro THP-1 cell line model. DLS, NTA, and microscopic methods (confocal microscopy, EM, cathodoluminescence, and AFM) were used to characterize ND particles and their intracellular distribution. According to our knowledge, this is the first in vitro study demonstrating direct activation of inflammasome by ND. It should be noted that our studies on standard carboxylated NDs do not directly imply the same effects in the case of ND particles with different chemical modifications of their surface. Specific surface modification can change ND behavior in the living cells, mainly when surface chemistry plays a key role in cell membrane interaction. Nevertheless, this surface modification can be altered in a complex environment of living cells (e.g., owing to action of enzymes and reactive oxygen species). In this case our description of ND behavior in living cells is relevant.

In this work we determined these important parameters which are crucial for interaction of ND particles with living cells:

1. The irregular shapes and blade-like edges of ND make ND an ideal cutter of biological membranes (EM).
2. In spite of relatively high ζ-potential, a small proportion of the ND exists in the aggregated state (NTA analysis).
3. Acidification of the water milieu leads to a rapid decrease in the ζ-potential of carboxylated ND which is accompanied by extensive aggregation. Because this effect begins to appear at a pH near 6, the possibility that value of pH within lysosomes and endosomes induces colloidal instability of the ND dispersion and must be considered.
4. As engineered nanoparticle NDs are inevitably recognized by the immune system, and internalization of NDs can destabilize endosomes and lysozymes in immune cells. Release of lysosomal content can induce cellular pathways leading to cytopathological processes. Cathepsin B released into the cytoplasm from injured lysozymes in combination with PAMP/DAMP molecules sensed by various membrane or cytosolic receptors (e.g., toll like receptors and NOD1/2) can trigger activation of inflammasome NLRP3 in tissue and induce chronic inflammation with pathological consequences.

There is no doubt that unique properties of fluorescent NDs make them excellent tools to study their fate and biodistribution in cells and tissues. The bioresistance of NDs and their ability to induce chronic inflammation in organisms well explains various toxic effects of NDs that have been observed and described in the literature using various in vivo animal models. Therefore, these features of NDs must be seriously considered and further studies focused on the long time effect of NDs on experimental animals are needed.

■ ASSOCIATED CONTENT

Supporting Information

The Supporting Information is available free of charge on the ACS Publications website at DOI: 10.1021/acs.molpharmaceut.9b00225.

DOI: 10.1021/acs.molpharmaceut.9b00225
Mol. Pharmaceutics 2019, 16, 3441−3451

Size distribution of NDs measured by NTA, activation of NLRP3 (inflammasome), TEM detail of interaction of NDs cluster with mitochondrion in THP-1 cell, TEM penetration of the small cluster of NDs through the cell membrane, TEM cell nucleus with localized NDs, and Raman spectra of NDs (PDF)

AUTHOR INFORMATION

Corresponding Authors

*E-mail: milan.raska@upol.cz (M.R.).
*E-mail: krat@fzu.cz (I.K.).
*E-mail: turanek@vri.cz (J.T.).

ORCID

Tereza Švadláková: 0000-0002-1581-5531
Petr Ashcheulov: 0000-0001-8085-3609
Irena Kratochvílová: 0000-0002-6633-9432
Jaroslav Turánek: 0000-0001-8001-4047

Author Contributions

Contribution of two first authors was equal. Team headed by J.T., M.M., J.K., and M.R.—in vitro effect of nanodiamond on cell culture models. Team headed by J.T. and I·K.—physical−chemical characterization of NDs. P.T.K., P.Š., and T.Š.,—in vitro tissue culture models. J.M., P·K., N·V., R.S., and V·K.—confocal microscopy, transmission, and SEM, cathodic luminiscence. E.B. and S.M.—physical-chemical characterization of nanodiamond by DLS, NTA, fluorescence spectroscopy, and field flow fractionation. L.F.—characterization of nanodiamond by AFM. P.A.—Raman spectroscopy

Notes

The authors declare no competing financial interest.

ACKNOWLEDGMENTS

This work was supported by the Ministry of Education, Youth and Sports under grants OPVVV PO1 project "FIT" (Pharmacology, Immunotherapy, nanoToxicology) CZ.02.1.01/0.0/0.0/15_003/0000495 (J.T.); Project Centre of Excellence for Nanotoxicology CENATOX GAP503/12/G147 (M.M., J.T.) and Czech Ministry of Agriculture under grant MZE0002716202 (J.T., M.M.) and RO0518 (J.T., M.M.). The laboratories of AFM were also supported by European Structural and Investment Funds and the Czech Ministry of Education, Youth and Sports (project no. SOLID21—CZ.02.1.01/0.0/0.0/16_019/0000760) (I.K.). The laboratory at ISI was supported by CSF (project 17−15451S), MEYS CR (LO1212), its infrastructure by MEYS CR and EC (CZ.1.05/2.1.00/01.0017). Supported by the Ministry of Agriculture of the Czech Republic, institutional support MZE-RO0518 (J.T., M.M.). The kind support of the company Ádamas (USA) regarding samples of nanodiamond is acknowledged. Special thanks to the project AdmireVet (CZ.1.05/2.1.00/01.0006—ED0006/01/01 from the Czech Ministry of Education, Youth and Sport) for permitting access to the scanning electron microscope. The authors acknowledged access to instruments in Education and Research Centre VRI-Malvern (join project of Veterinary Research Institute Brno and Malvern, UK) (J.T., S.M., M.K.) and in laboratory NanoPharm (join project of Veterinary Research Institute Brno, research centre ICRC and St. Anne Faculty Hospital Brno) (J.T.).

REFERENCES

(1) Schrand, A. M.; Hens, S. A. C.; Shenderova, O. A. Nanodiamond Particles: Properties and Perspectives for Bioapplications. *Crit. Rev. Solid State Mater. Sci.* **2009**, *34*, 18−74.

(2) Petráková, V.; Taylor, A.; Kratochvílová, I.; Fendrych, F.; Vacík, J.; Kučka, J.; Šturs a, J.; Cígler, P.; Ledvina, M.; Fišerová, A.; Kneppo, P.; Nesládek, M. Luminescence of Nanodiamond Driven by Atomic Functionalization: Towards Novel Detection Principles. *Adv. Funct. Mater.* **2012**, *22*, 812−819.

(3) Havlik, J.; Raabova, H.; Gulka, M.; Petrakova, V.; Krecmarova, M.; Masek, V.; Lousa, P.; Stursa, J.; Boyen, H.-G.; Nesladek, M.; Cigler, P. Benchtop Fluorination of Fluorescent Nanodiamonds on a Preparative Scale: Toward Unusually Hydrophilic Bright Particles. *Adv. Funct. Mater.* **2016**, *26*, 4134−4142.

(4) Petrakova, V.; Benson, V.; Buncek, M.; Fiserova, A.; Ledvina, M.; Stursa, J.; Cigler, P.; Nesladek, M. Imaging of transfection and intracellular release of intact, non-labeled DNA using fluorescent nanodiamonds. *Nanoscale* **2016**, *8*, 12002−12012.

(5) Kratochvílová, I.; Šebera, J.; Ashcheulov, P.; Golan, M.; Ledvina, M.; Míčová, J.; Mravec, F.; Kovalenko, A.; Zverev, D.; Yavkin, B.; Orlinskii, S.; Záliš, S.; Fišerová, A.; Richter, J.; Šefc, L.; Turánek, J. Magnetical and Optical Properties of Nanodiamonds Can Be Tuned by Particles Surface Chemistry: Theoretical and Experimental Study. *J. Phys. Chem. C* **2014**, *118*, 25245−25252.

(6) Kratochvílová, I.; Kovalenko, A.; Fendrych, F.; Petráková, V.; Záliš, S.; Nesládek, M. Tuning of nanodiamond particles' optical properties by structural defects and surface modifications: DFT modelling. *J. Mater. Chem.* **2011**, *21*, 18248−18255.

(7) Kratochvílová, I.; Kovalenko, A.; Taylor, A.; Fendrych, F.; Řezáčová, V.; Vlček, J.; Záliš, S.; Šebera, J.; Cígler, P.; Ledvina, M.; Nesládek, M. The fluorescence of variously terminated nanodiamond particles: Quantum chemical calculations. *Phys. Status Solidi A* **2010**, *207*, 2045−2048.

(8) Kovalenko, A.; Petráková, V.; Ashcheulov, P.; Záliš, S.; Nesládek, M.; Kraus, I.; Kratochvílová, I. Parameters affecting the luminescence of nanodiamond particles: Quantum chemical calculations. *Phys. Status Solidi A* **2012**, *209*, 1769−1773.

(9) Turcheniuk, K.; Mochalin, V. N. Biomedical applications of nanodiamond. *Nanotechnology* **2017**, *28*, 252001.

(10) Taylor, A. C.; Gonzalez, C. H.; Miller, B. S.; Edgington, R. J.; Ferretti, P.; Jackman, R. B. Surface functionalisation of nanodiamonds for human neural stem cell adhesion and proliferation. *Sci. Rep.* **2017**, *7307*. DOI: 10.1038/s41598-017-07361-y

(11) Mochalin, V. N.; Pentecost, A.; Li, X.-M.; Neitzel, I.; Nelson, M.; Wei, C.; He, T.; Guo, F.; Gogotsi, Y. Adsorption of Drugs on Nanodiamond: Toward Development of a Drug Delivery Platform. *Mol. Pharm.* **2013**, *10*, 3728−3735.

(12) Toh, T.-B.; Lee, D.-K.; Hou, W.; Abdullah, L. N.; Nguyen, J.; Ho, D.; Chow, E. K.-H. Nanodiamond-Mitoxantrone Complexes Enhance Drug Retention in Chemoresistant Breast Cancer Cells. *Mol. Pharm.* **2014**, *11*, 2683−2691.

(13) Adnan, A.; Lam, R.; Chen, H.; Lee, J.; Schaffer, D. J.; Barnard, A. S.; Schatz, G. C.; Ho, D.; Liu, W. K. Atomistic Simulation and Measurement of pH Dependent Cancer Therapeutic Interactions with Nanodiamond Carrier. *Mol. Pharm.* **2011**, *8*, 368−374.

(14) Bray, K.; Cheung, L.; Hossain, K. R.; Aharonovich, I.; Valenzuela, S. M.; Shimoni, O. Versatile multicolor nanodiamond probes for intracellular imaging and targeted labeling. *J. Mater. Chem. B* **2018**, *6*, 3078−3084.

(15) Mašek, J.; Bartheldyova, E.; Korvasova, Z.; Skrabalova, M.; Koudelka, S.; Kulich, P.; Kratochvilova, I.; Miller, A. D.; Ledvina, M.; Raska, M.; Turanek, J. Immobilization of histidine-tagged proteins on monodisperse metallochelation liposomes: Preparation and study of their structure. *Anal. Biochem.* **2011**, *408*, 95−104.

(16) Shenderova, O. A.; Zhirnov, V. V.; Brenner, D. W. Carbon nanostructures. *Crit. Rev. Solid State Mater. Sci.* **2002**, *27*, 227−356.

(17) Mochalin, V. N.; Shenderova, O.; Ho, D.; Gogotsi, Y. The properties and applications of nanodiamonds. *Nat. Nanotechnol.* **2012**, *7*, 11−23.

DOI: 10.1021/acs.molpharmaceut.9b00225
Mol. Pharmaceutics 2019, 16, 3441−3451

(18) Silbajoris, R.; Huang, J. M.; Cheng, W.-Y.; Dailey, L.; Tal, T. L.; Jaspers, I.; Ghio, A. J.; Bromberg, P. A.; Samet, J. M. Nanodiamond particles induce I1-8 expression through a transcript stabilization mechanism in human airway epithelial cells. *Nanotoxicology* **2009**, *3*, 152−160.
(19) Ema, M.; Hougaard, K. S.; Kishimoto, A.; Honda, K. Reproductive and developmental toxicity of carbon-based nanomaterials: A literature review. *Nanotoxicology* **2016**, *10*, 391−412.
(20) Dworak, N.; Wnuk, M.; Zebrowski, J.; Bartosz, G.; Lewinska, A. Genotoxic and mutagenic activity of diamond nanoparticles in human peripheral lymphocytes in vitro. *Carbon* **2014**, *68*, 763−776.
(21) Zhang, X.; Yin, J.; Kang, C.; Li, J.; Zhu, Y.; Li, W.; Huang, Q.; Zhu, Z. Biodistribution and toxicity of nanodiamonds in mice after intratracheal instillation. *Toxicol. Lett.* **2010**, *198*, 237−243.
(22) Schrand, A. M.; Huang, H.; Carlson, C.; Schlager, J. J.; Ōsawa, E.; Hussain, S. M.; Dai, L. Are diamond nanoparticles cytotoxic? *J. Phys. Chem. B* **2007**, *111*, 2−7.
(23) Thomas, V.; Halloran, B. A.; Ambalavanan, N.; Catledge, S. A.; Vohra, Y. K. In vitro studies on the effect of particle size on macrophage responses to nanodiamond wear debris. *Acta Biomater.* **2012**, *8*, 1939−1947.
(24) Schrand, A. M.; Huang, H.; Carlson, C.; Schlager, J. J.; Ōsawa, E.; Hussain, S. M.; Dai, L. Are diamond nanoparticles cytotoxic? *J. Phys. Chem. B* **2007**, *111*, 2−7.
(25) Suarez-Kelly, L. P.; Campbell, A. R.; Rampersaud, I. V.; Bumb, A.; Wang, M. S.; Butchar, J. P.; Tridandapani, S.; Yu, L.; Rampersaud, A. A.; Carson, W. E., III. Fluorescent nanodiamonds engage innate immune effector cells: A potential vehicle for targeted anti-tumor immunotherapy. *Nanomed. Nanotechnol. Biol. Med.* **2017**, *13*, 909−920.
(26) Ibrahim, M.; Xue, Y.; Ostermann, M.; Sauter, A.; Steinmueller-Nethl, D.; Schweeberg, S.; Krueger, A.; Cimpan, M. R.; Mustafa, K. In vitro cytotoxicity assessment of nanodiamond particles and their osteogenic potential. *J. Biomed. Mater. Res. A* **2018**, *106*, 1697−1707.
(27) Burchard, W. *Static and Dynamic Light Scattering Approaches to Structure Determination of Biopolymers*; Royal Society of Chemistry ed.: Cambridge, 1992.
(28) Baalousha, M.; Kammer, F. V. D.; Motelica-Heino, M.; Le Coustumer, P. 3D characterization of natural colloids by FIFFF-MALLS-TEM. *Anal. Bioanal. Chem.* **2005**, *383*, 549−556.
(29) Khosravi, Y.; Salimi, A.; Pourahmad, J.; Naserzadeh, P.; Seydi, E. Inhalation exposure of nano diamond induced oxidative stress in lung, heart and brain. *Xenobiotica* **2018**, *48*, 860−866.
(30) Lynch, I.; Dawson, K. A. Protein-nanoparticle interactions. *Nano Today* **2008**, *3*, 40−47.
(31) Solomatin, A. S.; Yakovlev, R. Y.; Teplova, V. V.; Fedotcheva, N. I.; Kondrachova, M. N.; Kulakova, I. I.; Leonidov, N. B. Effect of detonation nanodiamond surface composition on physiological indicators of mitochondrial functions. *J. Nanoparticle Res.* **2018**, *20*, 1−16.
(32) Fresta, C. G.; Chakraborty, A.; Wijesinghe, M. B.; Amorini, A. M.; Lazzarino, G.; Lazzarino, G.; Tavazzi, B.; Lunte, S. M.; Caraci, F.; Dhar, P.; Caruso, G. Non-toxic engineered carbon nanodiamond concentrations induce oxidative/nitrosative stress, imbalance of energy metabolism, and mitochondrial dysfunction in microglial and alveolar basal epithelial cells. *Cell Death Dis.* **2018**, *9*, 245.
(33) Mytych, J.; Lewinska, A.; Zebrowski, J.; Wnuk, M. Nanodiamond-induced increase in ROS and RNS levels activates NF-kappa B and augments thiol pools in human hepatocytes. *Diamond Relat. Mater.* **2015**, *55*, 95−101.
(34) Elsaesser, A.; Howard, C. V. Toxicology of nanoparticles. *Adv. Drug Delivery Rev.* **2012**, *64*, 129−137.
(35) Lin, Y.-C.; Wu, K.-T.; Lin, Z.-R.; Perevedentseva, E.; Karmenyan, A.; Lin, M.-D.; Cheng, C.-L. Nanodiamond for biolabelling and toxicity evaluation in the zebrafish embryo in vivo. *J. Biophot.* **2016**, *9*, 827−836.
(36) Xiang, Y.; Zhao, M.-m.; Sun, S.; Guo, X.-L.; Wang, Q.; Li, S.-A.; Lee, W.-H.; Zhang, Y. A high concentration of DMSO activates caspase-1 by increasing the cell membrane permeability of potassium. *Cytotechnology* **2018**, *70*, 313−320.
(37) Kumari, S.; Singh, M. K.; Singh, S. K.; Grácio, J. J.; Dash, D. Nanodiamonds activate blood platelets and induce thromboembolism. *Nanomedicine* **2014**, *9*, 427−440.
(38) Srinivasula, S. M.; Poyet, J.-L.; Razmara, M.; Datta, P.; Zhang, Z.; Alnemri, E. S. The PYRIN-CARD protein ASC is an activating adaptor for caspase-1. *J. Biol. Chem.* **2002**, *277*, 21119−21122.
(39) Martinon, F.; Burns, K.; Tschopp, J. The inflammasome: A molecular platform triggering activation of inflammatory caspases and processing of proIL-beta. *Mol. Cell* **2002**, *10*, 417−426.
(40) Patel, M. N.; Carroll, R. G.; Galván-Peña, S.; Mills, E. L.; Olden, R.; Triantafilou, M.; Wolf, A. I.; Bryant, C. E.; Triantafilou, K.; Masters, S. L. Inflammasome Priming in Sterile Inflammatory Disease. *Trends Mol. Med.* **2017**, *23*, 165−180.
(41) Pellegrini, C.; Antonioli, L.; Lopez-Castejon, G.; Blandizzi, C.; Fornai, M. Canonical and Non-Canonical Activation of NLRP3 inflammasome at the Crossroad between immune Tolerance and intestinal inflammation. *Front. Immunol.* **2017**, *8*, 36.
(42) Tan, M.-S.; Yu, J.-T.; Jiang, T.; Zhu, X.-C.; Tan, L. The NLRP3 Inflammasome in Alzheimer's Disease. *Mol. Neurobiol.* **2013**, *48*, 875−882.
(43) Effenberg, R.; Turánek Knötigová, P.; Zyka, D.; Čelechovská, H.; Mašek, J.; Bartheldyová, E.; Hubatka, F.; Koudelka, Š.; Lukáč, R.; Kovalová, A.; Šaman, D.; Křupka, M.; Barkocziova, L.; Kosztyu, P.; Šebela, M.; Drož, L.; Hučko, M.; Kanásová, M.; Miller, A. D.; Raška, M.; Ledvina, M.; Turánek, J. Nonpyrogenic Molecular Adjuvants Based on norAbu-Muramyldipeptide and norAbu-Glucosaminyl Muramyldipeptide: Synthesis, Molecular Mechanisms of Action, and Biological Activities in Vitro and in Vivo. *J. Med. Chem.* **2017**, *60*, 7745−7763.
(44) Fekete, L.; Kusova, K.; Petrak, V.; Kratochvilova, I. AFM topographies of densely packed nanoparticles: a quick way to determine the lateral size distribution by autocorrelation function analysis. *J. Nanopart. Res.* **2012**, *14*, 10.
(45) Hemelaar, S. R.; de Boer, P.; Chipaux, M.; Zuidema, W.; Hamoh, T.; Martinez, F. P.; Nagl, A.; Hoogenboom, J. P.; Giepmans, B. N. G.; Schirhagl, R. Nanodiamonds as multi-purpose labels for microscopy. *Sci. Rep.* **2017**, *7*, 720.
(46) Nagarajan, S.; Pioche-Durieu, C.; Tizei, L. H. G.; Fang, C.-Y.; Bertrand, J.-R.; Le Cam, E.; Chang, H.-C.; Treussart, F.; Kociak, M. Simultaneous cathodoluminescence and electron microscopy cytometry of cellular vesicles labeled with fluorescent nanodiamonds. *Nanoscale* **2016**, *8*, 11588−11594.
(47) Yuan, Y.; Chen, Y.; Liu, J.-H.; Wang, H.; Liu, Y. Biodistribution and fate of nanodiamonds in vivo. *Diamond Relat. Mater.* **2009**, *18*, 95−100.
(48) Lake, M. P.; Bouchard, L.-S. Targeted nanodiamonds for identification of subcellular protein assemblies in mammalian cells. *PLoS One* **2017**, *12*, No. e0179295.

DOI: 10.1021/acs.molpharmaceut.9b00225
Mol. Pharmaceutics 2019, 16, 3441−3451

C Indrustrial designs

C.1 Cryo-SEM holder for imaging of thin samples in the transmission mode with elemental and cathodoluminescence analysis

ÚSTAV PŘÍSTROJOVÉ TECHNIKY
AKADEMIE VĚD ČESKÉ REPUBLIKY

Technická dokumentace k funkčnímu vzorku

Kryo-držák pro SEM umožňující zobrazování tenkých vzorků v transmisním módu s možností prvkové a katodoluminiscenční analýzy

Cryo-SEM holder for imaging of thin samples in the transmission mode with elemental and cathodoluminescence analysis

Výzkumný záměr: AV0Z20650511
Grant: TG03010046, LO1212
Rok: 2017

Autoři:

Ing. Vladislav Krzyžánek, Ph.D	pracovník ÚPT
Ing. Mgr. Radim Skoupý	pracovník ÚPT
Mgr. Kamila Hrubanová	pracovník ÚPT
Mgr. Naďežda Vaškovicová, Ph.D	pracovník ÚPT

Anotace v češtině

Držák velmi tenkých vzorků pro jejich zobrazování v rastrovacím elektronovém mikroskopu (SEM) v transmisním módu pomocí STEM detektoru a zároveň umožňující jejich analýzu pomocí EDX nebo CL detektoru. Veškerá pozorování/analýzy jsou možné v teplotním rozsahu od velmi nízkých (kryogenních) teplot po pokojovou teplotu.

Účel

Kryo-držák byl navržen pro pozorování velmi tenkých vzorků umístěných na TEM síťkách a to tak, aby bylo možné pozorování v transmisním módu pomocí retraktabilního STEM detektoru, který je umístěn pod vzorkem, a zároveň umožňoval studium vzorků pomocí detektoru pro energiově-disperzní analýzu paprsků rentgenového záření (EDX), nebo katodoluminiscenčního (CL) detektoru, které jsou umístěny nad vzorkem. Tato kombinace zobrazovacích technik umožňuje stanovení rozličných vlastností studovaného vzorku bez nutnosti s ním manipulovat. Tím se snižuje šance na jeho poškození nebo kontaminaci.

Funkční princip

Kryo-držák je navržen takovým způsobem, aby jej bylo možné přenášet pomocí kryo-vakuového transferu VCT100 (Bal-Tec, Balzers, Lichtenštajnsko a Leica microsystems, Vídeň, Rakousko). Z důvodu využití pro CL, EDX a STEM analýzu jsou vzorky umístěny na rameni zprostředkovávajícím jejich chlazení a zároveň sloužícím jako stínění potlačující nežádoucí signál generovaný při dopadu primárního svazku na posuvný stolek mikroskopu. Vhodnost pro CL měření je zajištěna umístěním vzorků těsně pod povrch jejich nosiče.

Technické řešení

Kryo-držák umožňuje pevné uchycení až čtyř TEM sítěk standardních rozměrů (tj. průměr 3.05 mm), přichycených po dvou kusech. Každá pozice je, pro snadnější orientaci a práci se vzorkem, označena číslem I až IIII. Vzdálenost středu TEM sítěk od základny je 17 mm, což zaručuje použití pro většinu komerčně dostupných retraktabilních polovodičových STEM detektorů (testováno na STEM detektorech firmy FEI). TEM síťky jsou uloženy 0,2 mm pod povrchem jejich nosiče, což umožňuje nastavení vhodné pracovní vzdálenost CL zrcadla (testováno na CL detektoru MonoCL4 Plus od firmy Gatan, kde je ohnisková vzdálenost zrcadla 0,5 mm). Tyto a další význačné vlastnosti jsou vyznačeny na náčrtu v obrázku 1.

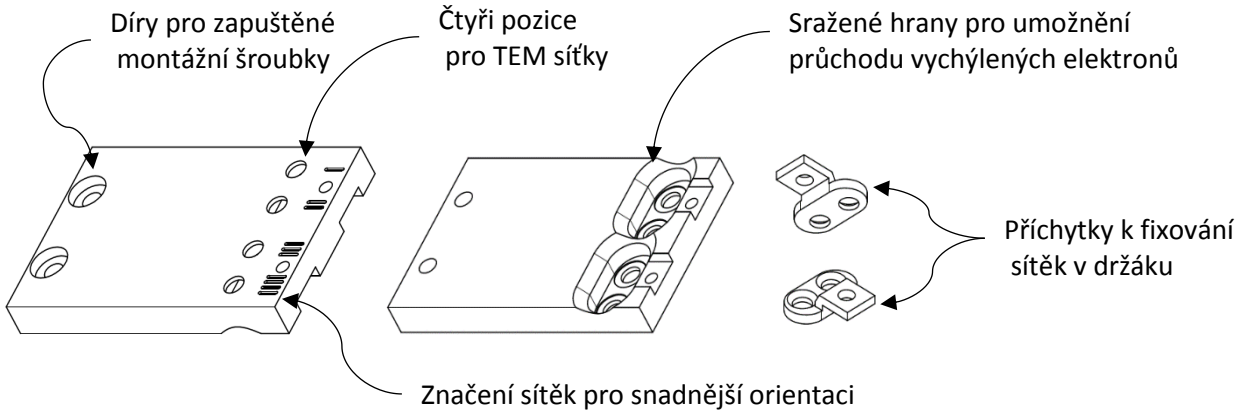

Obrázek 1: Náčrt držáku s vyznačením důležitých částí a jejich vlastností.

Realizace

Základ ramene je vyroben postupným obráběním z měděného bloku. Spojení ramene s originálním nosičem (Bal-Tec, Balzers, Lichtenštajnsko a Leica microsystems, Vídeň, Rakousko) je vyřešeno pomocí dvou nerezových nemagnetických šroubků M1,6. Systém uchycení TEM sítěk je oproti originálu zcela otočen a nově se vzorky umísťují do držáku ze spodní strany. Síťky jsou uchycovány po dvou kusech kvůli zamezení ztráty již umístěného vzorku při neopatrné manipulaci. Příchytky sítěk jsou vyrobeny z duralu a přichycené mosazným šroubkem M1,6. Sesazený komplet je vidět na obrázku 2.

Obrázek 2: Funkční vzorek připraven k použití a namontování na originální kryo zařízení.

Za autory

Ing. Vladislav Krzyžánek, Ph.D

C.2 Cryo-SEM holder and anticontaminator system for cathodoluminescence analysis in SEM at very low temperatures

ÚSTAV PŘÍSTROJOVÉ TECHNIKY
AKADEMIE VĚD ČESKÉ REPUBLIKY

Technická dokumentace k funkčnímu vzorku

Systém kryo-držáku a antikontaminačního štítu pro katodoluminiscenční analýzu v SEM při velmi nízkých teplotách

Cryo-SEM holder and anticontaminator system for cathodoluminescence analysis in SEM at very low temperatures

Výzkumný záměr: AV0Z20650511
Grant: TG03010046
Rok: 2018

Autoři:

Ing. Mgr. Radim Skoupý	pracovník ÚPT
Mgr. Kamila Hrubanová	pracovník ÚPT
Ing. Vladislav Krzyžánek, Ph.D.	pracovník ÚPT

Anotace v češtině

Předloženým návrhem funkčního vzorku je soustava držáků vzorků zamražených na terčících pro vysokotlaké mražení (HPF) a antikontaminátoru navržená pro účely zobrazování v rastrovacím elektronovém mikroskopu pomocí katodoluminiscenčního detektoru. Veškerá pozorování/analýzy jsou možné v teplotním rozsahu od velmi nízkých (kryogenních) teplot po pokojovou teplotu.

Účel

Sestava kryo-držák/antikontaminátor (AK) byla navržena pro účely pozorování vzorků v rastrovacích elektronových mikroskopech (SEM) vybavených kryo-systémem typu Bal-Tec (Balzers, Lichtenštejnsko) a Leica microsystems (Vídeň, Rakousko). Sestava je uzpůsobena pro uchycení kovových terčíků používaných v systémech pro vysokotlaké mražení High Pressure Freezing (HPF) výrobců Leica microsystems a Engineering Office M. Wohlwend GmbH, Sennwald, Švýcarsko) a to tak, aby byla možná analýza vzorků jak pomocí detektorů sekundárních a zpětně odražených elektronů, tak katodoluminiscenčního (CL) detektoru.

Funkční princip

Kryo-držák je navržen takovým způsobem, aby jej bylo možné přenášet pomocí kryo-vakuového transferu VCT100 (Bal-Tec, Balzers, Lichtenštejnsko a Leica microsystems, Vídeň, Rakousko), tzn. je zachována jeho kompatibilita s přenosnou tyčí transferu. Z důvodu využití pro CL analýzu je vzorek umístěn na rameni zprostředkovávajícím jeho chlazení a zároveň zabezpečujícím polohu 1 mm nad chlazeným AK štítem. Tato pozice umožňuje nastavit vzorek do ohniska parabolického zrcadla CL detektoru a zároveň zabraňuje jeho poškození způsobenému kolizí se štítem.

Technické řešení

Kryo-držák umožňuje pevné uchycení HPF terčíku o průměru 3 a 6 mm (v závislosti na jeho variantě) uprostřed ramene směřujícího od základny (1). Pevné uchycení HPF terčíku je vyřešeno pomocí svěráku o vhodné velikosti (2). Při zašroubování šroubku (3) sevře stolek terčík mezi svými čelistmi. Stolek je doplněn o AK (4), který je vzhledem k jeho přímému spojení s chlazeným stolkem (5) nejchladnějším místem soustavy a během zobrazování vzorku snižuje jeho kontaminaci (chladovod není zobrazen). Vzorek je ohříván na požadovanou teplotu pomocí topného elementu (6) umístěného přímo na držáku vzorku. Teplota je měřena paralelně v tělese stolku (7) a přímo na držáku v těsné blízkosti vzorku (8). Elektrické propojení topidla a sensorů teploty je provedeno pomocí konektoru (9) a kabeláže (10).

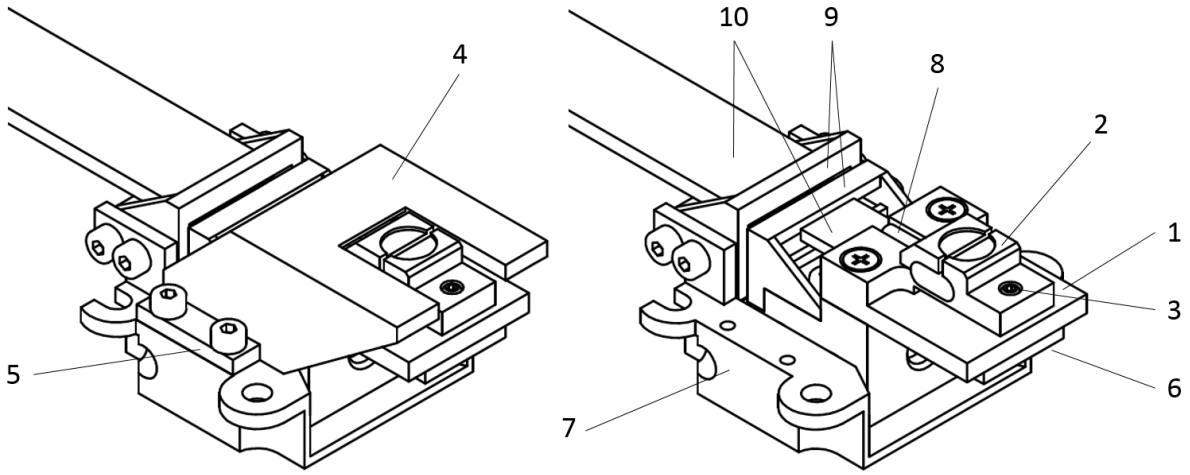

Obrázek 1: Schéma systému kryo-držák/antikontaminátor (AK) s vyznačením důležitých částí (kompletní sestava - vlevo, stav po odmontování AK – vpravo).

Realizace

Základ držáku je vyroben postupným obráběním z měděného bloku. Jeho spojení s kostkou obsahující konektor je provedeno pomocí dvou nemagnetických šroubků se zápustnou hlavou velikosti M2. Držák je konstruován pro jeden vzorek na HPF terčíku, a to z důvodu dosažení dostatečné ochrany vzorku

pomocí antikontaminačního štítu. Svírání a následné uvolnění svěráku je vyřešeno pomocí nerezového stavěcího šroubu velikosti M2. Regulace teploty je zprostředkována pomocí 2 teplotních čidel PT100 a to ve čtyřvodičovém zapojení - čidlo (8) a ve dvojvodičovém zapojení - čidlo (7). Topení je prováděno topným členem připevněným na spodní straně držáku vzorku. Regulační smyčka je poté zprostředkovávána externí jednotkou.

Význam výsledku a jeho využití v praxi

Systém kryo-držák/antikontaminátor byl během vývoje testován na mnoha experimentech, na jejichž základě byla jeho konstrukce optimalizována za účelem zvýšení reprodukovatelnosti výsledků analýz různých typů vzorků a zlepšení uživatelské přívětivosti. Výsledky získané s použitím nového systému byly publikovány v:

[1] Vaskovicova N., Skoupy R., Hrubanova K., Kulich P., Turanek J., Krzyzanek V. Localization of nanodiamonds inside THP1 cells by Cathodoluminescence. In proceeding of Mikroskopie 2017, Bratislava, Slovakia.

[2] Vaskovicova N, Skoupy R, Hrubanova K, Kulich P, Turanek J, Krzyzanek V. 13th Multinational Congress on Microscopy September 24-29, 2017 in Rovinj, BOOK OF ABSTRACTS, 2017 Zagreb, Croatia.

[3] Skoupy R, Vaskovicova N, Hrubanova K, Kulich P, Turanek J, Krzyzanek V. Cathodoluminescence imaging and mapping of biological samples in cryo-SEM. The 51st Annual Meeting of ISM Weizmann Institute of Science, BOOKS OF ABSTRACTS, 2017, Rehovot, Israel.

[4] Vaskovicova, N., Skoupy, R., Patak, A., Hrubanova, K., Krzyzanek, V. Cathodoluminescence Study of Microdiamonds and Improvements of Signal Detection by Lowering Temperature of the Sample. Microscopy and Microanalysis, 2017,23(S1), pp. 2284-2285.

[5] Turanek, J., Turanek Knotigova, P., Masek, J., Hubatka, F., Kulich, P., Kotoucek J., Simeckova, P., Celechovska, H., Koudelka, S., Procházka, L., Bartheldyova, E., Hezova, R., Vaskovicova, N., Skoupy, R., Krzyzanek, V., Macaulay, S., Fekete, L., Machala, M., Raska, M. and Kratochvilova I. Activation of inflammasomes as a mechanism of nanodiamond toxicity: Application of fluorescent nanodiamonds and advanced microscopic methods to study the intracellular distribution and activation of inflammasome NLRP3. *Particle and Fibre Toxicology* (submitted)

Za autory

Ing. Vladislav Krzyžánek, Ph.D.